Stresses and recrystallization in thin metallic films

Diplomarbeit in Physik

von

Robert J. Drese

vorgelegt der
Fakultät für Mathematik, Informatik und Naturwissenschaften
der Rheinisch-Westfälischen Technischen Hochschule Aachen

im Februar 2000

angefertigt am

I. Physikalischen Institut

Prof. Dr. M. Wuttig
Priv. Doz. Dr. T. Michely

Contents

List of Figures

Introduction to this thesis

This diploma thesis is divided into two parts. It covers two different issues and the experiments analyzed in this thesis have been performed in two different laboratories.

The first part, which is actually not the first one in chronological order, has been carried out at the RWTH-Aachen at the I. Institute of Physics A. It covers stresses in thin films.

Stresses are an area of increasing interest in thin film analysis, since virtually all thin films exhibit stresses. The order of these stresses can reach GPa, which is much higher than stresses in bulk materials. These stresses in thin films can be e.g. caused by the different linear thermal expansion coefficients of the film and the substrate.

The stresses are measured by determining the curvature of the film on a substrate using a 'wafer curvature apparatus'. Such a system to measure stresses has been installed previously [1]. Two additional parts have been added during this thesis, an annealing unit and a gas cell. The annealing unit can be utilized to determine the stress and reflectivity changes of phase change material at the phase transition temperature. The gas cell allows stress and reflectivity analysis of switchable windows, which change their properties upon exposure to hydrogen.

The second part of this thesis has been carried out at the Bell Laboratories of Lucent Technologies in Murray Hill, New Jersey. It covers the characterization of electroplated copper in damascene structures.

The characterization of the copper in these structures, resembling interconnects in computer chips, is of enormous interest, since copper interconnects are a very new technology in chip manufacturing. They allow higher performance computer chips at lower costs compared to the conventional technology of aluminum interconnects. The advantage of copper is based on its low resistance, which provides good electromigration performance and allows high clock speeds.

The electroplating process used to deposit the copper is new in this field of research. The copper electroplated into narrow trenches has unique properties analyzed in this thesis. The recrystallization at room temperature is investigated as well as the crystallographic texture of the copper.

Although these two parts can be seen separately, there are many links between them. First of all, it is essential to take care that mechanical stresses are low in computer chips consisting of several metallization levels. Stress measurements are therefore routinely performed during the development of high performance chips, especially when a new technology like the copper interconnects is implemented [7]. Another link is pre-

sented as a results of this thesis indicating that the room temperature recrystallization process might be influenced by thermal stresses prior to the recrystallization analysis.

Part I

Stress analysis using a wafer curvature apparatus

Introduction

In material science and solid state physics, stresses play a crucial role both from an experimental and theoretical point of view. Stresses are related to deformations of the crystal lattice and can cause many effects such as dislocations, which provide deep insights into the structure and the properties of a material.

Thin films on a substrate are almost always stressed. These stresses can evolve during the deposition of the material or because of thermal treatment of the samples.

Understanding and controlling the stress of a thin film compound is essential in the solid state industry, because unwanted changes in stress may lead to degradation in device performance as well as failure of interconnects and even delamination of films. On the other hand, controlling of stresses is critical for achieving the desired optical, electronic and mechanical properties of the film. Stress analysis provides important information about the material and can be used as an analytical tool as well as for quality control purposes [38].

Two thin film systems exhibiting stresses are presented in this thesis. The first material investigated is a special coating for glass that can be used to build switchable windows, which change their transparency on demand. During the change of the optical properties of these glasses, they are presumably stressed.

The second substance investigated here is a phase change material that can be used for optical data storage. During the phase transition, the volume of the film changes causing stresses in it. Before these compounds can be used in a product, the occurring stresses have to be watched closely to prevent cracking of the film.

In this thesis, stresses of thin films are measured using a 'wafer curvature' system. To measure the stress, a laser scans over the sample and determines its curvature, which yields the stress in the thin film. To allow further analysis of the stresses and stress relaxation mechanism in thin films, the system is equipped with a gas cell and an annealing unit. Samples can be exposed to pressurized gases or annealed in vacuum.

The primary goal of this work has been to characterize and to improve this system.

Chapter 1

Theoretical aspects

This chapter gives an introduction into the theoretical aspects which might be encountered when measuring stresses.

The first section gives an introduction to stress and strain using a simple one dimensional example. Then, the influence of the stress on the structure of the material is investigated from a microscopic point of view. The last part of this section generalizes stress and strain to achieve a solution for stress in three dimensions.

In the second section, the influence of stress on thin films deposited on substrates is discussed. First, the biaxial state of stress is described and Hooke's law for biaxial stress in a thin film is derived. The bending of a film–substrate combination caused by these stresses is investigated next.

The last section describes intrinsic stresses, which are occurring in thin films without external forces. Thermal stresses and stresses caused by a volume change in the thin film are discussed thoroughly, with respect to the applications of the wafer curvature apparatus described in this thesis.

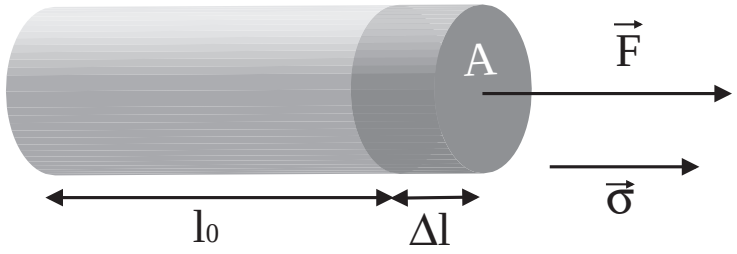

Figure 1.1: An external force F is applied to a wire causing stress and strain.

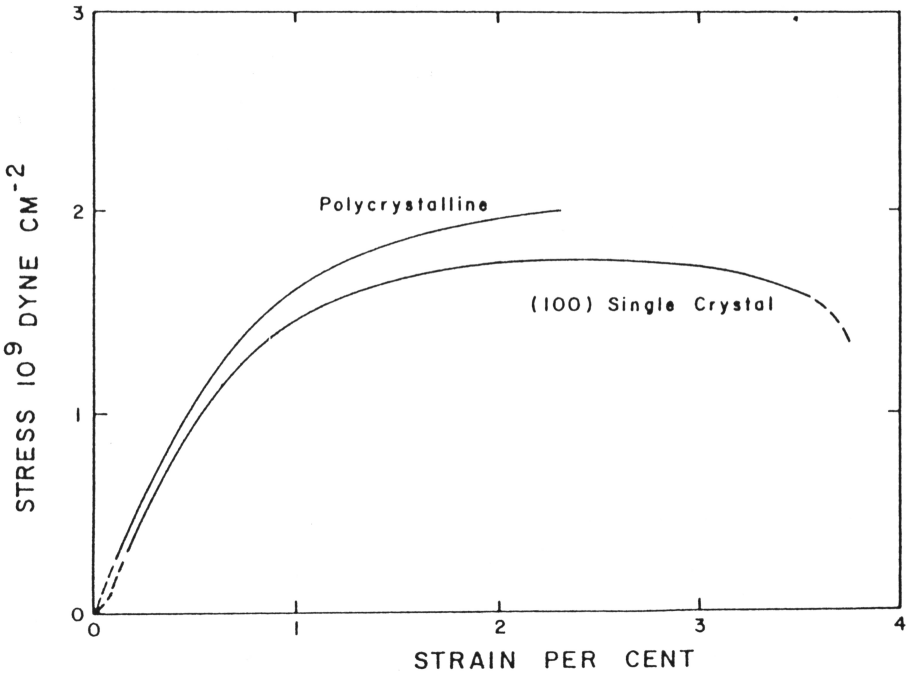

Figure 1.2: Typical stress–strain curve for polycrystalline and single-crystal gold films at constant strain rate of 0.2% per minute. (Data from [2])

1.1 Stress and strain

1.1.1 Stress and strain in one dimension

When a force F is applied to a wire of length l and cross section A, a stress is induced in the wire and it is stretched by an absolute amount of Δl (see figure 1.1).

The stress σ in the material is defined as

$$\sigma = \frac{F}{A}, \qquad \text{unit: } [\sigma] = \frac{\mathrm{N}}{\mathrm{m}^2} = \mathrm{Pa}.$$

The strain ε is given by the ratio between the elongation and the length of the wire

$$\varepsilon = \frac{\Delta l}{l}.$$

When the strain is measured for an increasing external force F, a stress-strain curve like the one shown in figure 1.2 is generated.

Because of the lateral contraction of the wire, it is important to know whether the stress plotted in such a figure corresponds to the real stress inside the material. Often, the lateral contraction of the material caused by the stress is omitted during the stress calculations, the resulting stress is called 'technical' or 'effective' stress [35].

This lateral contraction ε' is proportional to the elongation of the wire, the factor between the two values is Poisson's ratio ν.

$$\varepsilon' = \nu \cdot \varepsilon$$

material	Young's modulus E	Poisson's ratio ν	linear expansion coefficient α
Ag	$8.27 \cdot 10^{10}$ Nm^{-2}	0.367	$18.27 \cdot 10^{-6}$ K^{-1}
Al	$7.06 \cdot 10^{10}$ Nm^{-2}	0.345	$23.8 \cdot 10^{-6}$ K^{-1}
Cu	$12.98 \cdot 10^{10}$ Nm^{-2}	0.343	$16.7 \cdot 10^{-6}$ K^{-1}
Ti	$12.02 \cdot 10^{10}$ Nm^{-2}	0.361	$8.9 \cdot 10^{-6}$ K^{-1}
Si	$10.0 \cdot 10^{10}$ Nm^{-2}	0.45	$3.6 \cdot 10^{-6}$ K^{-1}

Table 1.1: Typical values for Young's modulus E, Poisson's ratio ν and the linear expansion coefficient α of some bulk materials [23], [29], [35], [40].

The value of ν varies from substance to substance. Typical values are between 0 and 0.5.

As seen in figure 1.2, there is a proportionality between the stress and the strain for low stresses. According to Hooke's law, σ calculates as

$$\sigma = E \cdot \varepsilon.$$

The constant E describing the linear relationship is Young's modulus. Values of E and ν for some materials used in this thesis are given in table 1.1.

When the external force F is removed and the strain decreases to zero, the material has been deformed elastically. Elastic deformation is possible up to approximately $\varepsilon = 10^{-3}$ (for bulk metals [35]). It is not limited to the linear region in the graph, though.

At higher stresses, the straining of the sample is no longer reversible, the deformation becomes plastic. At an even higher strain, the material breaks. The point of failure varies from material to material, it is e.g. $\varepsilon = 0.5$ for bulk gold. The strain at the point of failure is much smaller for thin films. E.g. thin, free standing gold films are destroyed at a strain of $\varepsilon = 0.01$. This value depends on various material properties like the thermal treatment of the material [8].

1.1.2 Stress from a microscopic point of view

The macroscopic stress has an influence on the microscopic properties of the stressed film. When a material is strained, this elongation has its foundation in the crystal lattice. Looking at a simple example, the influence of the macroscopic stress on the lattice is discussed.

Assuming the material is a single crystal consisting of a cubic structure, the stress is equally distributed inside the material. When there are (100) planes parallel and perpendicular to the direction of the stress, they show a different behaviour depending on their orientation (figure 1.3).

When the planes are perpendicular to the stress, the spacing between the planes increases by the macroscopic strain

$$d'_{\perp} = \varepsilon \cdot d.$$

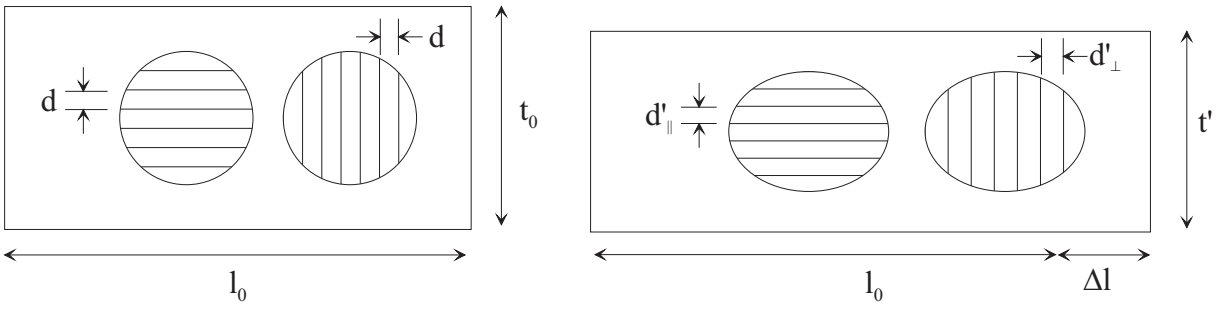

Figure 1.3: Influence of a macroscopic stress on the lattice of a thin film. The spacing between planes is strained differently for differently oriented planes.

The lateral contraction of the material is given by Poisson's ratio. Again, the spacing between planes parallel to the stress is strained by the same amount as the macroscopic material

$$d'_{\parallel} = \nu \cdot \varepsilon \cdot d.$$

Using X-ray diffraction techniques, the strain of the lattice constants can be measured directly and the corresponding stresses can be calculated [5].

1.1.3 Three dimensional state of stress

When an external force is applied to the surfaces of a material, a stress is induced inside the material. This stress can be separated into three perpendicular directions, x, y and z.

Figure 1.4 shows the stresses σ_{ij} appearing in the material. They correspond to a force in direction i, which is applied to the plane perpendicular to direction j. Normal stresses are described as σ_{ii}, the components σ_{ij} with $i \neq j$ corresponding to shear stresses.

Continuum mechanics shows that the state of stress $\bar{\sigma}$ consisting of σ_{ij} is a symmetrical tensor of second order, this gives $\sigma_{ij} = \sigma_{ji}$ and the tensor can be transformed into principle axes.

This means that each state of stress is determined completely by three components of the stress, e.g.

$$\begin{aligned} \sigma_I &= \sigma_{xx} \\ \sigma_{II} &= \sigma_{yy} \\ \sigma_{III} &= \sigma_{zz}. \end{aligned}$$

The strain ε_{ij} in the material shows the same behaviour. It is also a symmetrical tensor of second order. Stress and strain are connected by the general form of Hooke's law

$$\sigma_{ij} = \sum_{kl} C_{ijkl} \varepsilon_{kl}.$$

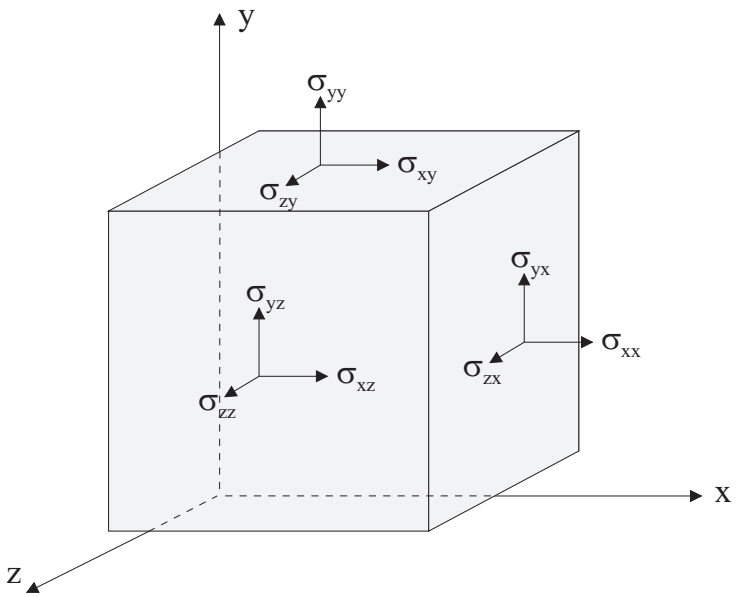

Figure 1.4: Definition of the stress components σ_{ij} contributing to a three dimensional state of stress.

C_{ijkl} is a tensor of fourth order containing $3^4 = 81$ components, of which due to the symmetrical properties of the stress and the strain, only 21 are independent.

For single crystal materials, the symmetry of the crystal structure can be used to simplify the equation even further. Depending on the crystal structure of the material, more or less components of the tensor are independent. For cubic single crystals, only three components are needed to describe the relationship between the stress and the strain.

For isotropic material (e.g. polycrystalline material) the relation can be reduced down to two independent components. Two material constants like E and ν can be used to describe the system completely. In this case, these constants are independent from the direction of the stress and their values given for a specific substance (see e.g. table 1.1) are averaged over all crystallographic orientations.

This yields the general form of Hooke's law for polycrystalline material

$$\begin{aligned}
\varepsilon_{xx} &= \frac{\sigma_{xx}}{E} - \nu\frac{\sigma_{yy}}{E} - \nu\frac{\sigma_{zz}}{E} \\
\varepsilon_{yy} &= \frac{\sigma_{yy}}{E} - \nu\frac{\sigma_{xx}}{E} - \nu\frac{\sigma_{zz}}{E} \\
\varepsilon_{zz} &= \frac{\sigma_{zz}}{E} - \nu\frac{\sigma_{xx}}{E} - \nu\frac{\sigma_{yy}}{E}
\end{aligned} \tag{1.1}$$

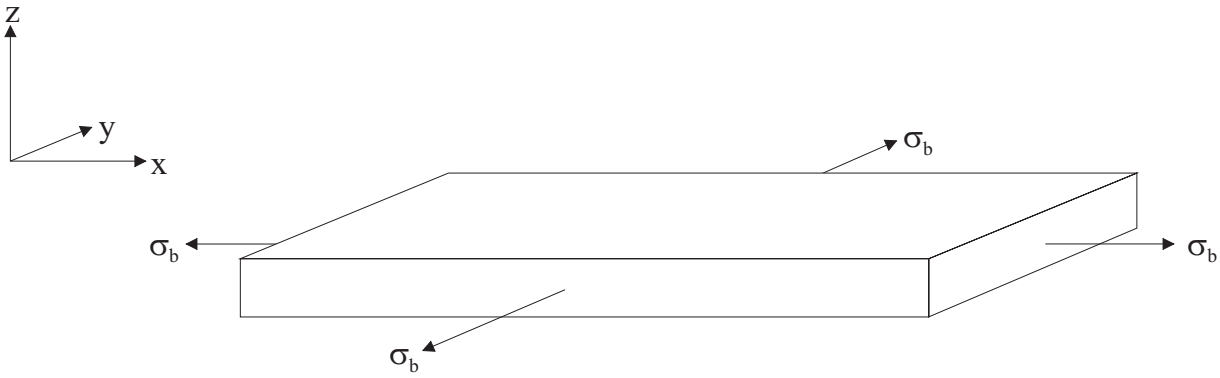

Figure 1.5: Biaxial stress in a thin film

1.2 Stresses in thin films

1.2.1 Biaxial state of stress

This section discusses a biaxial state of stress in a thin film [1].

Biaxial means in this case that all stress components are in plane with the film and there is no stress component in z-direction (figure 1.5). Equation 1.1, Hooke's law in general form for polycrystalline material, can be used here.

The stress and the strain in plane shall be homogeneous and of equal value for all directions,

$$\begin{aligned} \sigma_b &= \sigma_{xx} = \sigma_{yy} \\ \varepsilon_b &= \varepsilon_{xx} = \varepsilon_{yy}. \end{aligned}$$

The stress perpendicular to the plane is zero,

$$\sigma_{zz} = 0.$$

Calculation of the value of ε_b using the equations above gives

$$\begin{aligned} \varepsilon_b &= \varepsilon_{xx} = \frac{\sigma_{xx}}{E} - \nu\frac{\sigma_{yy}}{E} - 0 \\ &= \sigma_b \cdot \frac{1-\nu}{E} \end{aligned}$$

This yields Hooke's law for biaxial stress

$$\sigma_b = \frac{E}{1-\nu} \cdot \varepsilon_b \tag{1.2}$$

[1] According to [29], a thin film is defined as a film with a thickness d, which is much smaller than its lateral dimensions l_1 and l_2: $d \ll l_1, l_2$.

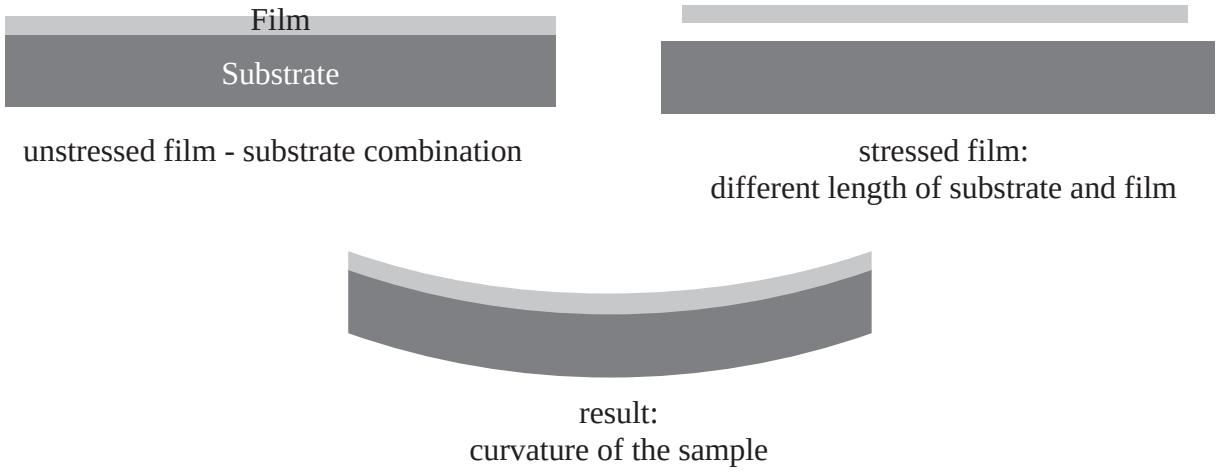

Figure 1.6: Curvature of a sample due to stress in the thin film.

1.2.2 Stresses in a film–substrate combination

Thin films are deposited onto a substrate, in this case either on silicon or on glass.

When a thin film on a substrate is stressed, it is strained by a certain amount and does not fit onto the substrate anymore. To compensate for this difference of size, the film–substrate combination will bend (figure 1.6).

1909, Stoney derived a formula that connects this bending with the stress inside the thin film [36]. Stoney's formula equals to

$$\sigma_f = \frac{1}{6R} \frac{E_s d_s^2}{(1-\nu_s) \cdot d_f} \qquad \text{with } d_f \ll d_s \tag{1.3}$$

A proof of this equation can be found e.g. in [29] or [31].

E_s is Young's modulus of the substrate, d_s is the thickness of the substrate, d_f is the thickness of the film, ν_s is Poisson's ratio of the substrate. The properties E_f and ν_f of the thin film do not contribute to this formula.

When the sample is curved towards the thin film (like illustrated in figure 1.6), the stress is tensile. This is obvious, since the film compensates for the stress by pulling at the substrate. Otherwise, the state of the stress inside the thin film is compressive.

1.3 Intrinsic stresses

When a thin film on a substrate is stressed, it is not due to an external force, but the stress occurs inside the film substrate combination. This is called an intrinsic stress. There are various origins of an intrinsic stress, according to [31], it can be, amongst other reasons, caused by

- lattice mismatch during epitaxial growth,

- incorporation of atoms,
- recrystallization processes,
- thermal effects,
- phase transformations.

The lattice mismatch occurs only during epitaxial growth, when a material with similar, but not equal lattice constant as the substrate is deposited and adopts the lattice constant of the substrate. As outlined above, this corresponds to a state of stress. For polycrystalline films like the films investigated here, this kind of stress does not appear.

When atoms are incorporated in the thin film after its deposition, the lattice is disturbed, this may also cause a stress due to the change of the lattice constants.

Recrystallization involves growth and reorganization of the grains in the thin film. It occurs mostly as a stress relaxation process at higher temperatures [12]. Investigation on recrystallization processes at room temperature are given in the second part of this thesis. Results given in that part show that stress might be a driving force of recrystallization processes.

The last two effects causing intrinsic stresses are very important for the measurements outlined in section 2.4. These effects are discussed further in the next two sections.

1.3.1 Thermal stresses

When a substance is heated, its volume changes. In general, the thermal expansion of a single crystal for small temperature changes δT is

$$\varepsilon_{ij} = \alpha_{ij} \cdot \delta T.$$

The α_{ij} describe the amount, the crystal is strained by the temperature δT. Like ε_{ij}, α_{ij} is a symmetrical tensor of second order and can be transformed into principle axes. Three linear expansion coefficients α_I, α_{II} and α_{III} completely describe the strain caused by a small temperature change. These coefficients can be different for different orientations, even the sign can vary, e.g. for zinc at 60K, $\alpha_I = \alpha_{II} = -2 \cdot 10^{-6} K^{-1}$, $\alpha_{III} = 55 \cdot 10^{-6} K^{-1}$ [35].

The relation between the strain and the temperature change is not exactly linear for large temperature changes, it can be modeled by a polynomial function for each direction

$$\varepsilon_i = \alpha_i \cdot \Delta T + \beta_i \cdot (\Delta T)^2 + \gamma_i \cdot (\Delta T)^3 + \ldots.$$

Often, only average coefficients $\alpha, \beta, \gamma \ldots$ are given as the expansion factor of a substance. In such a case, the value can be used for samples consisting of grains of random orientation. Values for α, β and γ can be found e.g. in [23].

When the temperature change is small, the relationship between the strain and the temperature can be assumed to be linear

$$\varepsilon_T = \alpha \cdot \Delta T.$$

α is called the coefficient of linear thermal expansion.

Normally, a film–substrate combination consists of two different substances with different linear expansion coefficients. When such a sample is annealed, it is stressed by the different thermal strains in the film and the substrate. The substrate and the thin film expand to different sizes. Assuming that the substrate is much thicker than the thin film and that the size of the substrate is not influenced by the thin film, the biaxial stress of the substrate can be neglected. Using equation 1.2, the biaxial stress in the thin film can be calculated as

$$\sigma_T = \frac{(\alpha_s - \alpha_f) \cdot E_f}{1 - \nu_f} \cdot \Delta T. \tag{1.4}$$

α_s is the coefficient of linear thermal expansion of the substrate, α_f of the film. The thickness of the film and the substrate does not contribute to the calculation of the stress.

The thermal expansion is very small. The increase in volume from $T = 0$K up to the melting point is for many fcc based metals 7% (Grüneisen's rule [35]). For some important materials, values for α are given in table 1.1.

Although the thermal strain of the film and the substrate is low, annealing of a film–substrate combination can cause huge stresses inside the thin film. To exemplify this, the change of stress is calculated for Al on Si using the values given in table 1.1:

$$\begin{aligned} \sigma_T &= \frac{(24 - 3.6) \cdot 10^{-6} \cdot \mathrm{K}^{-1} \cdot 7.06 \cdot 10^{10} \cdot \mathrm{N\,m}^{-2}}{1 - 0.345} \cdot \Delta T \\ &= 2.20 \cdot 10^6 \frac{\mathrm{Pa}}{\mathrm{K}} \cdot \Delta T \end{aligned} \tag{1.5}$$

This shows that a temperature difference of 1°C causes a stress of 2.2MPa in the thin film. The result of the calculation is in good agreement with experimental results [21].

For comparison, some bulk materials crack at around 70MPa (steel, [40]), thin films can reach much higher values of e.g. up to 380MPa (free standing gold film, 0.25µm thick [9]).

When annealing a sample, the thermal stress can reach the cracking limit, but the film will normally not crack. The reason for this behaviour are stress relaxation mechanisms, which take place at a high stress or at elevated temperatures, when the mobility of the atoms is increased.

Figure 1.7 shows an example of such a measurement. During the first temperature cycle, the stress increases up to about 200MPa, then, at a temperature of 150°C, the stress stops to increase and stays constant. This relaxation mechanism has been identified as a recrystallization process involving grain growth [21]. During the second and

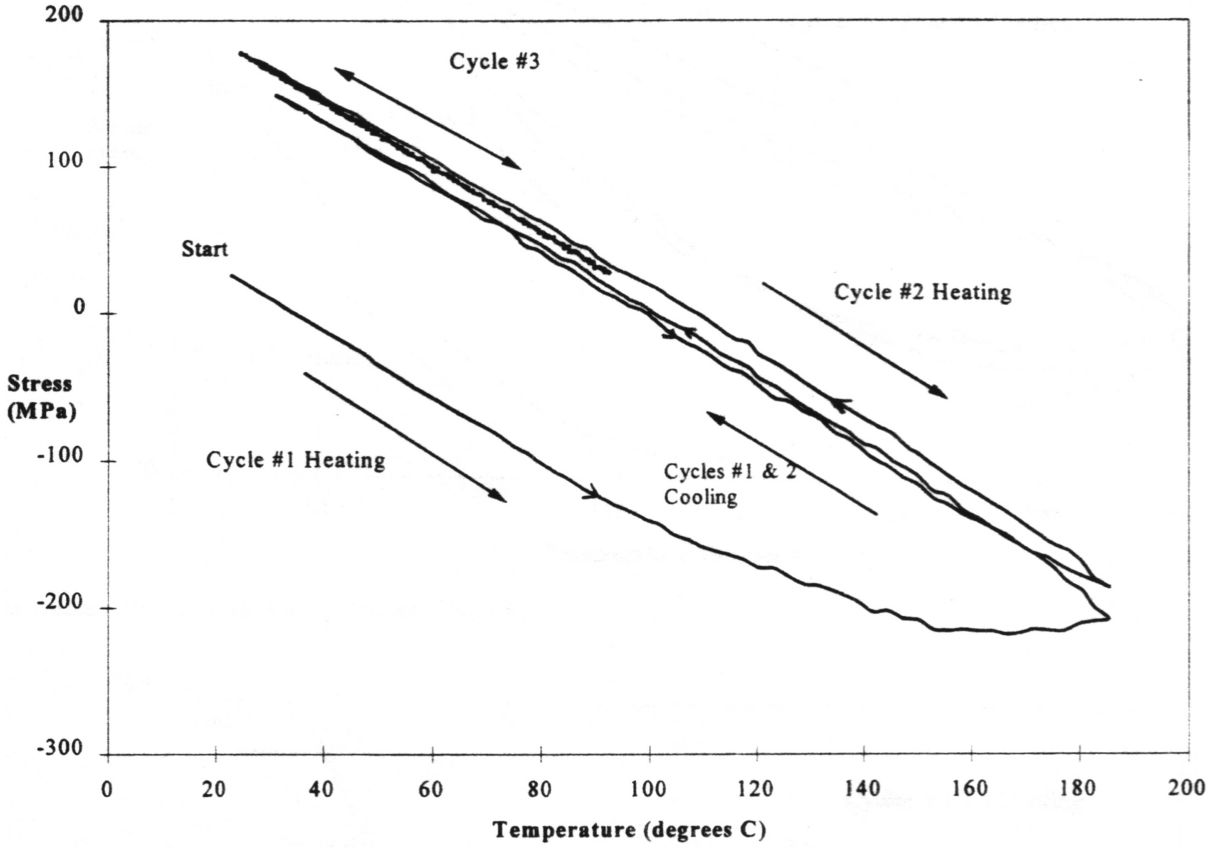

Figure 1.7: Temperature cycling of Al on Si [21]

third cycle, the large grained material does not show any stress relaxation, the stress is a linear function of the temperature.

The curvature of the sample during annealing changes correspondingly, equation 1.3 yields for a 250nm Al film on 250µm Si using the result of calculation 1.5:

$$\begin{aligned}
\frac{1}{R} &= 6(\sigma_{f_0} + \sigma_{f_T})\frac{(1-\nu_s)\cdot d_f}{E_s d_s^2} \\
\frac{1}{R} &= \frac{1}{R_0} + \frac{1}{R_T} \\
&= \frac{1}{R_0} + 13.2\cdot 10^6 \cdot \Delta T \cdot \frac{1-0.45}{10\cdot 10^{10}} \cdot \frac{250\cdot 10^{-9}}{(250\cdot 10^{-6})^2} \cdot \frac{1}{\mathrm{Km}} \\
&= \frac{1}{R_0} + \frac{1}{3443.5\,\mathrm{m}}\frac{\Delta T}{\mathrm{K}}
\end{aligned} \tag{1.6}$$

Normally, a sample has an initial curvature of radius R_0 caused by an intrinsic stress σ_0. For example, this stress can be caused by an elevated deposition temperature. When the thin film is deposited at a temperature of 50°C onto the substrate, the stress arising during subsequent cooling to room temperature would amount to

$\sigma_0 = -66$MPa. The resulting curvature (assuming that the substrate was completely flat prior to deposition) is $R_0 = -114.8$m. Since the stress in the film is negative and the sample is bent towards the film, it is tensile stress.

When the sample is annealed from room temperature, the curvature changes according to equation 1.6. At a temperature of 50°C, the sample will be flat, at higher temperatures the curvature gets positive and the stress changes from tensile to compressive. When the sample is annealed to 100°C, the overall stress will be $\sigma = 110$MPa and the corresponding curvature is $R = 68.9$m.

This calculation shows that the change of curvature caused by the temperature change is significant and can be measured.

1.3.2 Stress in the film due to volume change

This section will discuss what happens to the stress upon volume change in the film. One reason for this is e.g. a phase transformation of the material.

When the volume of the film changes, formula 1.4 can be used in a modified version. This time, the change of volume is discrete and affects only the film, while the properties of the substrate remain constant. This yields

$$\sigma = \frac{\varepsilon \cdot E_f}{1-\nu_f} = \frac{\Delta l}{l} \cdot \frac{E_f}{1-\nu_f} = \left(\sqrt[3]{\frac{V'}{V}} - 1 \right) \cdot \frac{E_f}{1-\nu_f}.$$

V is the volume prior to volume change, V' the value afterwards.

It is necessary for this equation to assume that the volume change in the film is homogeneously distributed.

This kind of volume change causes a huge amount of stress. A sudden volume change of $+5\%$ in an aluminum film on a substrate would cause a stress of 1.77GPa. This is equivalent to a thermal stress caused by annealing a thin film of Al on Si up to 803°C. These huge stresses will not be observed in the reality, since stress relaxation mechanisms will take place to compensate for this amount of stress.

Additionally, a volume change in the material often goes along with a reorganization of the material which will partly compensate for the stress.

This thesis concentrates on two types of samples showing this behaviour. On the one hand phase change media materials are analyzed. These materials change their phase from amorphous to crystalline involving a volume change upon annealing. The application of these compounds is the storage of information.

On the other hand, the stress of switchable coatings on glass is analyzed. These coatings change their colour from transparent to opaque, when they are exposed to hydrogen. This process is reversible, exposure to oxygen switches the coatings back to their transparent state. The application of these compounds are windows, which switch their transparency on demand.

Phase change media

The material used for the phase change media is $Ge_2Sb_2Te_5$. As deposited, it is in an amorphous state. After annealing up to the phase transition temperature T_p, the phase has changed to crystalline.

X-Ray reflectivity measurements show that the densities of the amorphous and the crystalline phase are different [13]. This density difference is about 6%.

Details about the structure of this material can be found e.g. in [13], [20].

Coatings for switchable windows

The coatings used for the switchable windows are based on tungsten oxide. A layer of WO_x is deposited on glass serving as the substrate. On top of the WO_x, a layer of palladium (Pd) is deposited. The palladium layer is very thin and due to the fact that the WO_x is transparent, the whole multilayer system is translucent, too. The palladium serves as a catalyzer to crack up H_2 molecules into H radicals used for switching.

When the system is exposed to hydrogen, the hydrogen ions reduce the WO_x, which changes its colour to blue. This effect can be reversed by applying oxygen to the switchable window.

This allows to create windows which can be switched from transparent to opaque on demand by changing the atmosphere applied to the coating.

Detailed information about the switching process can be found e.g. in [16], [17], [39].

Chapter 2

Experimental setup

This chapter describes the setup of the wafer curvature apparatus.

In the first section, the setup of the system is discussed and an overview of the system and the individual components including their significance to the measuring process is given.

The next section (2.2) explains how the curvature of a sample can be measured using this setup. It shows the connection between stresses in thin films (section 1.2.2) and this system.

Section 2.3 describes how changes to the setup allow a variety of samples to be analyzed. During the stress measurement, the samples can be annealed in an oven (section 2.3.3) or exposed to pressurized gas in a gas cell (section 2.3.2). Section 2.4 gives a summary of the measurements possible using these different setup.

The measurements are controlled by a computer. The program used both for calibrating and measuring has been written as a part of this thesis and is described in detail in section 2.5.

2.1 Experimental setup of the system

This section describes the system and the components used. A top view of the setup is illustrated in figure 2.1.

A standard 5mW HeNe Laser emits a monochromatic light with a wavelength of $\lambda = 633$nm, the size of the laser spot is about 1.5mm in diameter. The light is linearly polarized and the polarization axis of the light can be adjusted by a $^{\lambda}/_{2}$–waveplate, which is positioned in front of the laser.

A mirror reflects the light onto one of the main parts of the setup, the scanning mirror. This scanning mirror is a small mirror fixed on an axis which can be rotated by several degrees. The tilting angle of the mirror is controlled by the current applied to the scanning mirror. When the mirror is tilted, the laser beam is directed up or down (out of the paper plane in figure 2.1).

The next component in the beam path is the polarizing beam splitter, the light is

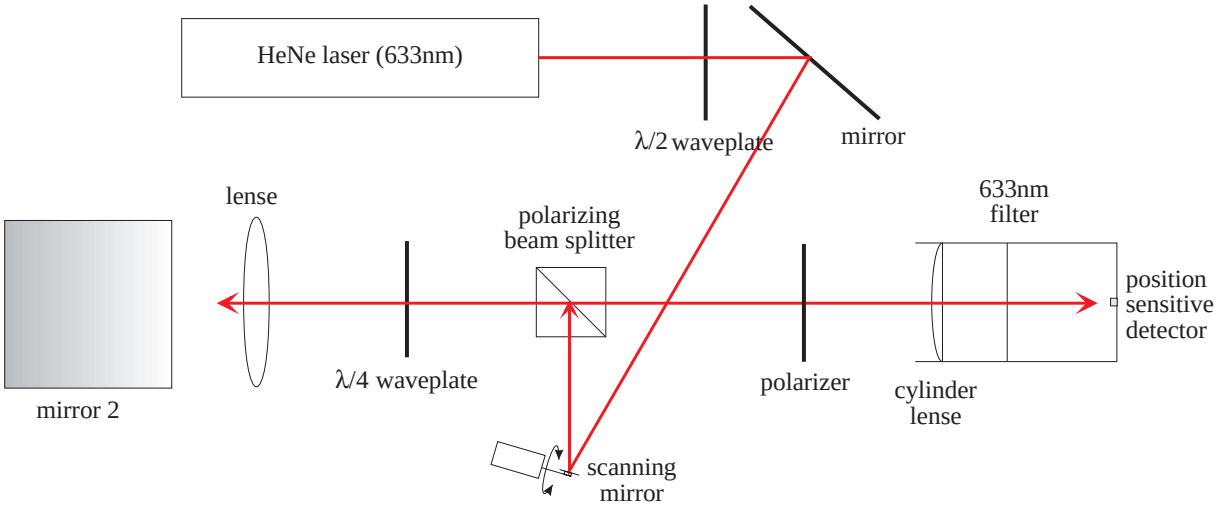

Figure 2.1: Top view of the setup.

either reflected by 90° to the left side or it passes the beam splitter straight depending on the polarization of the light. This effect is used to control the intensity of the light on the sample.

The light heading towards the sample passes a $\lambda/4$–waveplate and is refracted by a lens. The scanning mirror is positioned in the focal point of the lens. This provides a beam parallel to the optical table behind this lens, no matter how the scanning mirror is tilted.

Next, the beam is directed by a second mirror towards the sample, where it is reflected. The tilt of the scanning mirror determines the position of the laser beam on the sample. This part of the setup is called the sample holder and can be varied depending on the samples, which shall be measured. The different setup possibilities of this part are described in detail in section 2.3.

The reflected light crosses the lens and the $\lambda/4$–waveplate again. Due to the fact that the light has passed this waveplate two times, its polarization axis is changed by 90° and it passes the beam splitter without change of direction.

The light crosses a polarizer, which is used to control the intensity of the laser spot on the detector, enters the box containing the detector and passes a cylinder lens. This cylinder lens is used to focus any beam parallel to the beam path onto the detector. This lens is necessary since the width of the detector is small. Behind the lens, a band pass filter filtering out any wavelength but 633nm is installed.

Finally, the light passes on to the position sensitive detector. This detector supplies a voltage depending on the vertical position of the laser spot on the sensitive area of 0.7mm×12mm. It is therefore possible to measure the vertical position of the reflected laser beam.

2.2 The measurement method

To demonstrate how the system measures the curvature of a sample, the beam path is shown for three different sample conditions in figure 2.2. Since the detector and the beam splitter are both positioned in the focal point of the lens, they are drawn at the same place in the figure. The laser beam is shown for two different scanner positions. It is important to notice that each one of the two beams drawn in the figures represents the laser beam at a different moment in time, in reality they are never both present at once.

Figure 2.2 a) shows what happens, when the sample has a planar surface and is mounted horizontally. The incoming and the reflected beam are identical. There is no movement of the laser spot on the detector during scanning.

In figure 2.2 b) the beam path for a flat and tilted sample is illustrated. The parallel beams reaching the sample are reflected at an angle and are still parallel. Since parallel beams are always focused in the focal plane of the lens, the laser spot on the detector does not move during scanning, either. The position of the spot on the detector differs from example a).

Figure 2.2 c) shows the situation for a curved sample. When the sample is not flat but curved, it depends on the position of the scanning beam on the sample in which direction the beam is reflected. The reflected beams are therefore no longer parallel and not focused in the focal point of the lens, but to a different point in front or behind the detector. Because of this, the reflection will move on the detector by a length of x during the scan.

The movement of the reflected beam is used to calculate the curvature of the sample. The ratio between the scanned length on the detector and the scanned length on the sample is reciprocal to the radius of the curvature. The radius of the curvature can be calculated by this equation:

$$\frac{x}{s} = \frac{2f}{R}. \tag{2.1}$$

In appendix A, the exact derivation of this formula is shown. This equation forms the basis of the measurement method. When the curvature of the sample is known, it is easy to calculate stresses via Stoney's formula 1.3.

Since the beam splitter has a different refractive index than air, f will differ from the actual distance between the lens and the detector. This affects equation 2.1, because it is derived from the geometrical properties of the system. The value used for the actual calculation is therefore lower than $2f$ and can be determined by the computer program controlling the setup as described in section 2.5.

It is also important to keep in mind, whether the laser scans over the film or over the substrate. The sign of the calculated stress depends on the correct sign of the curvature.

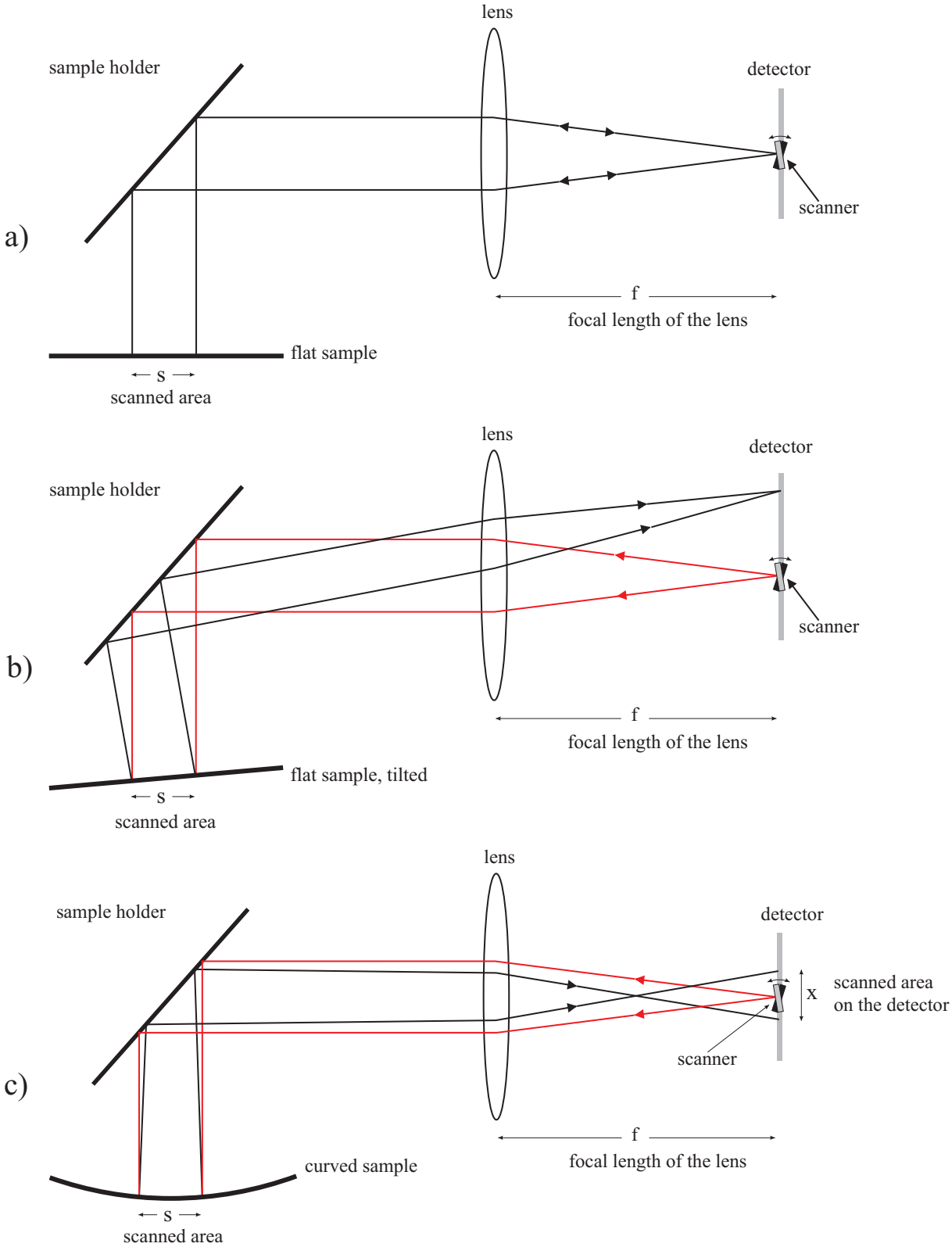

Figure 2.2: The reflection of the laser beam is shown for three different samples. In the first two figures, the sample has a planar surface and the reflection does not move on the detector during scanning. The third figure shows a curved sample, the reflected beams are no longer focused on the detector and move vertically on the detector during scanning.

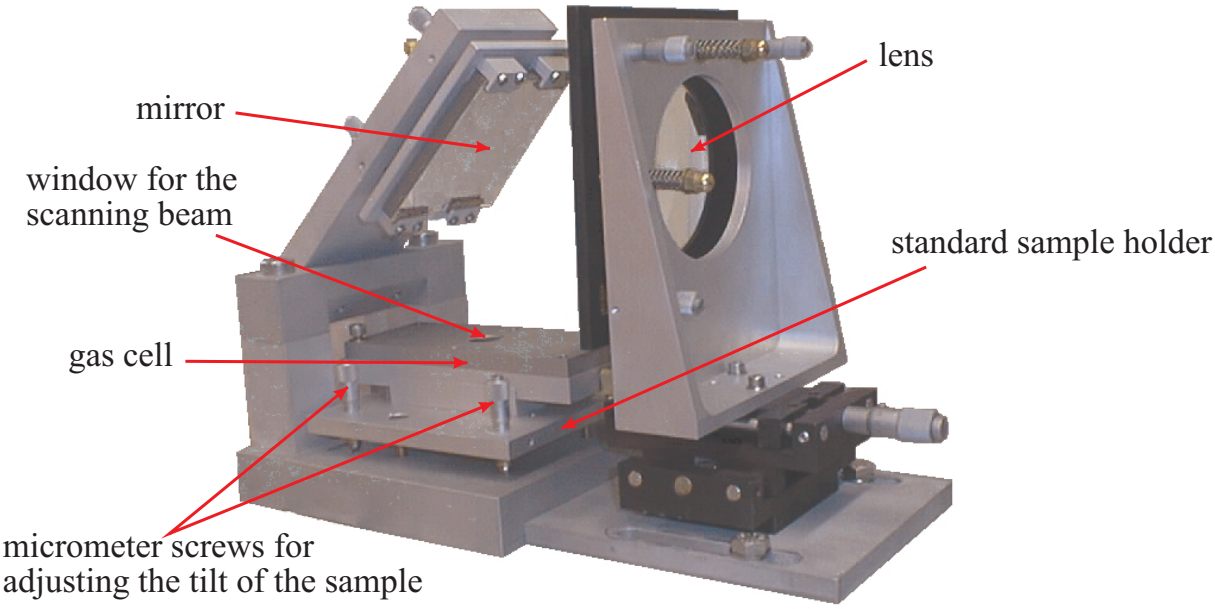

Figure 2.3: Lens and standard sample holder in which, instead of a sample, the gas cell is mounted.

2.3 Sample holders

The standard sample holder unit used in the setup consists of a mirror at an angle of 45° directing the light onto the sample. Instead of the sample, a gas cell can be mounted here. Behind this sample holder there is a combination of two mirrors fixed on the optical table, which direct the beam towards an annealing unit, when the first sample holder is removed. The different units and their applications are described in the next sections.

2.3.1 Standard sample holder

The standard sample holder (see figure 2.3) consists of a mirror at an angle of 45° which directs the laser beam onto the sample. The samples are put onto three metallic balls in the sample holder and held by gravity only. It is important that the sample is not fixed, since the curvature of the sample could be changed by this.

Using this sample holder, it is possible to measure the curvature of a sample. When the curvature of the substrate before deposition is known, it is possible to calculate the amount of stress in the thin film by the use of Stoney's formula (formula 1.3).

2.3.2 Gas cell

The gas cell can be mounted in the standard sample holder instead of a sample (figure 2.3). It is a is specially designed box made of aluminum. A small window allows the

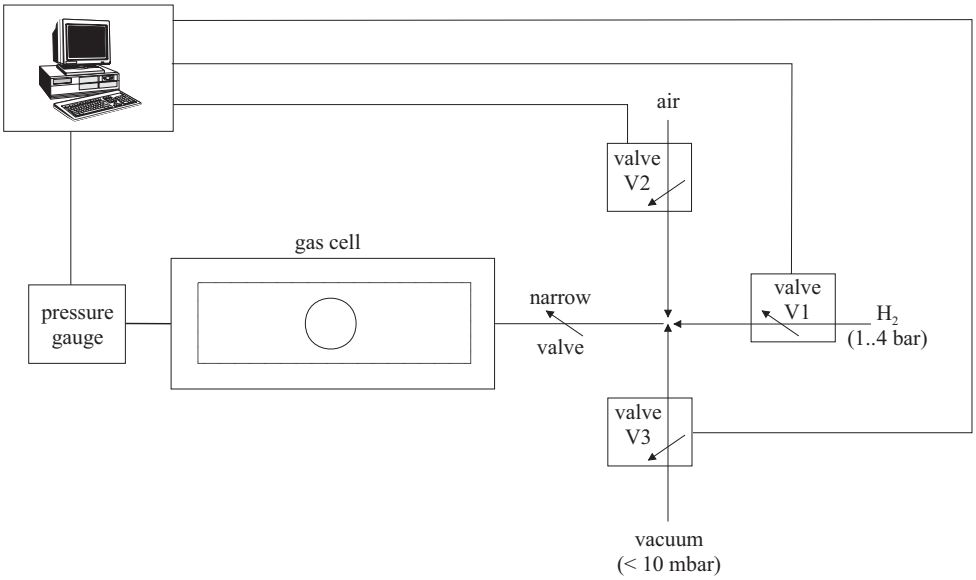

Figure 2.4: Valves and connections of the gas cell

scanning of the sample.

It is possible to change the pressure and the atmosphere inside the gas cell. It can be evacuated ($<$ 10mbar), filled with a gas (98% argon plus 2% hydrogen, up to 4bar) and it can be opened to let in air. The three valves (see figure 2.4) can be switched individually by the computer. A fourth, very narrow valve connects the other valves with the gas cell to smooth out the pressure changes inside the cell. The pressure inside the cell is monitored by the computer.

The purpose of the gas cell is to analyze the stress and reflectivity changes of a switchable coating on glass during switching.

2.3.3 Annealing unit

When the standard sample holder is removed, two mirrors guide the light towards the annealing unit (see photo 2.5). The annealing unit is a vacuum chamber with a heatable sample holder inside.

The sample holder is a block made of copper with a hole in center where the sample is positioned during the measurement (see photo 2.6). The sample is supported by a ball and a cylinder. The cylinder has a small slit containing one of the two thermocouples to measure the temperature of the sample. The other thermocouple is positioned slightly over the sample. Above the sample, a slit across the copper block allows the laser beam to scan over the sample. The sample is heated by two infrared radiators positioned inside the block.

Around the copper block, a hollow cylinder flooded with streaming water prevents heat transfer by radiation to the whole unit. Additionally, the inside of the cylinder is covered with several spacer layers of steel foil. At the two open ends of the cylinder,

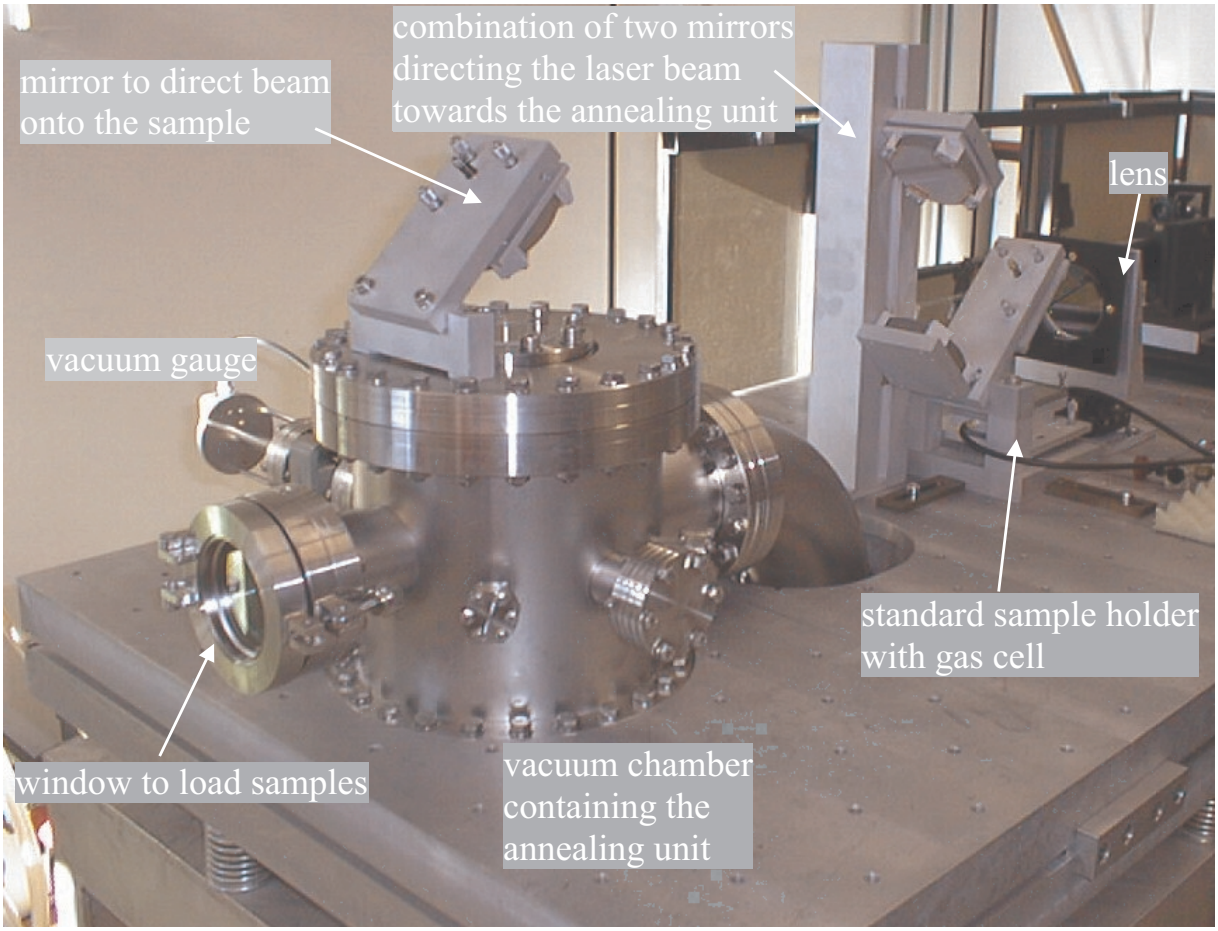

Figure 2.5: A photo of the setup. The vacuum chamber in in front contains the annealing unit. Next to it are two mirrors used to direct the laser beam towards the vacuum chamber, when the standard sample holder is removed.

two additional heat shields made of copper are attached. They are also covered with several layers of foil.

The copper block contains also a cooling system. Air or water can flow through pipes in the copper block. Water as cooling fluid has the advantage of a fast cooling rate, but it prohibits high temperatures and prevents fast annealing rates. When the sample has to be annealed quickly or the temperature has to be very high, air is used for cooling.

To adjust the sample, the whole copper block is mounted on two micrometer screws and a fixed leg. The micrometer screws are accessible from the outside to enable adjustment of the sample tilt in the evacuated chamber.

The vacuum chamber is evacuated by two pumps, a turbomolecular pump and a mechanical pump. A pressure of less than 10^{-6}mbar can be achieved. The temperature can reach up to 500°C with air cooling, the maximum annealing rate is about 3°C per minute. When cooling with water, it takes longer time to reach a given temperature,

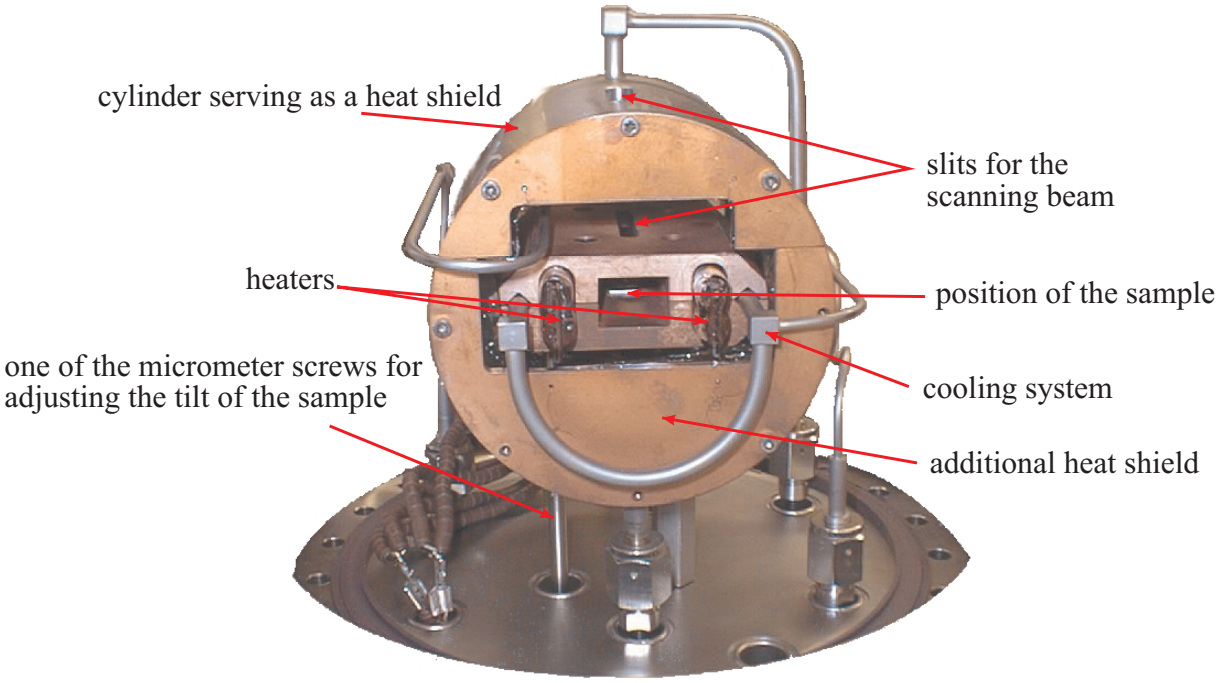

Figure 2.6: The annealing unit

especially at higher temperatures the rate is very low, only 1°C per minute can be achieved. The advantage of water cooling is the faster cooling rate, with cooling by air the decrease of the temperature can be as low as 1°C/min.

The temperature inside the oven is regulated by an Eurotherm 818P temperature controller, which is monitored by the computer.

The purpose of the annealing unit is to analyze the stress and reflectivity changes of samples during annealing in vacuum.

2.4 Summary – possible measurements

The different sample holders allow a variety of measurements on miscellaneous samples.

standard sample holder

- the curvature of samples can be easily determined
- curvature measurements before and after deposition yield the intrinsic stress of the deposited film

gas cell

- samples can be exposed to pressurized H_2, air and vacuum

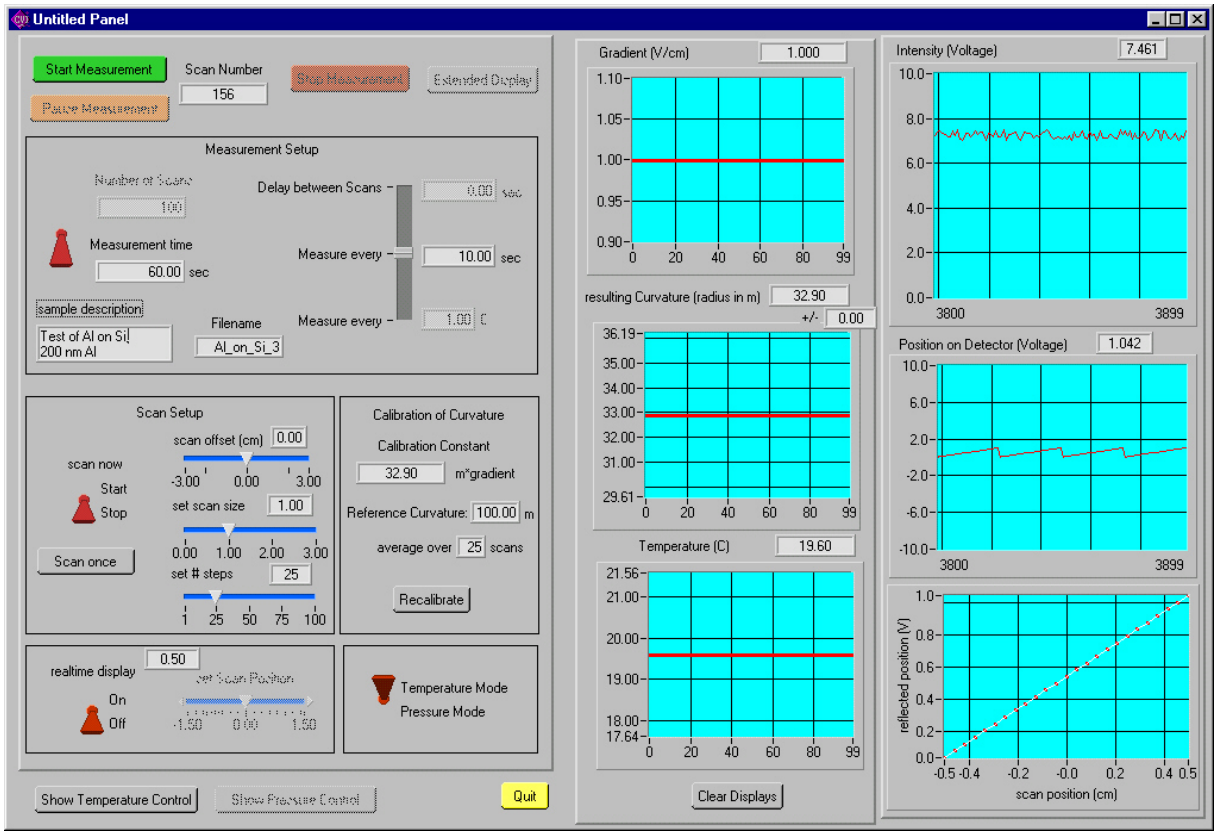

Figure 2.7: The main part of the computer program

- in situ analysis of stress and reflectivity during the switching of switchable windows

annealing unit

- samples can be annealed up to 500°C in a vacuum of less than 10^{-6}mbar.
- in situ analysis of stress and reflectivity during annealing of thin metal films and phase change media.

2.5 Controlling the measurement by computer

To enable all the different types of measurements mentioned above, the system is controlled by the computer. A computer program to serve this purpose has been written in 'C' using 'Lab–Windows'. It can be used both for measuring and adjusting the machine, a screen shot is shown in figure 2.7.

The scanning of the sample is done in small, discrete steps. The length of a scan can be set to a value between 0cm and 3cm, the number of steps is between 0...100. The position and intensity of the reflection on the detector is recorded for each of these

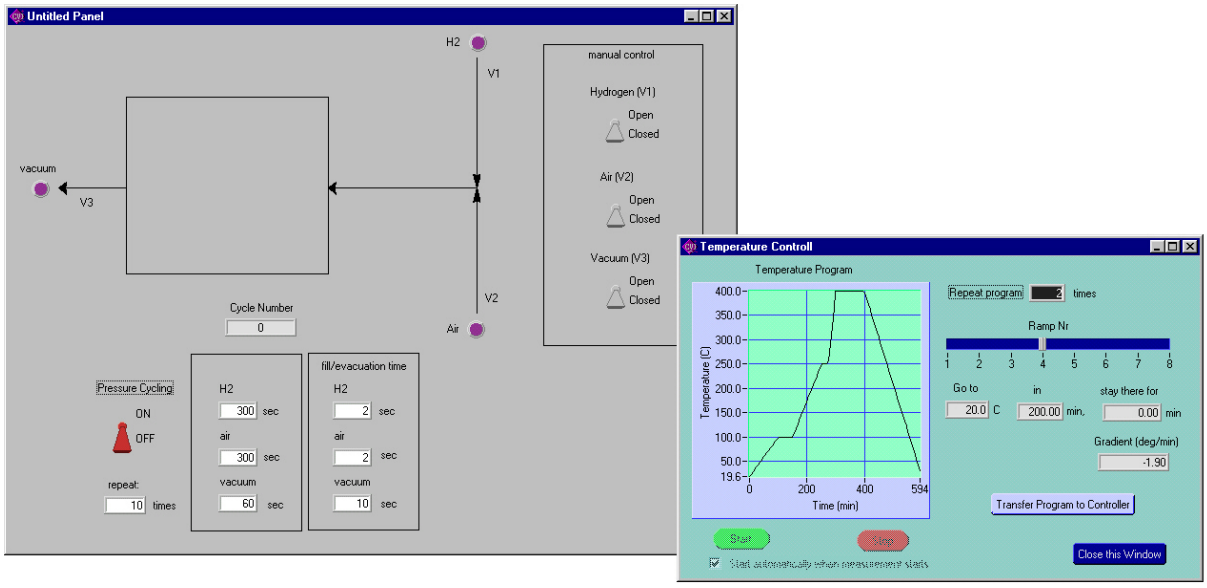

Figure 2.8: The temperature controller can be easily programmed and the pressure can be controlled manually or automatically by the computer program.

steps. Actually, each step is measured a hundred times to reduce noise (see section 3). Using the recorded values, the ratio between the movement of the reflection on the detector and the scanned length $\frac{\Delta x}{\Delta s}$ is determined by a linear regression as well as the statistical error of this regression.

To adjust the mirrors or the sample, it is possible to look at the state of the detector at the moment without scanning by using the 'real time display' function, which provides the position and intensity of the reflected beam every 0.5 seconds.

For adjusting the curvature calculation, a calibration function is implemented. During this calibration, one of the standard mirrors is scanned for a given number of scans, the measured gradients are averaged and the correct value of the constant $c = 2f$ used in formula 2.1 is generated accordingly. Since the gradient is measured by the computer as the voltage difference ΔU on the detector over the scanned length Δs on the sample, the generated constant is shown in this units: $[c] = \mathrm{m} \cdot \mathrm{V} \cdot \mathrm{cm}^{-1}$. To calculate the value in meters, c has to be multiplied with a factor of $0.06\mathrm{cmV}^{-1}$. This takes in account that the size of the detector is 1.2cm and the voltage difference across it equals to 20V.

An actual measurement consists of many scans. The time between two of these scans can be adjusted in three different ways. It is possible to set up a delay between two scans, this is especially useful, when the time between two scans should be low (a delay of 0s lets the computer scan as fast as possible). A second possibility is to set a timer, which collects data every n seconds. This is a very good solution for long term measurements. Especially for measurements, involving temperature changes, it is possible to set a temperature difference ΔT, after which a new scan should be

performed. In this case, the computer checks permanently, whether the temperature changed more than ΔT compared to the last scan. If it has changed that much, new data are collected.

To set the ending condition of a measurement, a number of scans or a certain time can be specified, after which the measurement stops.

The program allows also a manual stop of the running measurement. Useful, when something has to be readjusted, are the functions to pause and later resume the measurement.

Depending on the sample holder used, the program can be run in a 'temperature mode' or a 'pressure mode'. The difference between the two modes is not big, in the first case, the temperature and pressure of the annealing unit are recorded and the temperature controller can be programmed. In the latter case, the pressure inside the gas cell is monitored and the switching of the valves can be controlled.

To visualize the running measurement (see figure 2.7), there are two columns of graphs. The right column shows values for every recorded step. There are plots of the intensity and the position of the reflection for each step. The position of the reflection x is also shown as a function of the scan position s in a separate graph. Additionally, the fitted line is plotted there as well as the statistical error.

In a second column, values are shown for each scan. The gradient and the curvature are calculated and shown in separate graphs. The temperature or the pressure (depending on the type of measurement) is measured at the end of each scan and is shown in a graph.

An extended display allows an even better overview over the parameters recorded. Both the x and the y-axis can be chosen individually, which enables plots like curvature over temperature or intensity over pressure. It is possible to change how much data is displayed in this window during the measurement.

When a measurement is running, the computer saves all relevant data collected in two files on the hard disk. The first file contains the starting and ending time and date of the measurement, a sample description, the scanning parameters and for each scan

- number and time of the scan,
- temperature and vacuum pressure or just the gas pressure, depending on the type of measurement,
- calculated gradient and curvature and their statistical errors,
- intensity, averaged over the complete scan.

In a second file, each scan is saved completely. For each step, both the intensity and the position of the reflected beam on the detector are saved. This information can be especially useful for fixing problems and for finding systematic correlations. It is for example possible to see how much the reflected beam moved up or down or how the profile of the intensity changed during the measurement.

Every 100 scans, the files are closed and reopened to prevent loss of data in case of a power failure or a different problem causing the computer to stop working. During a measurement, a lot of data is recorded, especially the second file gets very big, a typical long term measurement easily fills several Megabytes.

In addition to the functions concerning the direct measurement, some supplementary features are implemented in the program. The temperature controller of the annealing unit can be easily and comfortably programmed in a graphical mode (see figure 2.8). Up to eight different ramps can be programmed, each ramp consists of a temperature to achieve, the time it takes to reach it and the time the temperature is then kept on a constant level.

The pressure during measurements using the gas cell is also controlled by the program (see figure 2.8), the valves can be switched manually or automatically.

Both the temperature and the pressure programs can be repeated a given time to perform several cycles. This makes long term measurements overnight or over the weekend possible.

Chapter 3

Characterization of the wafer curvature apparatus

The wafer curvature apparatus is characterized in this chapter.

The first part discusses the noise of the system. The noise level is analyzed for a stable, not moving, laser spot on the detector (section 3.1). The noise of the measured position and intensity are studied thoroughly. Next, the noise during a long term measurement is discussed (section 3.2).

The influence, which reflections caused by optical components can have on a measurement, is investigated in section 3.3. A scanning reflection of low intensity and a stable laser spot of varying intensity are monitored on the detector to learn how the resulting signal is composed of the two laser spots.

The results of the previous sections are discussed in section 3.4 and improvements of the setup are suggested.

The quality of the samples and its influence on the measured curvature is discussed in section 3.5. The relationship between the noise of the system and the error of the linear regression is also discussed in this section.

The last two sections (3.6 and 3.7) are dedicated to the characterization of the gas cell and the annealing unit. Problems prohibiting measurements are revealed and clarified. Possible solutions are shown, too.

3.1 Characterization of the detector noise

In this section, the noise of the detector and the rest of the system is investigated. To determine which components of the system are contributing to the noise, the experiment is divided into four parts. The experiment has been carried out using a stable laser spot on the detector. Both the position and the intensity of the spot are measured several times and the noise is calculated for these measurements.

The setup of the system is changed for each part of the experiment to find out which optical components are contributing to the noise. The noise has been determined for

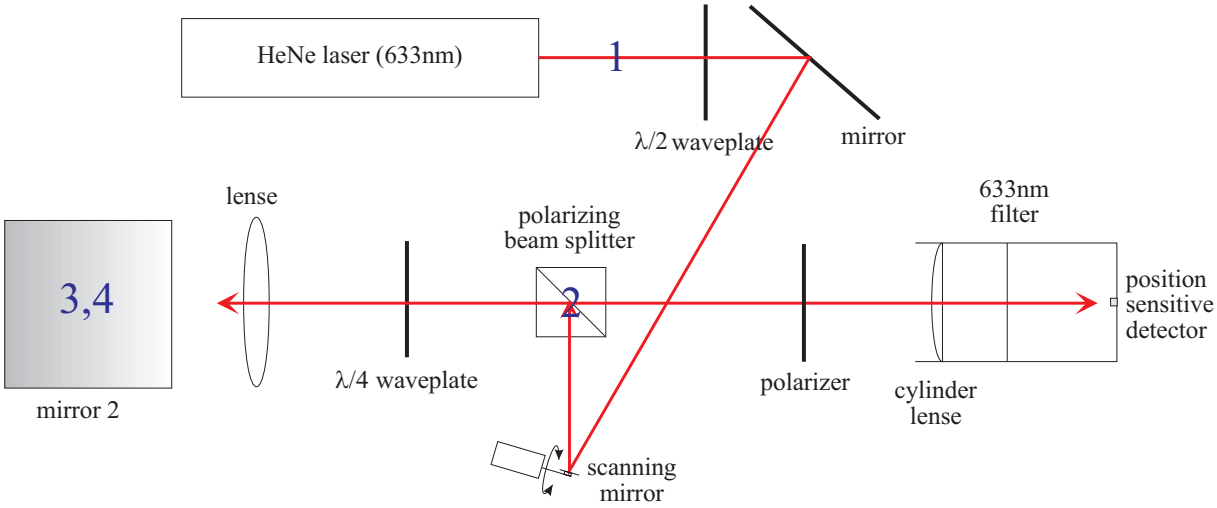

Figure 3.1: The different measurement setups.

1. the direct laser beam,

2. a reflection of the beam splitter,

3. a calibration mirror in the standard sample holder,

4. a sample in the evacuated oven.

The difference in the setup are illustrated in figure 3.1. The numbers given in the figure indicate, after which component the laser beam is analyzed.

The first measurement investigates the intrinsic noise of the detector and the laser. The laser is aimed directly at the detector, only the polarizer and the 633nm filter are in the beam path, the cylinder lens has been removed.

The second measurement shows the influence of the first important optical component, the scanning mirror, on the noise. During this measurement, the beam splitter has been turned around and the reflected light is no longer guided to the lens, but to the detector.

Third, the noise during a normal measurement setup is investigated. A very good mirror normally used for calibration purposes is positioned in the standard sample holder.

The fourth setup determines the noise of a sample in a different sample holder, the annealing unit, which is evacuated to find out whether additional noise is induced by the running pumps.

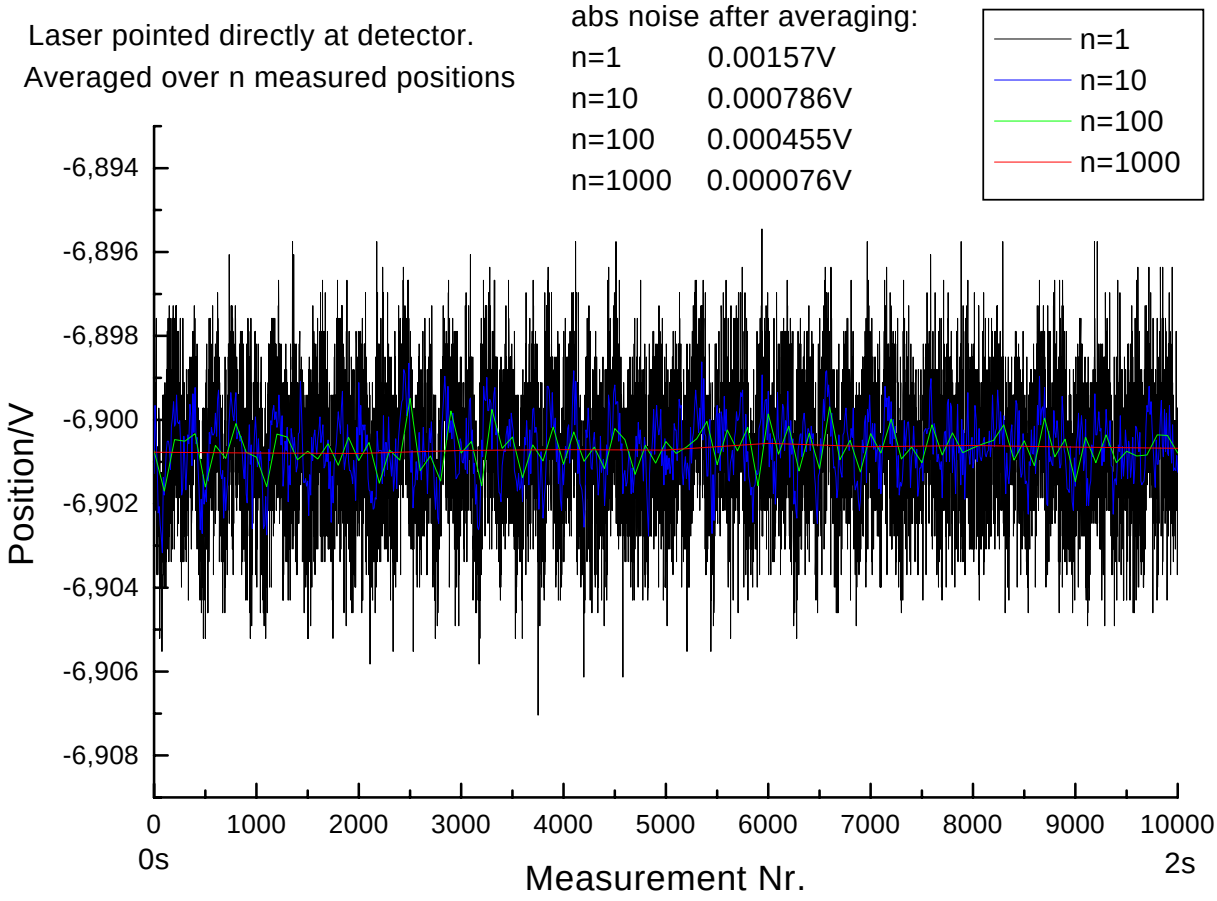

Figure 3.2: Noise of the laser and the detector, the position of a laser spot is measured 10000 times. The signal is averaged over 1, 10, 100 and 1000 values and plotted in the graph. The noise is calculated for each n.

3.1.1 Position noise

Noise of the direct laser beam

The noise of the detector and the laser are determined by pointing the laser directly towards the detector. The cylinder lens has been removed for this experiment, the 633nm filter and the polarizer are still in the beam path. The distance between the laser and the detector is about 15cm.

To measure the noise of the laser spot, the position was measured 10000 times, which takes about 2s. The measured values are plotted in figure 3.2.

The standard deviation of the measured signal is the noise, it amounts to 1.57mV. This equals to an actual position uncertainty of 0.94µm, since the detector has a size of 1.2cm and the voltage difference across the detector is 20V. The specifications of the detector give a resolution of 0.5mV or 0.3µm [1].

A simple way to reduce the noise is to average over several data points. As shown

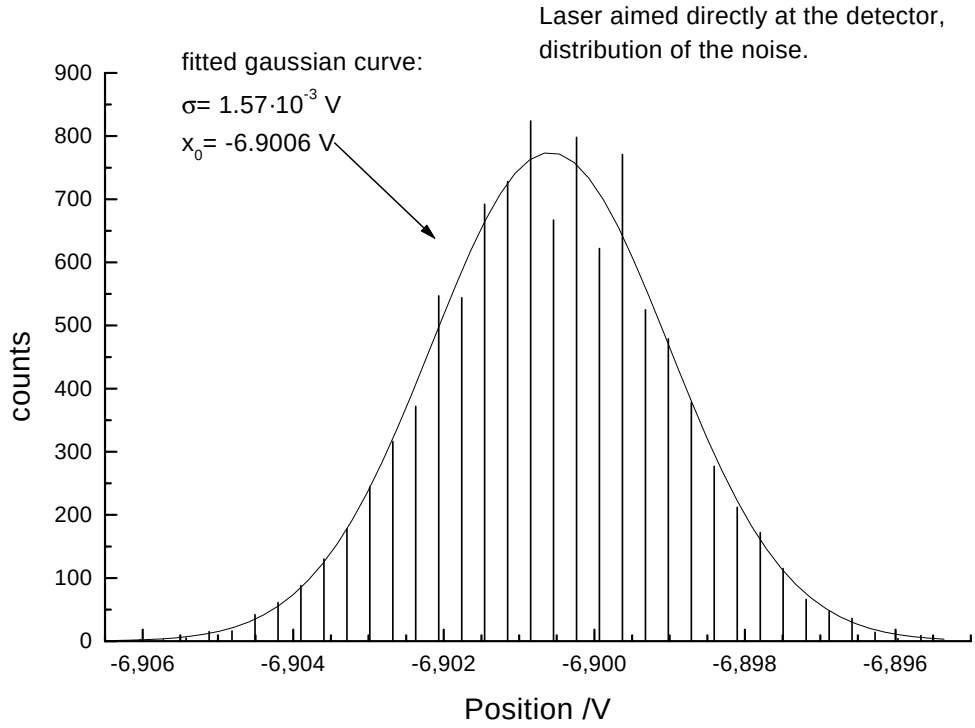

Figure 3.3: The distribution of the noise shows the quantization of the signal.

in figure 3.2, this is done for $n = 10$, $n = 100$ and $n = 1000$ data points. The noise decreases significantly with increasing n, but a measurement will take n times longer, when each point of data is measured n times. When the data is averaged over 100 data points, the noise level gets close to the specifications of the detector. At the moment, this value is used for actual measurements, because the noise is reduced and the measuring time is still low.

To get an insight into the nature of the noise, the distribution of the measured values is plotted in a histogram (figure 3.3). The quantization caused by the 16 bit resolution of the analog to digital converter (AD converter) becomes visible as the measured values are discrete lines. Since the position measurement yields a voltage between -10V and $+10$V, the theoretical accuracy of the AD converter is $3.05 \cdot 10^{-4}$V. This value is visible as the spacing between the discrete lines in the histogram. This value of this quantization is about 19.4% of the measured position noise.

The curve formed by the discrete points in the histogram can be modeled by a gaussian function with a standard deviation of 1.57mV. This suggest that the noise is gaussian distributed [11].

Unfortunately, this is not true, because otherwise σ_n, the standard deviation of the signal averaged over n following values, would fulfill the central limit theorem, which gives

$$\sigma_n = \frac{\sigma_1}{\sqrt{N}}.$$

n	calculated σ_n, as measured	calculated σ_n, randomized order	theoretical σ, $\sigma_n = \frac{\sigma_1}{\sqrt{N}}$
1	$1.57 \cdot 10^{-3}$V	$1.57 \cdot 10^{-3}$V	$1.57 \cdot 10^{-3}$V
10	$7.86 \cdot 10^{-4}$V	$5.13 \cdot 10^{-4}$V	$4.96 \cdot 10^{-4}$V
100	$4.55 \cdot 10^{-4}$V	$1.59 \cdot 10^{-4}$V	$1.57 \cdot 10^{-4}$V
1000	$7.64 \cdot 10^{-5}$V	$4.55 \cdot 10^{-5}$V	$4.96 \cdot 10^{-5}$V

Table 3.1: Comparison between the measured and calculated standard deviations.

The measured values for σ_n deviate significantly from this relation (see table 3.1).

To test the relation, the order of the data is randomized by a computer program and afterwards averaged again. The standard deviation σ_n is calculated again. As one can see in table 3.1, after the randomization of the order of the measured values, the σ_n match the theoretical values very well.

This analysis shows that there is a correlation between measured values following each other. Surprisingly, following values are more likely to have a bigger difference than two randomly picked values.

This result indicates that there is a periodic disturbance in the signal. To examine this, a fourier analysis is performed on the measured data. Prior to this, the average is subtracted from the signal and the signal is plotted over the time axis. [1]

The fourier analysis is done with the built in fast fourier transformation (FFT) functions of the computer program 'Origin', using a rectangular windowing function. The result of this analysis is shown in figure 3.4

This analysis shows a strong peak at 25Hz, which is presumably related to the laser or the electronics of the detector. There are also weaker peaks at 10Hz and 40Hz. Additional weak peaks at 50Hz and 100Hz are harmonics of the strong peak at 25Hz, but might also be caused by the power supply of the detector or the AD converter.

Noise using the different setups

After this short detour about the characteristic of the noise itself, the noise measurements using the different setups mentioned above are compared. The comparison between the different noise levels is shown in figure 3.5, exact values can be found in table 3.2.

The second setup determines the influence of the optical components on the noise. The original setup is changed by turning around the beam splitter. Now, the beam splitter directs the laser beam towards the detector. The noise increases significantly by a factor of 3.

[1] These steps are not essential, but the first step removes the peak at 0Hz, where the average of the signal is shown. The second step makes the interpretation of the data easier, since it makes sure that the x-axis of the resulting data is plotted in units of Hz.

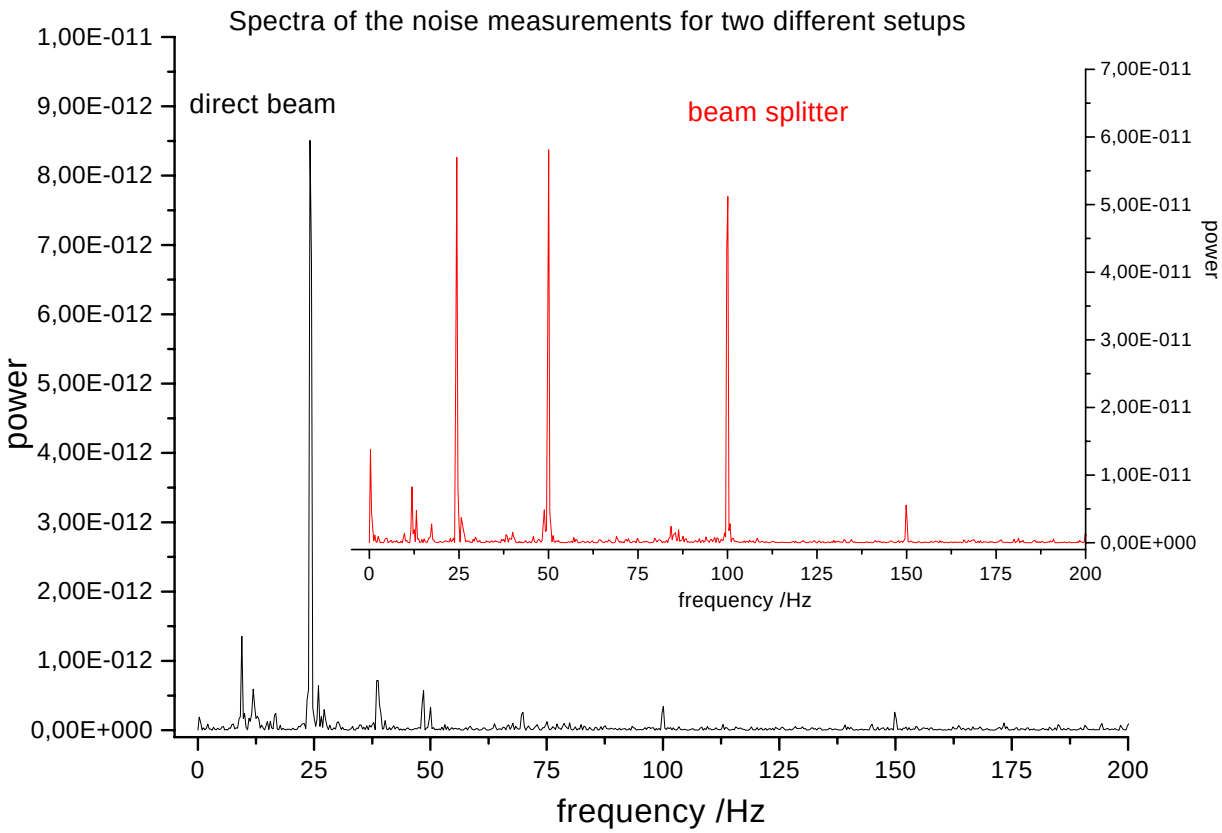

Figure 3.4: Spectra of the noise data for the first (direct laser beam) and the second (beam splitter) setup. The first spectrum (black) shows a strong peak at 25Hz, the latter (red) exhibits additional peaks at 50 and 100Hz.

To find out, whether this increase is related to the optical components or to turbulence of the air in the longer beam path, the setup is changed again. This time, the reflection of a calibration mirror positioned in the standard sample holder is monitored. The length of the beam path increases from circa 110cm to about 320cm. To decrease a possible influence of turbulence, the setup is covered with a box. In both cases, the noise level is about the same, the length of the optical path seems to have no influence on the noise.

This indicates that the main amount of the noise is related to the scanning mirror. When the frequency spectrum of this noise is plotted (figure 3.4), there are two additional strong peaks at 50Hz and 100Hz. This leads to the conclusion, that the DC power supply of the scanner is not filtering out the 50Hz net frequency well enough and the scanner is vibrating with this frequency and the harmonics of this frequency.

The last part of this experiment concerns the annealing unit. The standard sample holder is removed and a sample is placed inside the oven, which is evacuated next.

The noise increases dramatically by a factor of 6 compared to the first setup. The high amount of noise is presumably caused by the pumps attached to the vacuum

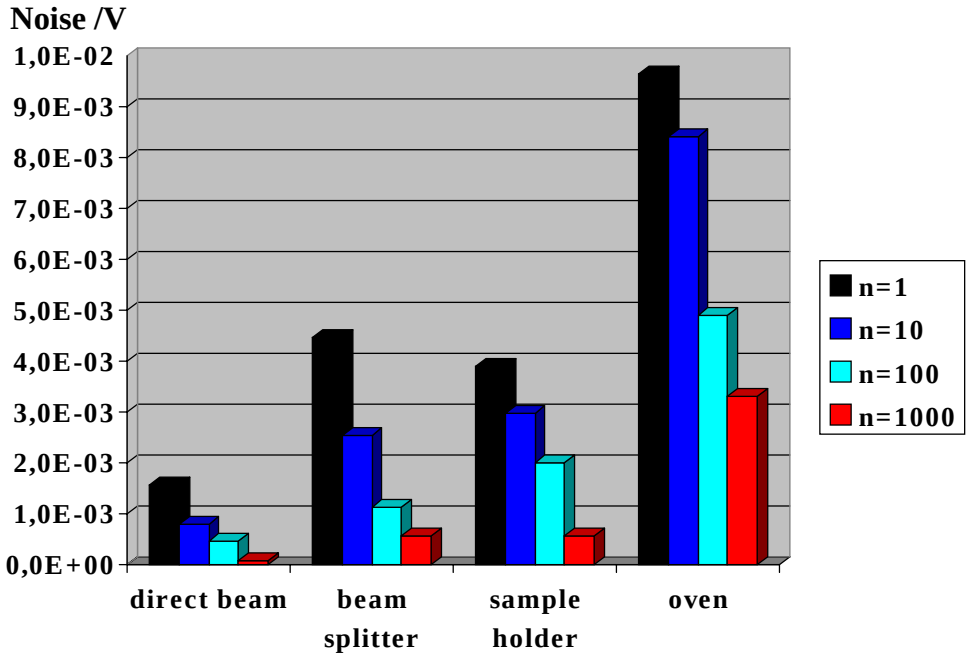

Figure 3.5: Comparison between the position noise measured using different setups.

n	σ, direct beam	σ, reflection of beam splitter	σ, reflection of mirror	σ, reflection of oven
1	$1.57 \cdot 10^{-3}$V	$4.46 \cdot 10^{-3}$V	$3.9 \cdot 10^{-3}$V	$9.63 \cdot 10^{-3}$V
10	$7.86 \cdot 10^{-4}$V	$2.54 \cdot 10^{-3}$V	$2.97 \cdot 10^{-3}$V	$8.4 \cdot 10^{-3}$V
100	$4.55 \cdot 10^{-4}$V	$1.14 \cdot 10^{-3}$V	$2 \cdot 10^{-3}$V	$4.89 \cdot 10^{-3}$V
1000	$7.64 \cdot 10^{-5}$V	$5.64 \cdot 10^{-4}$V	$5.67 \cdot 10^{-4}$V	$3.31 \cdot 10^{-3}$V

Table 3.2: Position noise using different setups.

chamber. Especially the mechanical pump is transmitting its vibrations via the tube towards the vacuum chamber.

3.1.2 Intensity noise

Although the primary goal of the system is the measurement of curvature, the intensity of the reflected beam may contain crucial information. A change in reflectivity can be observed e.g. during the switching of the switchable glasses or the phase transition of the phase change samples described in section 1.3.2 and section 1.3.2.

The intensity signal is recorded exactly the same way the position signal is, except for the fact that the sampling frequency of the AD converter is set to a different value during the intensity measurement. The intensity is determined 19000 times per second, while the position is measured only 5000 times per second. It takes therefore about 0.5s to record the intensity 10000 times. Apart from that, the experiment was performed the

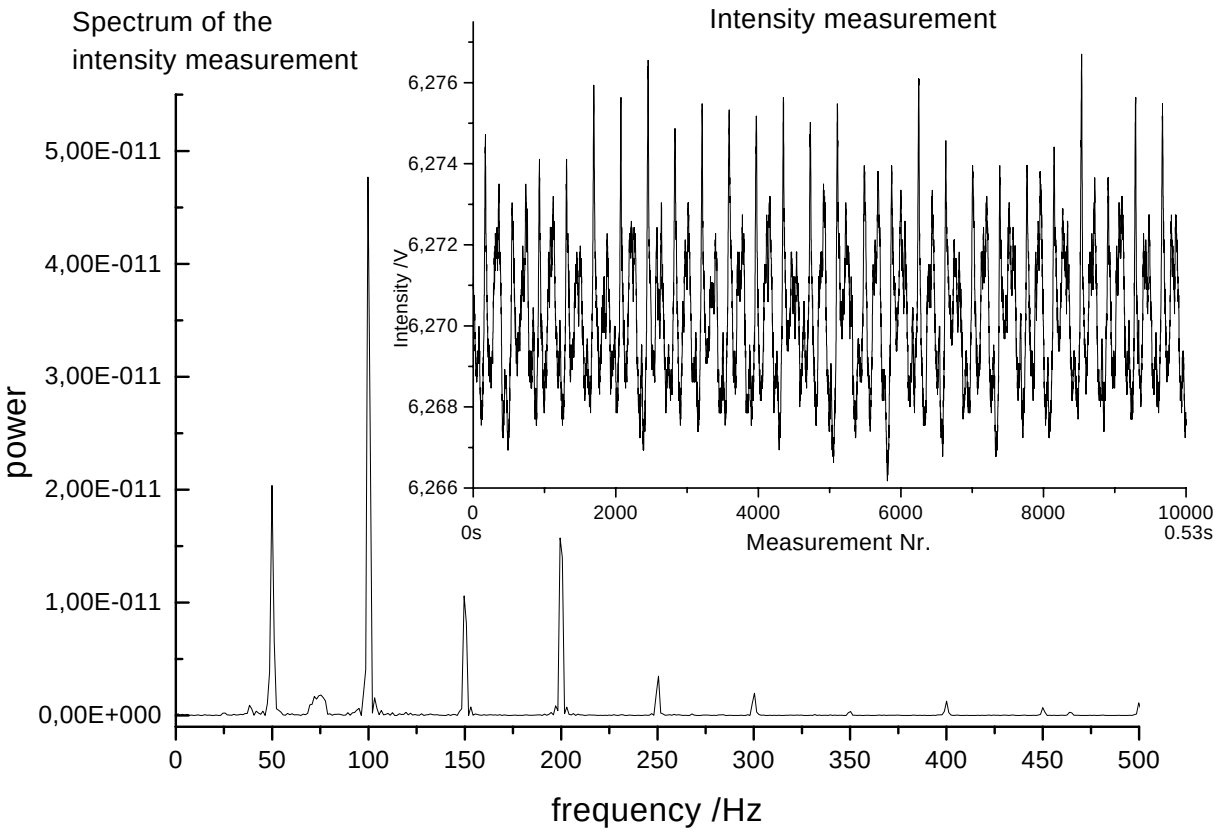

Figure 3.6: Intensity noise of the laser and the detector, the laser is pointed directly at the detector. The periodic nature of the signal is visible both in the plotted data and the spectrum. Two frequencies, 50Hz and 100Hz, are dominating the spectrum.

same way as the experiment for the position noise.

First, the laser is directed at the detector and the intensity of the laser beam is analyzed. When the data is plotted, an oscillation is visible in the graph. Figure 3.6 shows both the recorded intensity values and the spectrum of the noise. By frequency analysis two frequencies are found in the signal, one at 50Hz and one at 100Hz. The peak at 100Hz is much stronger than the peak at 50Hz, which suggests that it is not just a harmonic vibration caused by the 50Hz oscillation. The other peaks in the spectrum are presumably harmonics of the first two peaks.

The oscillation with the frequency of 100Hz is caused by the fluorescent lamps in the room, it disappears, when the light is turned off [33].

Table 3.3 contains the noise values of the different setups for different averaging coefficients n.

A comparison between the different intensity noise measurements yields no difference to the behaviour of the position noise. Again, the reflection of the mirror in the standard sample holder and the reflection of the beam splitter are showing the same amount of noise. The signal of the scanned sample in annealing unit has a higher noise

n	σ, direct beam	σ, reflection of beam splitter	σ, reflection of mirror	σ, reflection of oven
1	$1.71 \cdot 10^{-3}$V	$2.66 \cdot 10^{-3}$V	$2.2 \cdot 10^{-3}$V	$7.64 \cdot 10^{-2}$V
10	$1.68 \cdot 10^{-3}$V	$2.64 \cdot 10^{-3}$V	$2.13 \cdot 10^{-3}$V	$6.21 \cdot 10^{-2}$V
100	$9.96 \cdot 10^{-4}$V	$1.74 \cdot 10^{-3}$V	$1.27 \cdot 10^{-3}$V	$2.45 \cdot 10^{-2}$V
1000	$1.18 \cdot 10^{-4}$V	$4.40 \cdot 10^{-4}$V	$3.91 \cdot 10^{-4}$V	$9.45 \cdot 10^{-3}$V

Table 3.3: Intensity noise using the different setups.

level which is related to the same problems as mentioned above.

Interestingly, the averaging does not decrease the noise level as well as it does in case of the position noise. This is clearly related to the fact that the data is collected much faster. The period of a 50Hz oscillation equals to 380 data points. It is therefore impossible to decrease the noise by averaging over 10 or 100 data points. Because of this, the noise level of the intensity is higher than the noise of the position.

3.2 Long term noise during a measurement

After the noise of a fixed laser spot on the detector has been analyzed, the noise during a measurement is investigated. During this experiment, the laser beam scans over a mirror placed in the standard sample holder. This mirror is a high quality mirror used for calibration purposes, and has a well known curvature of 20m $\pm$2%.

The measurement is started in the afternoon and runs overnight. To make sure that the conditions of the room do not change too much during the measurement, the light is left on. To reduce air movement in the optical path, a box is mounted over the experimental setup. The table is not protected against vibrations.

The curvature of the mirror is well known and the distribution of the curvature is homogeneous over the mirror. Influences of the linear regression described in section 3.5 are therefore excluded. The result of this experiment is shown in figure 3.7, the measured curvature is plotted agains the time.

The measurement is started at 15:43 in the afternoon and runs for 19h until 10:30 the next morning. In the first three hours, the laboratory was still in use by somebody working on a different experiment. The noise level is about 0.5% during this time. After the last person has left the laboratory, the noise level drops significantly to about 0.07%.

Over the first 15h, the measured value increases slowly by 0.3% from 20.03m to 20.09m. Within the last two hours it decreases slightly again. In the next morning, around 9:00, the laboratory is in use again, the noise increases again to the same level as in the afternoon.

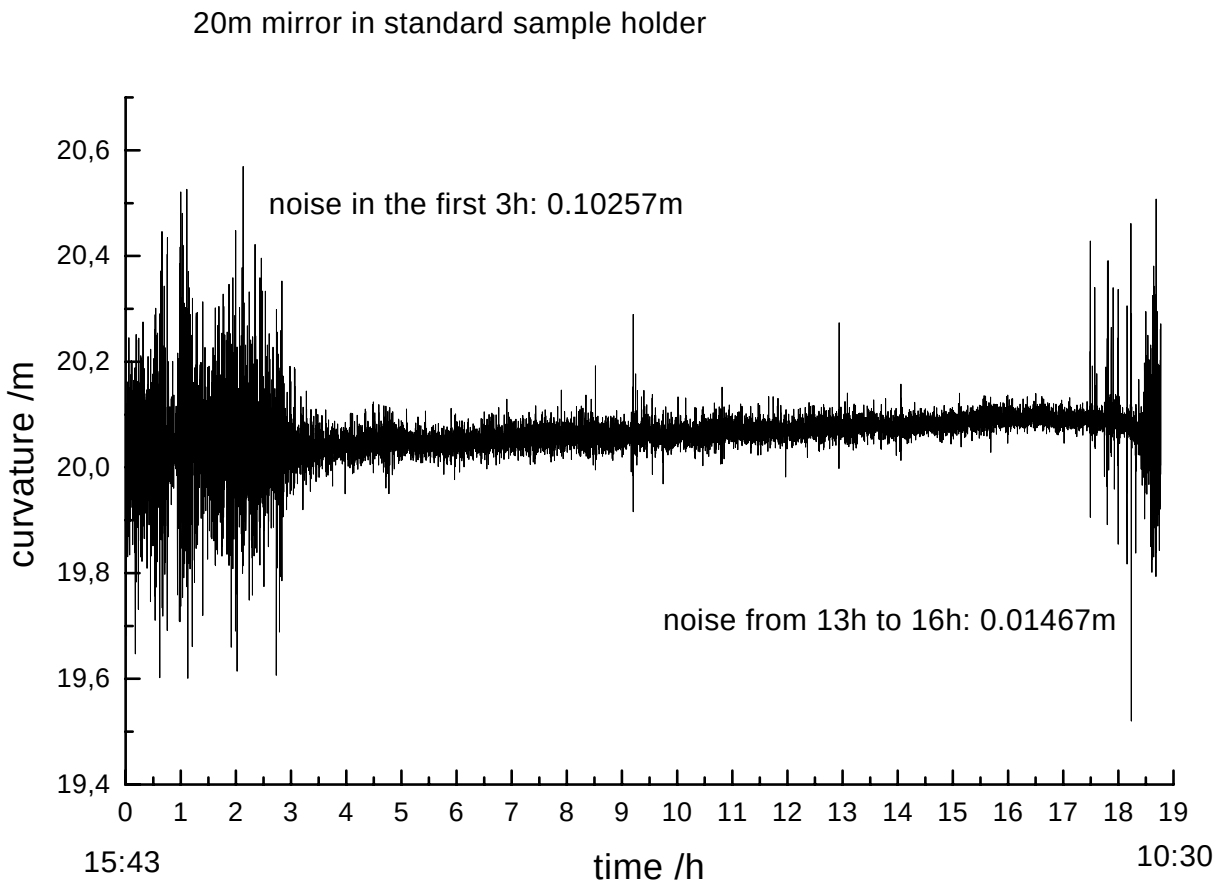

Figure 3.7: A long term measurement of the curvature of the 20m calibration mirror.

3.3 Influence of reflections on a measurement

It is important to investigate the possible influence of reflections on the measurements, since a lot of reflections are visible in the setup. These reflections appear at every glass-air interface in the system, e.g. at the lenses, the beam splitter and even the sample, if it is transparent.

The setup for this experiment is the same as for a normal measurement, except for the fact that the beam is stopped behind the beam splitter using non reflective black cardboard. During this experiment, a beam splitter without anti reflection coating is used and scanned by the laser beam.

At the glass air interfaces of the beam splitter, the laser beam is reflected and leaves the beam splitter in direction of the detector. The reflection is monitored by the detector and has an intensity of 0.055V. A second laser (also a HeNe laser with $\lambda = 633$nm) is positioned next to the beam splitter and is aimed at the detector. The position of this laser spot is fixed, the intensity of this laser can be adjusted using a linear variable filter.

Since the reflection of the beam splitter is moving due to the scanning beam, it

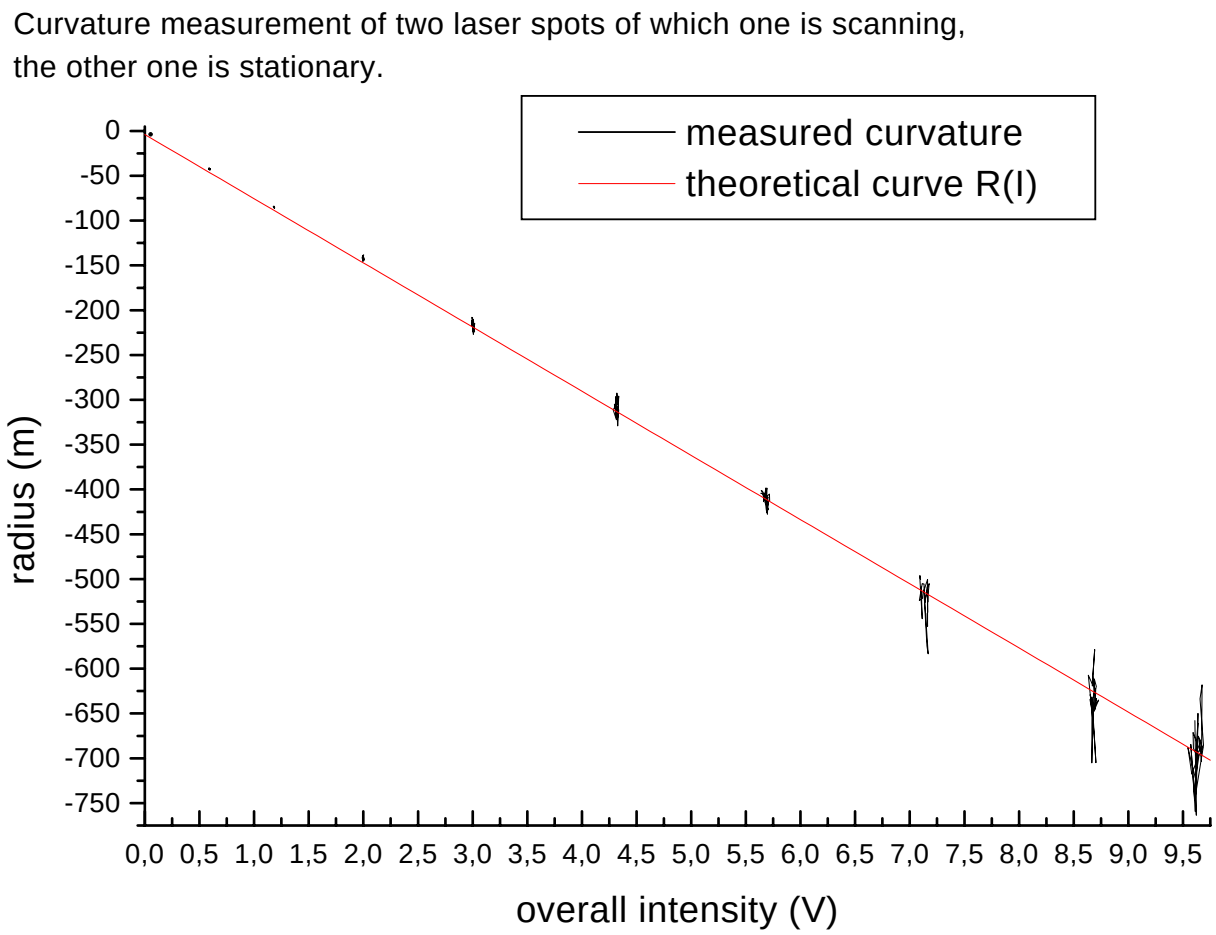

Figure 3.8: Measured curvature of two laser spots competing on the detector. One spot of 0.055V intensity scans over the detector, while the intensity of a second, stationary spot is changed.

causes a straight line in the position/scan position diagram, which is interpreted as a curvature of radius -3.95m.

The idea of this experiment is to slowly increase the intensity of the stationary laser spot and to analyze its influence on the measured curvature. The measured data is shown in figure 3.8. The curvature is plotted over the overall intensity as measured by the detector. For each intensity, the curvature is determined 25 times.

When the intensity of the stationary laser spot increases, the influence of the reflection decreases. The position of the two spots on the detector is averaged with respect to the intensities. When the intensity of the second laser is increased, the weight of the scanning spot decreases and the scanned area on the detector seems to be reduced, too. As a result, the line in the position/scan position diagram looks flatter and the calculated curvature is increasing. The linear regression gets more sensitive to noise when the gradient of the line decreases and the noise increases (see also section 3.5). Since the measurement was done without the box, the noise level is quite high.

The radius of the curvature is calculated by

$$R(I) = \frac{c}{g(I)},$$

with $g(I)$ as the gradient in variation of the changing intensity I of the stationary laser. The gradient $g(I)$ is given by

$$g(I) = g_0 \cdot \frac{I_0}{I + I_0},$$

I_0 is the intensity of the scanning laser and g_0 the measured curvature caused by the scanning beam. This takes into account that the resulting position of two separate laser spots is the average of each position weighted with respect to the intensities. This results in a linear relation between the curvature and the intensity of the stationary laser:

$$R(I) = c \cdot \frac{I + I_0}{I_0 \cdot g_0}. \tag{3.1}$$

The constant during the measurement is $c = 35.71\ \mathrm{mVcm^{-1}}$, the measured intensity of the scanning beam is $I_0 = 0.055\mathrm{V}$ and the measured gradient caused by the scanning beam is $g_0 = -9.06\mathrm{Vcm^{-1}}$. When these values are used in the equation, the calculated line shows a good agreement between the theoretical values and the actually measured values (see figure 3.8). This indicates that the simple model used above is correct.

The influence of the scanning reflection is still visible at the upper intensity limit of the detector. The ratio of intensity of the two laser spots is 200 at this point. The influence disappears, when the filter used to control the intensity is removed completely. It is not possible to determine the intensity of the laser beam at this point since the intensity is too high to be measured by the detector.

Using equation 3.1, it is as well possible to analyze the influence of a reflection on a measurement. This time, the unwanted reflection has a stable position on the detector, whilst the reflection of the sample is scanning over the detector. The intensity of the beam, which is reflected by the sample is I_0, the intensity of the unwanted reflection is $x \cdot I_0$. Using equation 3.1, these values give

$$\begin{aligned} R(I) &= c \cdot \frac{I_0 \cdot (x+1)}{I_0 \cdot g_0} = c \cdot \frac{x+1}{g_0} \\ &= R_0 \cdot (x+1). \end{aligned}$$

For example, when the 20m calibration mirror is analyzed and a reflection, which has an intensity of 10% of the intensity of the beam reflected by the mirror, the actual measured curvature will be

$$R(I) = 20\mathrm{m} \cdot (1 + 0.1) = 22\mathrm{m}.$$

3.4 Results of the characterization of the noise and the reflections

The noise measurements show that the noise level of the system can be as low as indicated in the specifications of the detector.

The measurements also show that some of the components seem to have a strong influence on the noise. The scanning mirror is responsible for a main part of the noise. Its power supply should be changed or an additional filter blocking out the net frequency of 50Hz should be added.

The noise can be reduced further by averaging over more data points. If the measuring time for each position and intensity value is longer than the time of one period of the disturbing frequencies, this will help to decrease the effect of this disturbance on the measurement. I would suggest to average over 400 values, the measurement is still very fast, it takes 0.08s to collect these values and it equals to a frequency of 12.5Hz. This is especially important for the intensity measurement. Here, the sampling rate should be reduced to average over a longer time and an averaging over 0.04s (this equals to 25Hz) should help to reduce the noise of the intensity measurement.

The annealing unit showed a very bad performance concerning the noise caused by vibration of the mechanical pump. To remove this noise, the tube connecting the pump with the vacuum chamber has been fixed to a block of concrete. The vibrations cannot get across the massive block and the noise has decreased significantly. According to [33], the noise level of the annealing unit is the same as it is for the other setups.

The long term measurement shows a very low noise and a very stable system, which makes it possible to measure one value over a long time without inconsistencies. It also shows that the system is very sensitive to vibrations in the room. These problems can be fixed by using better vibration protection for the optical table like air cushions underneath each of its legs. It would also help to have a separate room for the experiment or a better optical table. Essential for a good measurement is also the box to prevent turbulence of the air.

The result of the experiment concerning the reflections is clear, it shows that it is crucial for a good setup to remove all reflections. A single reflection on the detector can destroy a measurement by changing the measured curvature significantly, especially when the intensity on the detector is low and the observed curvature is low (has a high radius).

Removal of the reflections can be done with various approaches. It is possible to block out reflections, suppress them or make sure they do not reach the detector.

- Black cardboard around the beam splitter is used to block out any beams that are not passing it. The inside of the box containing the detector is also covered with black cardboard to prevent unwanted reflections from the walls.

- All of the optical components have been replaced by components with anti reflection coating to suppress reflections.

- To redirect reflections, the lenses have been tilted a bit horizontally to make reflections leave the optical path.

An interesting fact is that the detector itself reflects the incoming beam back onto the cylinder lens where it is reflected back towards the detector again. This problem could be solved by tilting the detector slightly.

3.5 Influence of the linear regression on the measured curvature

This section covers issues concerning the linear regression algorithm. Both the quality of the samples and the position noise have an influence on the calculation of the curvature, which is discussed in the next two subsections.

3.5.1 The quality of the sample curvature and its influence on the measurement

As outlined in section 2.2, the ratio between the scanned length Δx on the detector and the scanned length on the sample Δs is used to calculate the radius of the curvature of the sample:

$$\frac{\Delta x}{\Delta s} = \frac{2f}{R}$$

The position s of the laser beam on the sample is well known, it is controlled by the scanner. The position x of the reflection on the detector is measured. The ratio between the two values is determined by a linear regression.

Figure 3.9 shows x as a function of s and the resulting linear regression for two different samples, a calibration mirror and a sample (Ti on Si).

The left figure shows the data of the calibration mirror. The recorded data is a straight line, indicating that the mirror has a homogeneously curved surface. The linear regression gives a gradient of $g = 1.62\text{Vcm}^{-1}$. The error of the linear regression is calculated to $\sigma = 0.02\text{Vcm}^{-1}$, this equals to 1.2%.

In the right figure, the data of the sample are shown. The plot is not linear over the whole scanned length, it has a twisted form. This shape of the curve shows that the sample is not curved as expected.

It is difficult to analyze a sample with such a shape, since it depends on the analyzed area of the sample, what the result of the linear regression is. When the gradient is calculated for the whole set of data, the gradient equals to $g = -0.66\text{Vcm}^{-1}$. The error is high, $\sigma = 0.04\text{Vcm}^{-1}$, this corresponds to a relative error of 6.1%.

When the scanned length is reduced to the data points 9-16, which equals to a scan size of $s = 0.75$cm, the linear regression gives a gradient of $g = -1.11\text{Vcm}^{-1}$, with a relative error of 3.4%.

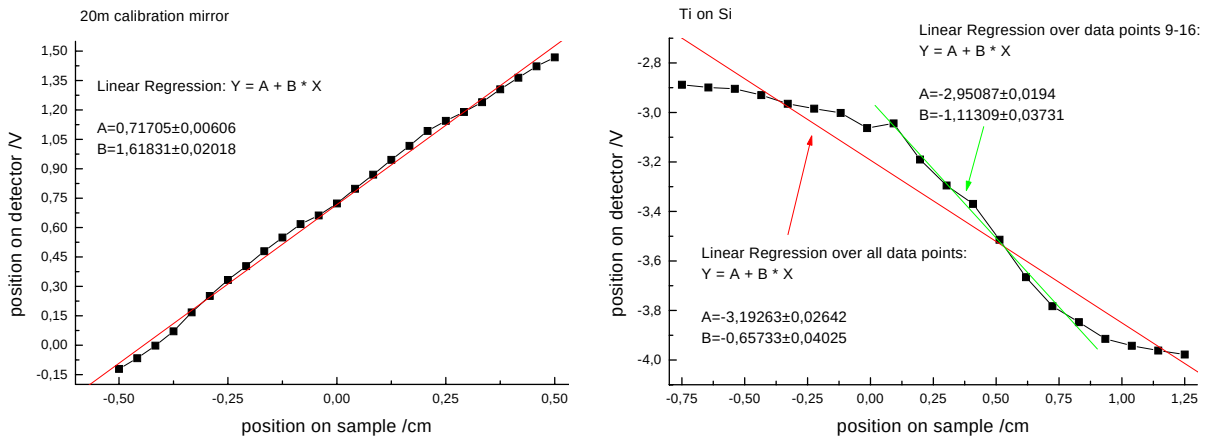

Figure 3.9: The position of the reflected beam is shown as a function of the position of the laser beam on the sample. The left figure shows a mirror, the right figure a sample (Ti on Si).

Regarding the strange shape of samples analyzed here, it is possible to measure any curvature by changing the scanned area on the sample. Nevertheless, quantitative measurements are still possible. As long as the scanned area does not change during the measurement, the recorded values of the curvature are consistent.

Assuming that the shape of the samples is solely caused by the shape of the substrates prior to deposition, theoretically even a stress analysis using Stoney's equation (equation 1.3) can be performed on these samples. Nevertheless, the use of samples with a good shape and homogeneous curvature is essential for reproducible measurements.

3.5.2 Influence of the position noise on the linear regression

The position noise determined in section 3.1 limits the measurable curvature. The lower the ratio between the movement of the reflected beam on the detector and the scanned length, the more sensitive is the calculation of the gradient and the curvature on the noise of the measured position.

The position of the reflection a_i is measured for each scanning position x_i and the gradient g is determined by a linear regression. The theoretical position of the reflection y_i calculates as

$$y_i = \alpha + g \cdot x_i, \qquad i = 1, \ldots, N. \tag{3.2}$$

The average error m of each measured value a_i is determined by

$$m = \sqrt{\frac{\sum_{i=1}^{N} (a_i - y_i)^2}{N-2}}.$$

y_i are the values calculated using equation 3.2. The error of α calculates to

$$m_\alpha = m \cdot \sqrt{\frac{\sum_{i=1}^{N} x_i^2}{N \cdot \sum_{i=1}^{N} x_i^2 - \left(\sum_{i=1}^{N} x_i\right)^2}}.$$

The error of g equals to

$$m_g = m \cdot \sqrt{\frac{N}{N \cdot \sum_{i=1}^{N} x_i^2 - \left(\sum_{i=1}^{N} x_i\right)^2}} = \sqrt{\frac{\sum_{i=1}^{N} (a_i - y_i)^2}{(N-2) \cdot (\sum_{i=1}^{N} x_i^2 - \frac{1}{N} \cdot \left(\sum_{i=1}^{N} x_i\right)^2)}}. \tag{3.3}$$

The parameter used for the determination of the sample curvature is the gradient g. The error m_g is therefore analyzed further.

A relation between this error and the position noise during a measurement is derived. Using this equation, the influence of the noise on the error of the gradient can be determined. Using this, it is possible to calculate the error of the curvature. Assuming a perfect measurement system including a perfectly curved sample, the error of the gradient is zero, the measured values a_i are equal to their theoretical values y_i. When the position noise is no longer zero, but has a value of σ, the measured values a_i deviate from y_i:

$$a_i = y_i \pm \sigma$$

The values x_i, each describing the position of the scanning beam on the sample during measurement step number i, are well known. With the length of the scan x_m, these positions calculate as

$$x_i = \frac{x_m \cdot (i-1)}{N-1}.$$

Using equation 3.3, the error of g transforms to:

$$\begin{aligned} m_g &= \sqrt{\frac{\sum_{i=1}^{N} \sigma^2}{(N-2) \cdot \sum_{i=1}^{N} x_i^2 - \frac{N-2}{N} \cdot \left(\sum_{i=1}^{N} x_i\right)^2}} \\ &= \sqrt{\frac{N \cdot \sigma^2}{(N-2) \cdot \sum_{i=1}^{N} x_i^2 - \frac{N-2}{N} \cdot \left(\sum_{i=1}^{N} x_i\right)^2}} \end{aligned}$$

$$\begin{aligned}\sum_{i=1}^{N} x_i^2 &= \sum_{i=1}^{N} \left(\frac{x_m \cdot (i-1)}{N-1}\right)^2 = \left(\frac{x_m}{N-1}\right)^2 \cdot \sum_{i=0}^{N-1} i^2 \\ &= \left(\frac{x_m}{N-1}\right)^2 \cdot \frac{N \cdot (N-1) \cdot (2N-1)}{6} \\ &= x_m^2 \cdot \frac{N \cdot (2N-1)}{6(N-1)}\end{aligned}$$

$$\begin{aligned}\left(\sum_{i=1}^{N} x_i\right)^2 &= \left(\frac{x_m}{N-1} \cdot \sum_{i=0}^{N-1} i\right)^2 \\ &= \left(\frac{x_m}{N-1} \cdot \frac{N \cdot (N-1)}{2}\right)^2 \\ &= x_m^2 \cdot \frac{N^2}{4}\end{aligned}$$

$$\begin{aligned}\Rightarrow m_g &= \sqrt{\frac{N \cdot \sigma^2}{(N-2) \cdot \sum_{i=1}^{N} x_i^2 - \frac{N-2}{N} \cdot \left(\sum_{i=1}^{N} x_i\right)^2}} \\ &= \sqrt{\frac{N \cdot \sigma^2}{(N-2) \cdot x_m^2 \cdot \frac{N \cdot (2N-1)}{6(N-1)} - \frac{N-2}{N} \cdot x_m^2 \cdot \frac{N^2}{4}}} \\ &= \frac{\sigma}{x_m} \cdot \sqrt{\frac{12(N-1)}{(N-2)(N+1)}}\end{aligned} \tag{3.4}$$

Using equation 3.4, it is possible to calculate the error of the linear regression m_g for a given noise σ and a given number of steps N.

The position noise of each step during a typical measurement setup has been determined according to table 3.2 as $\sigma = 2 \cdot 10^{-3}\text{V} = 1.2\mu\text{m}$. Typical values for the length of the scan and the number of steps per scan are $x_m = 2\text{cm}$ and $N = 20$.

Using these values, the error of the linear regression results to

$$m_g = \frac{1.2\mu\text{m}}{2\text{cm}} \cdot \sqrt{\frac{38}{63}} = 4.66 \cdot 10^{-5}$$

The error of the calculated gradient should be low compared to the gradient g itself. Assuming a relative error of less or equal than 10%, the gradient calculates as

$$g \geq 10 \cdot m_g = 4.66 \cdot 10^{-4}.$$

This corresponds to a curvature of

$$R = \frac{2f}{g} \leq \frac{2 \cdot 1.016\text{m}}{4.66 \cdot 10^{-4}} \leq 4361\text{m}.$$

Using the measurement parameters listed above, the radius of the sample has to be lower than 4361m to limit the statistical error of the gradient caused by the position noise to less than 10%.

This error of the linear regression can be lowered by increasing the number of steps per scan and the scanned length, allowing analysis of samples with a lower curvature.

3.6 Characterization of the gas cell

This section describes a measurement that has been carried out to characterize the gas cell.

The gas cell is going to be used for stress measurements of samples covered with a switchable coating. To switch these coatings, the gas cell is evacuated first to remove the oxygen in the cell. Then, the sample is exposed to a pressurized gas containing hydrogen, which causes the sample to change its properties. To reverse this process, the gas cell is evacuated again to remove the hydrogen and, after that, flushed with air. A measurement consists of several of these pressure cycles.

To test the gas cell, such a measurement has been carried out using a thin glass substrates without any coating. This substrate is 150µm thick.

The result is shown in figure 3.10. Both the curvature (black curve) and the intensity (red curve) are plotted against time. Additionally, the three different atmosphere and pressure conditions are shown. The hydrogen pressure is 2026mbar, the air is not pressurized and the pressure of the vacuum is less than 10mbar. From left to right, the state of the cell is changed from H_2 via vacuum to air and back via vacuum to H_2.

The intensity shows an interesting behaviour. When the H_2 is pumped out of the gas cell, the intensity increases dramatically. When vacuum is applied to the cell, the intensity shows some kind of relaxation and decreases again. When air is filled in, the intensity stabilizes at a high level. The intensity increases again when vacuum is applied to the gas cell and drops, when H_2 is filled in. The different levels of the intensity are changing from time to time, but the H_2 level is always lower than the air level.

The curvature changes too, but the change is not as clear as for the intensity. The curvature shows a peak each time the pressure inside the cell is changed.

These results are surprising, since the glass analyzed is not coated and should not change at all during the experiment. Presumably, the reason for this behaviour is the fact that the position of the reflected beam moves when the pressure state changes. This is related to a movement of the sample caused by the pressure shock.

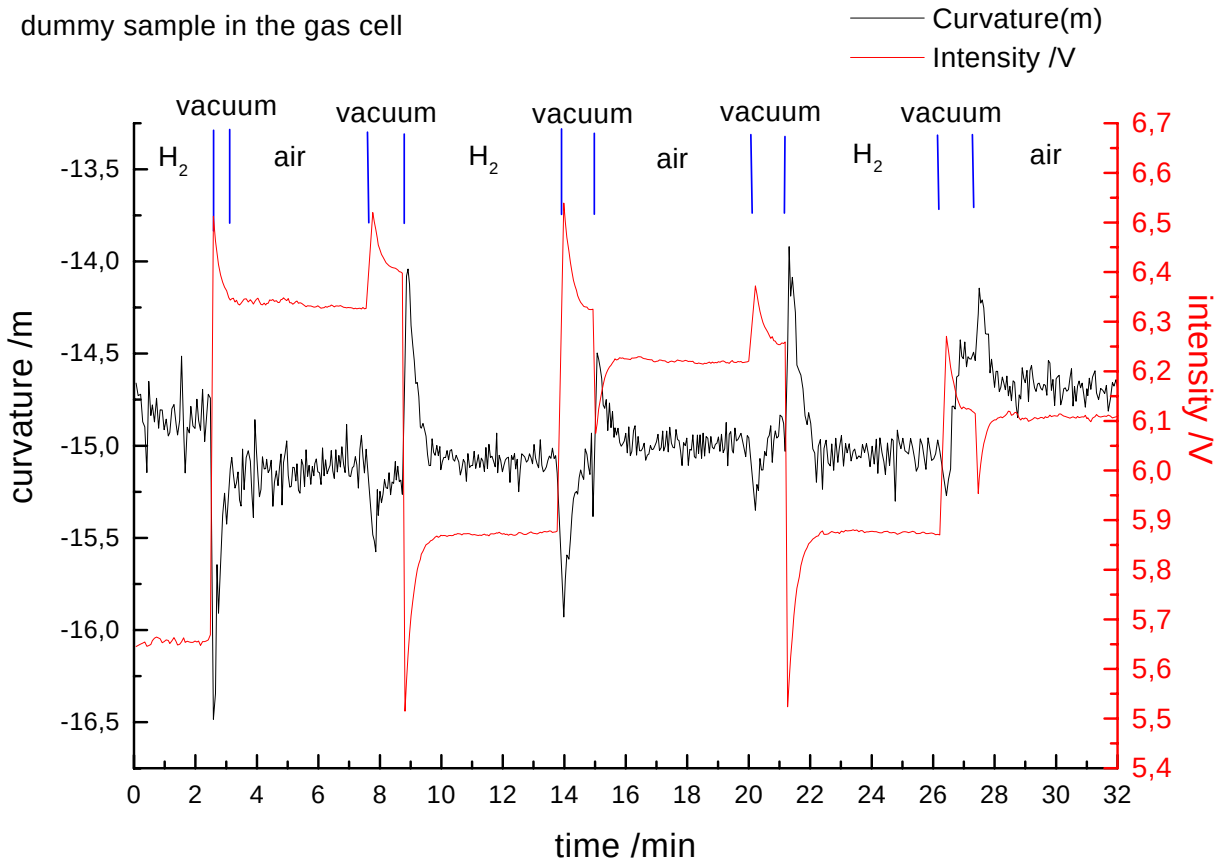

Figure 3.10: A measurement using an uncoated sample shows changes in the intensity and curvature caused by the different pressure states inside the gas cell.

3.7 Characterization of the annealing unit

A similar experiment has been carried out using the annealing unit. A silicon substrate has been annealed to 200°C, while the curvature has been measured. In figure 3.11, the measured curvature is plotted against the temperature.

Although the curvature should remain constant over time and temperature, it increases from its starting value of −21.8m to −16.5m at 180°C. During further annealing, it decreases slightly. When the radiators in the annealing unit are turned off, the temperature decreases, while the curvature stays constant. When the sample is cooled down to 125°C, the curvature starts to increase until it reaches −16.3m at 65°C. Back at room temperature, the curvature has the same value it had prior to the annealing process.

As mentioned above, the curvature of the sample should not vary during this experiment since it consists of a single crystalline substrate which has not been coated. There seems to be no clear correlation between the curvature and the temperature, the change of curvature during annealing is different from that during cooling.

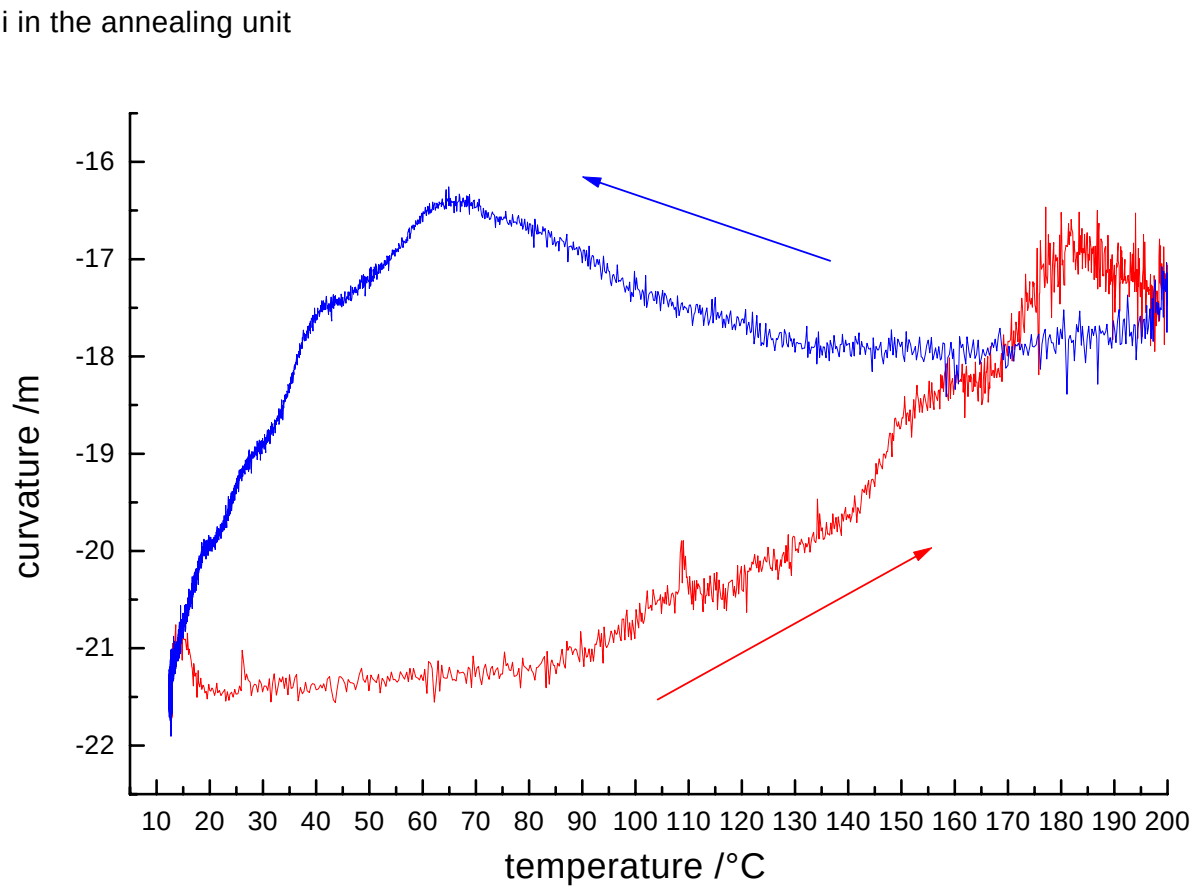

Figure 3.11: A piece of a Si wafer is annealed in the oven. The measured curvature changes with respect to the temperature. The data collected during heating up are plotted in red, during cooling, they are plotted in blue.

The reflected beam moves during the measurement. To test, whether the change of curvature is related to this drift, the curvature is plotted for the different position of the reflection on the detector (figure 3.12). The beam position is determined by the position of the reflection on the detector during the first step of each scan.

There seems to be a correlation between the curvature and the beam position. Depending on the position of the reflection on the detector, the curvature changes.

It is clear that any vertical drift of the reflection on the detector has an immediate influence on the measured curvature, since the additional drift is added to the movement of the reflection caused by the scanning procedure and is accounted for during the calculation of the curvature.

On the other hand, it is obvious that this effect can not cause the change of curvature observed in this case. The main reason for this is, that the change of curvature is much higher than the component caused by the drift measured in this experiment. Another hint is the fact, that the change of curvature as plotted in figure 3.12 can be both positive or negative for a positive change of position. When the position changes from -2.8cm

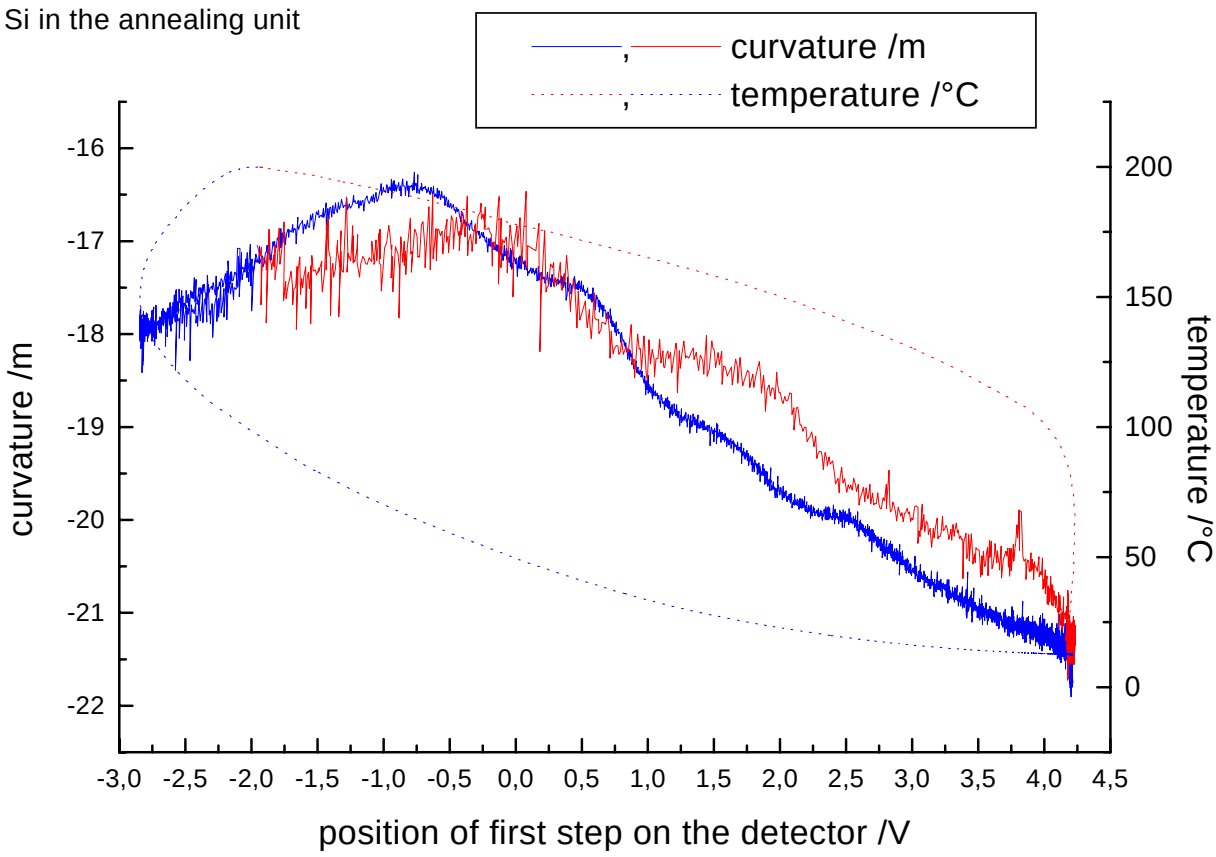

Figure 3.12: The curvature and the corresponding temperature are plotted over the position of the beam on the detector. The data collected during heating up are plotted in red, during cooling, they are plotted in blue.

to -0.8cm, the curvature increases, when the position changes further, the curvature decreases. If the change of curvature would be solely caused by the effect mentioned above, this behaviour would not appear.

The unexpected change of the curvature during the annealing process is therefore related to the drift, but it is much bigger than expected. This leads to the conclusion that either the detector does not work homogeneously, or the setup is misaligned.

3.8 Results of the investigations on the gas cell and the annealing unit

Both the gas cell and the annealing unit are still exhibiting some problems prohibiting good measurements.

When the gas cell is evacuated or filled, there is a pressure shock moving the sample for a moment. When the pressure is stable again, the position of the reflected beam

has changed slightly and as a result, the detected intensity and curvature varies with respect to the former value. Since it is not possible to fix the sample in order to measure the change in stress truly, it is hard to solve this problem.

There are two ways of eliminating this effect:

- slow down the pressure change to eliminate sample movement
- make sure that a change of the position of the reflected beam does not affect the measured intensity and curvature.

The pressure change was already slowed down by a narrow valve. By closing this valve even further, the pressure shock can be smoothed out. This affects of course the time resolution of the system, which should be in the scale of several seconds [39].

The second point is a much more powerful solution. Actually there is no good reason why a change in the position of the reflected beam affects the intensity or curvature. The cylinder lens should take care of horizontal movements and the detector should be homogeneous over the whole length.

One possibility is that the detector's axis is not absolutely parallel to the one of the cylinder lens. When the incoming beam is focused onto the detector in one point, a different beam vertically moved is focused to a different point next on the detector. Since the detector is very thin, this is presumably the case.

A solution would be to substitute the detector against a bigger one. The best solution would actually be to have a bigger detector so that the cylinder lens could be removed. A CCD camera could serve as the detector while a computer analyzes the image and calculates the position of the laser spot.

Another problem concerning the measurements is that the scanned area of the sample might change a bit when the sample moves. Since the samples often have an inhomogeneous curvature and a 'potato chip' shape, the measured curvature is changed when the scanned area changes. The solution to this problem is easy, better substrates should solve it immediately.

In the oven, there is a similar problem, when the copper block is heated up, it moves or is deformed by the temperature. The most likely cause of this are the three legs on which the copper block is positioned. Two of them consist of identical micrometer screws, while the third leg is fixed flexibly to the bottom of the vacuum chamber. The legs are presumably heated up and expanding differently, when the oven is used.

The problem can be fixed in two ways:

- stop the movement of the sample
- make sure that a change of the position of the reflected beam does not affect the measured intensity and curvature.

The first approach would be a redesign of the annealing unit or parts of it. An easy solution would be to separate the annealing part and the sample holder.

The second possibility is the same as mentioned above concerning the gas cell. It should therefore be solved with highest priority.

Chapter 4

Results

The characterization of the wafer curvature apparatus has shown that some improvements are necessary until good measurements can be performed on this system.

Nevertheless, it is possible to carry out measurements using the gas cell and the annealing unit. Such a measurement does not yield any quantitative information yet, but it can be used to investigate, whether the samples described in subsection 1.3.2 and 1.3.2 exhibit any measurable effects.

Two experiments using these samples are analyzed in the next sections. First a glass substrate covered with a switchable coating is investigated in the gas cell. Second, a phase change sample is annealed in the oven.

4.1 A measurement using the gas cell

This experiment has been carried out using a thin glass substrate (150µm) covered with a thin WOx layer (375nm) and a layer of palladium (Pd) serving as a catalyst.

Section 3.6 shows that measurements using the gas cell exhibit one weakness. The measured intensity and curvature change, when the pressure state in the cell changes. To smooth this change of pressure, the filling time of the gas cell has been reduced during this experiment by adjusting a valve. Both the measured curvature and intensity are shown in figure 4.1.

First, to test the sensitivity of the system to pressure changes, several pressure cycles consisting of a change from air to vacuum and back have been performed. As shown in figure 4.1, the reflected intensity changes from 3.63V, when the cell is filled with air to 3.76V, when the cell is evacuated. The curvature signal shows peaks, when the pressure inside the cell changes and the measured curvature changes slightly depending on the pressure inside the cell.

After 30min, the sample is exposed to a pressurized (1900 mbar) hydrogen-argon mixture. The reflectivity of the sample decreases immediately and reaches a minimum of 2.2V after 7 more minutes. The curvature of the sample is affected as well, the measured radius of the sample changes to 43% of its original value.

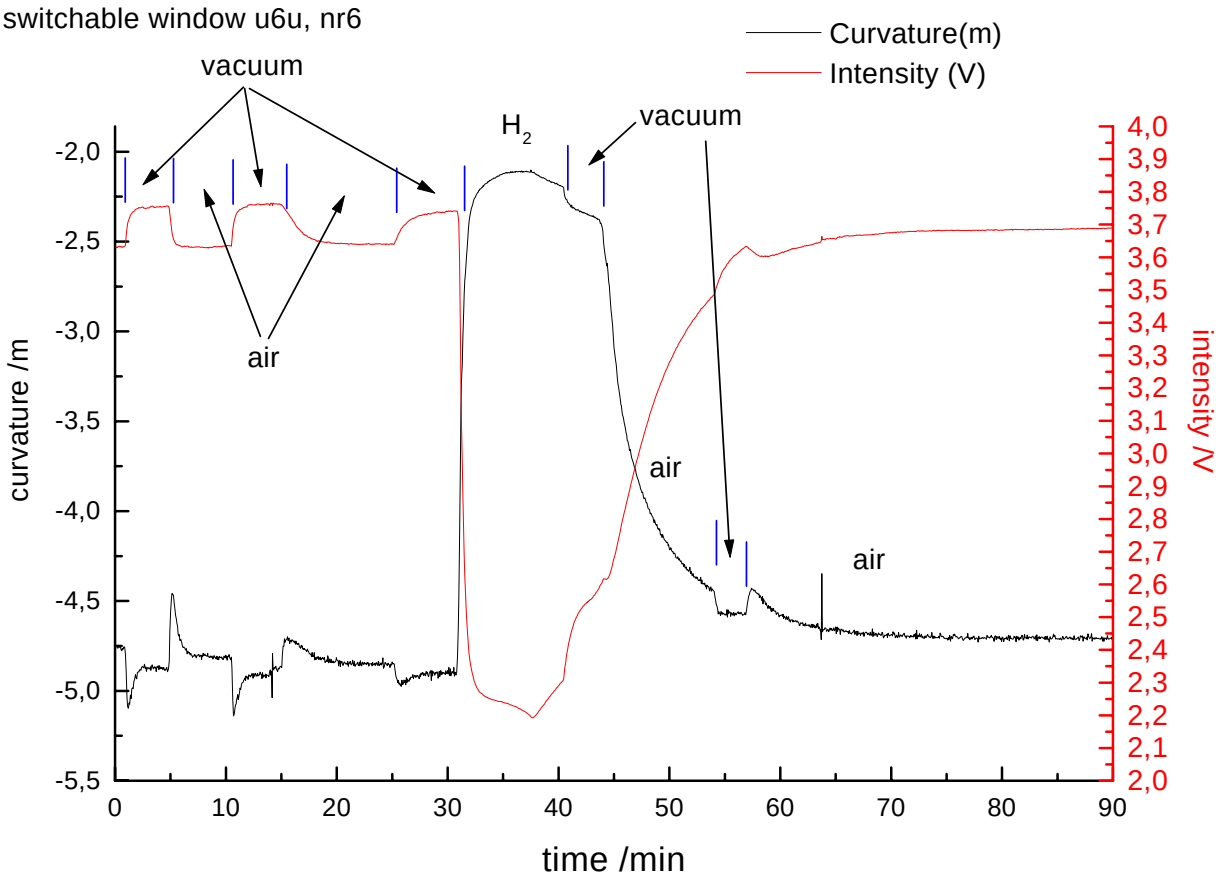

Figure 4.1: A switchable glass in the gas cell.

After 37min, the valve connecting the gas cell with the gas bottle is closed and due to a leak in the gas cell, the pressure inside the cell starts to decrease. Both the reflected intensity and the measured curvature change because of the pressure change.

After 41min, the cell is evacuated, both the intensity and curvature change because of the decreasing pressure. Still, the measured values of the intensity and the curvature do not get close to the values measured prior to the exposure to hydrogen.

Then, after 44min, the cell is flooded with air. The curvature and the intensity change dramatically. After 70min, both the intensity and the curvature are close to their original values.

This experiment shows that the change in reflectivity of the switchable windows can be monitored in the system to determine the state of the window. It also shows, that the curvature of the coated glass changes dramatically during switching. This leads to the conclusion that the thin film is stressed during the switching process and that this stress can be measured using this setup.

It is not yet possible to do any quantitative analysis. To do so, the curvature changes have to be separated into the component caused by the pressure change in the cell and into the component caused by the switching of the coating.

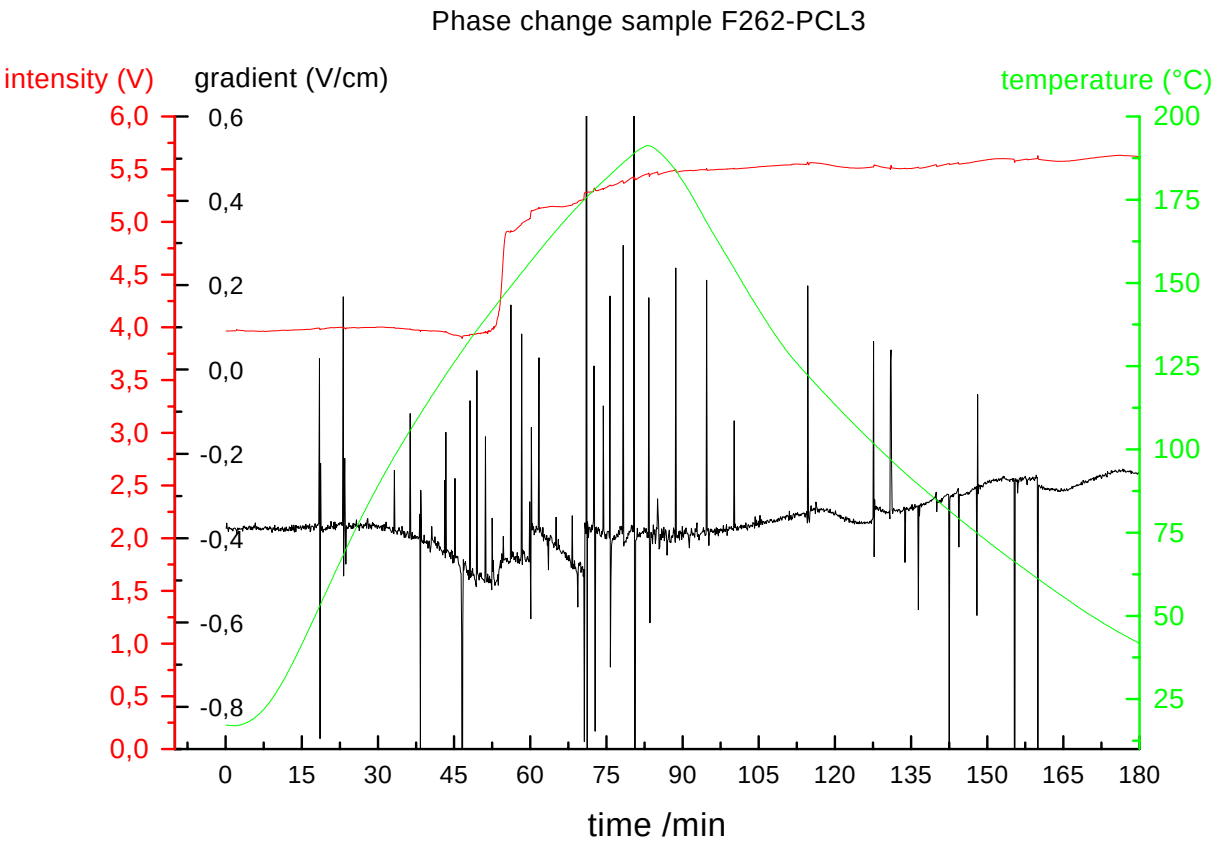

Figure 4.2: A phase change sample is annealed in the oven.

4.2 A measurement using the oven

To test, whether the phase transition of the phase change samples can be determined using the annealing unit, a phase change sample has been annealed in the vacuum chamber.

The sample consists of a silicon substrate (500µm) coated with a thin phase change material film (100nm). The measured reflected intensity and the gradient are displayed in figure 4.2. The temperature is also plotted in the same graph.

The sample is annealed at a rate of 2.5°C per minute from room temperature up to 190°C. During the first 54min, the intensity remains almost constant. The measured gradient shows many peaks and a decrease that can only be explained by the problems mentioned in section 3.7.

After 55min, the temperature level has reached about 150°C and the intensity signal shows a sudden increase from 3.92V to 4.92V. The gradient shows no change at the same temperature.

The intensity continues to increase slightly, with time the gradient increases, too.

This experiment shows that the change in reflectivity of the phase change sample can be monitored in the oven. However, due to the noise and the problems mentioned

in section 3.7, a change in the curvature of the sample could not be monitored during this experiment. This leads to the conclusion that the change of curvature caused by stresses in the thin film is low using this sample and can only be monitored after the system has been improved further. Using a thinner substrate would also help to enable measurements of the changing stress in the film.

Conclusions and suggestions for future work

A system to measure stress in thin films has been presented and characterized in this thesis.

The stresses are determined by measuring the curvature of the samples. A laser scans over the sample and the reflection of the beam is analyzed to determine the curvature of the sample. Additionally, the reflectivity of the sample is measured as well.

The system is equipped with two sample holders allowing further analysis. An annealing unit allows thermal treatment of samples. It is possible to anneal samples up to 500°C in a vacuum of less than 10^{-6}mbar. This allows in situ analysis of the stress and reflectivity of thin metal films and phase change media during annealing.

Samples can be exposed to pressurized gases using a gas cell. The gas cell can be filled with air, with a pressurized argon hydrogen mixture (up to 4bar) or it can be evacuated (less than 10mbar). This enables in situ analysis of the stress and reflectivity of switchable windows during exposure to hydrogen.

The system has been characterized. First, the noise of the measured position and intensity of a laser spot on the detector have been determined. The noise level depends on the setup. When the laser is pointed directly towards the detector, the noise level is very low and can reach the specifications of the detector. The noise level of the normal measurement setup is much higher.

The increase of the noise level is related to the scanning mirror. The mirror adds frequencies of 50Hz and 100Hz to the spectrum of the noise. This is presumably caused by vibrations of the scanner due to the net frequency of 50Hz. A noise measurement using the evacuated annealing unit shows a significant increase in noise. This increase is related to vibrations of the mechanical pump.

A long term measurement shows that the noise of a real measurement is as low as 0.07%, it also shows that the system is very sensitive to vibrations.

Another experiment shows that reflections of low intensity can have a tremendous influence on measurements and need to be removed.

The gas cell and the annealing unit have been characterized as well. When the pressure state of the gas cell changes during a measurement, the measured intensity and resulting curvature show unexpected changes. The same behaviour is visible in

the annealing unit, when the sample is heated.

This behaviour is related to the fact that the sample moves in both cases. In the gas cell, this sample movement is caused by the pressure shock. In the annealing unit, the sample is moved due to a movement or deformation of the annealing unit.

This is a fundamental problem, the movement of the reflected beam causes a change in the measured curvature and the reflectivity. This is presumably related to an inhomogeneously working detector or to a misaligned system.

Apart from this fundamental problem, the noise of the system should be reduced further.

The position noise is limiting the measurable curvature by affecting the accuracy of the linear regression determining the curvature. The noise level can be lowered by filtering out the disturbing frequencies. It is also possible to decrease it further by averaging over more data points. The noise level of the annealing unit has been lowered significantly by fixing the tube of the mechanical pump to a block of concrete which reflects the vibrations back to the pump.

To keep the noise at a low level during long term measurements, it is essential to prevent vibrations. This can be done by improving the optical table e.g. by attaching air cushions underneath each leg or by using a different optical table. A separate room for the experiment would also help to reduce vibrations. To reduce noise during measurements, the air flow has to be reduced by covering the setup with a box.

The quality of the samples has to be improved as well. For reproducible measurements allowing quantitative analysis, better substrates are necessary.

Although the system exhibits problems, measurements have been carried out to test, whether the samples show a measurable response, when they are annealed or exposed to hydrogen. These measurements are very promising. It was possible to monitor a phase transition of a sample in the annealing unit as well as a switching of a switchable glass in the gas cell. This leads to the conclusion, that it is in principal possible to perform such measurements using this system, but there are still a lot of major and minor improvements to be implemented, before quantitative relevant measurements are possible.

Part II

Room temperature recrystallization studies and X-ray texture analysis of electroplated copper in damascene structures

Introduction

The following part summarizes the experiments, which have been carried out at Bell-Labs, Lucent Technologies, Murray Hill, New Jersey. The primary goal of this work has been to characterize electroplated copper in damascene trenches.
Two types of measurements have been made on copper:

- First, the crystallographic orientation of the copper inside the damascene trenches has been investigated by complete X-ray texture analysis of copper by measuring the pole figures for the (111), (200) and (220) copper peaks. This has been done both with PVD deposited and electroplated copper on two different types of X-ray diffractometers, a conventional one (built by the company Scintag) and a new diffractometer with area detector (built by the company Bruker-AXS).

- Second, the room temperature recrystallization of electroplated copper has been analyzed. This has been achieved by monitoring the recrystallization process directly in a Focused Ion Beam microscope (FIB).

Nowadays, there is an enormous interest in copper as a substitute for aluminum as an interconnect material in advanced computer chips. The properties of these interconnects are crucial for the speed of the chips because their resistivity is one of the factors limiting the performance due to the RC delay.

Copper was chosen as the new material for interconnects because of its better conductivity and better electromigration resistance and lower costs due to a different processing technique. While the aluminum interconnects are sputtered as a thin film and then patterned by etching, the copper interconnects are formed by electroplating in trenches etched in an insulating layer.

The aim of this work is to characterize and understand the properties of the electroplated copper in these trenches.

Chapter 5

Experimental

This chapter describes the experimental issues of the measurements.

First, in section 5.1, the samples and the sample preparation are discussed and a summary of the different samples used for the X-ray texture analysis and the recrystallization studies are given.

In section 5.2, the measurement techniques used for the characterization of the electroplated copper are described.

The recrystallization process has been monitored in a focused ion beam microscope, the images taken in this machine have been analyzed manually (section 5.2.1). The X-ray texture has been investigated using both a standard X-ray machine and one consisting of a setup with an area detector. The setup of both systems are described and the differences between them concerning the complete pole figure texture analysis are discussed (section 5.2.2).

5.1 Samples and sample preparation

All of the experiments were carried out on samples prepared the same way. The preparation process is described briefly and illustrated in figure 5.1.

The first step is to etch trenches in an insulating SiO_2 layer by normal lithographic methods. In these trenches, three layers of material are deposited. The first layer is a barrier material, which is used in the interconnects to prevent the copper from diffusing into the insulator. Here, it is either 500Å of Ta or TaN (as measured on the surface between the trenches), which is put down by sputtering. The next layer is a 1000Å thick layer of sputtered copper. Its main purpose is to serve as the cathode in the following electroplating step. About 1µm of electroplated copper is then electroplated onto the sample.

As shown in figure 5.1, not only are the trenches filled, but the whole sample is covered with copper. These samples are used for the recrystallization experiments. For the X-ray texture measurements, the samples undergo another preparation step, the chemical mechanical polishing (CMP) to remove the copper above the trenches

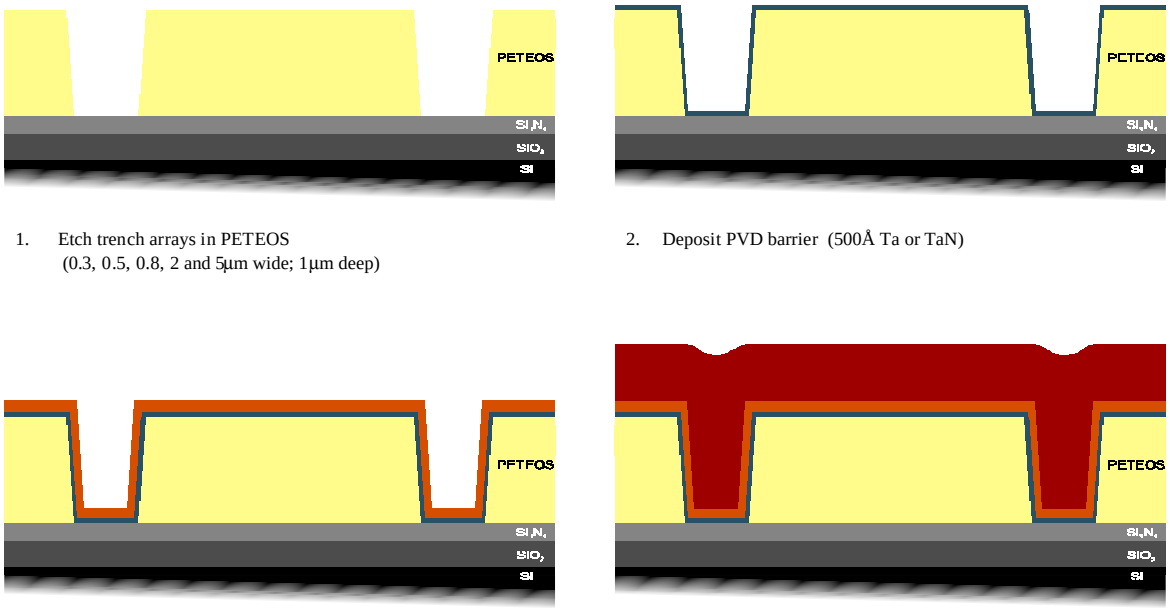

Figure 5.1: Sample preparation and setup

(figure 5.2).

CMP involves the removal of material by abrasion through chemical reactions using an elastomeric polishing pad and slurry. This allows us to examine the X-ray texture of only the copper inside the trenches.

Since modern computer chips have up to six metallization levels, the size of the interconnects on the chip varies depending on the purpose and level of its implementation. The interconnects serving as the power lines are up to 5µm wide, while interconnects at the lowest level connecting the transistors may have a width of less than 0.2µm. To take this into account, the geometry of the trenches is varied. There are 9 different trench geometries on a wafer consisting of 5mm×5mm arrays of trench/space gratings shown in the table below.

The areas are separated on the wafer by blank areas without trenches and can be cleaved out of the wafer individually. On any given wafer the depth of the trenches is the same, but two sets of wafers have been produced, with either 0.5µm or with 1.0µm deep trenches.

Trench width:	Trench spacing:
0.3µm,	0.3µm
0.3µm,	3.0µm
0.5µm,	0.5µm
0.5µm,	3.0µm
0.8µm,	0.8µm
0.8µm,	3.0µm

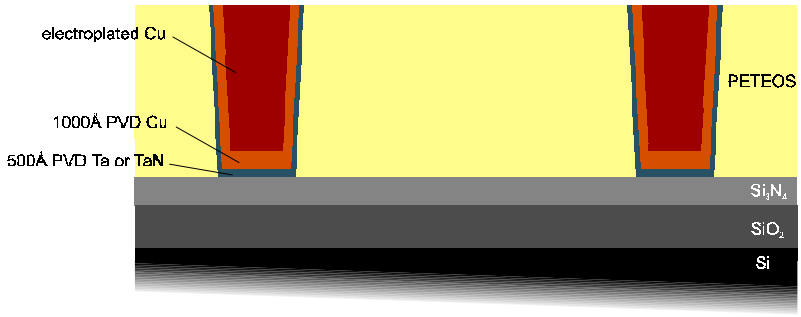

Figure 5.2: The overlaying copper is removed by chemical mechanical polishing (CMP) to prepare samples for X-ray measurements.

2.0µm,	2.0µm
5.0µm,	5.0µm

blank, no trenches but the same stack of materials

To help analyze the copper seed layer texture, some samples have a thicker PVD copper layer of 3000Å and no additional copper is electroplated onto the sample. These samples were not treated with CMP prior to the X-ray measurements. Measurements concerning these samples are discussed in section 6.1.1, all other experiments have been carried out using samples with electroplated copper.

5.2 Measurement techniques used

5.2.1 Focused Ion Beam (FIB)

The Focused Ion Beam microscope (FIB) is similar to the Scanning Electron Microscope (SEM) except for the fact that the electron beam is substituted by a beam of gallium ions. When the ion beam is scanned over the sample, secondary electrons generated by collisions of the ions with the sample are detected and imaged on a screen.

The purpose of the FIB imaging has been to look at the grain size of the electroplated copper. It is possible to see the grain size of the copper, because grains with different crystallographic orientation have different ion channeling properties. The deeper the ions channel into a grain, the darker is the image of the grain, because fewer secondary electrons reach the detector.

If a sample is highly textured, grains may give similar intensities making it hard to distinguish grain boundaries. In such a case tilting the sample helps increasing the contrast.

Additionally, there is an amorphous oxide layer on top of the copper that must be removed first. This is done in the FIB by scanning the Ga^+ beam, which sputters material away.

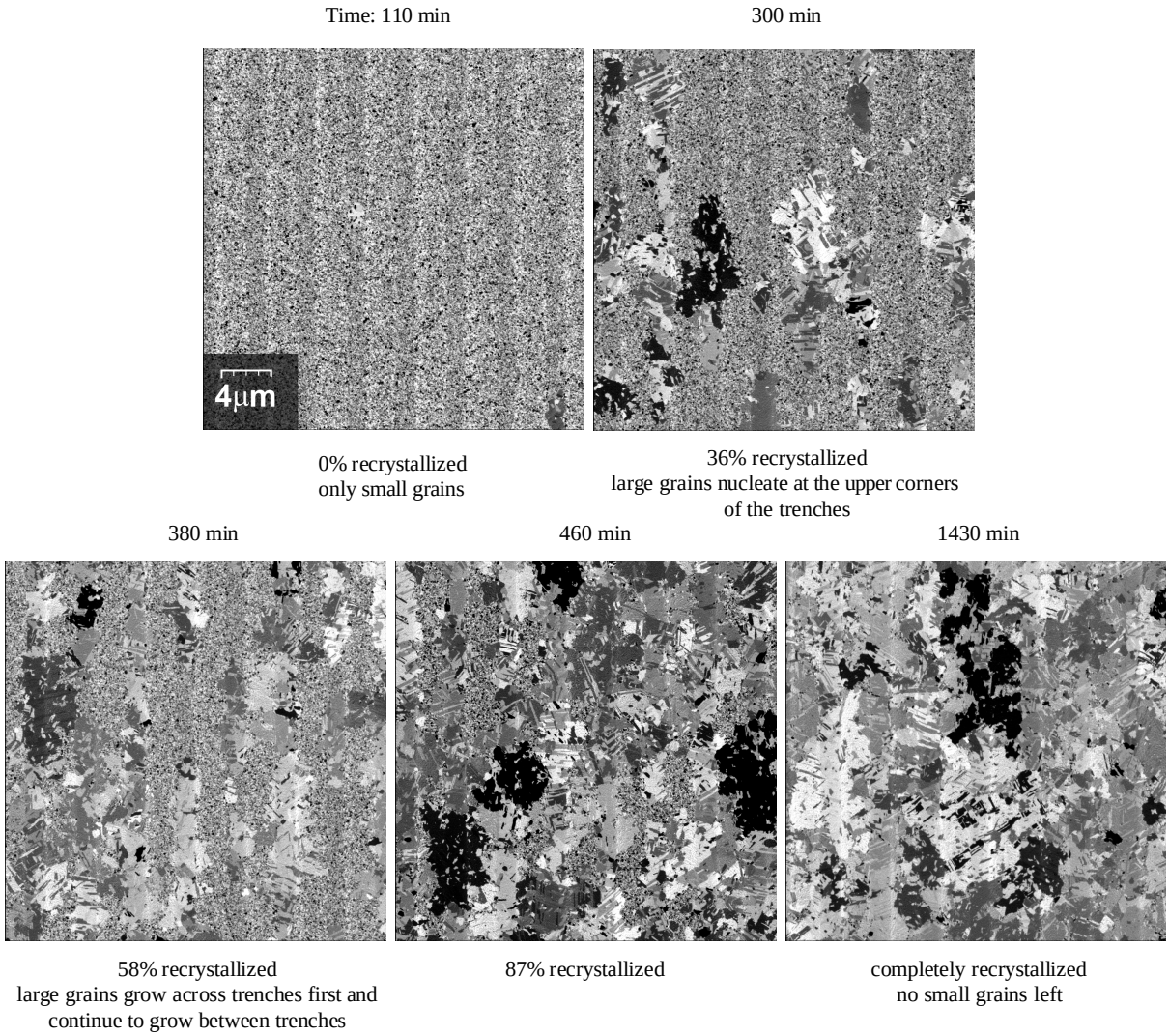

Figure 5.3: Series of FIB pictures showing the recrystallization process. The barrier material is Ta, the trenches are 1µm deep, 2.0µm wide and separated by 2.0µm. The recrystallization starts presumably inside the trenches and proceeds across the trenches first [26].

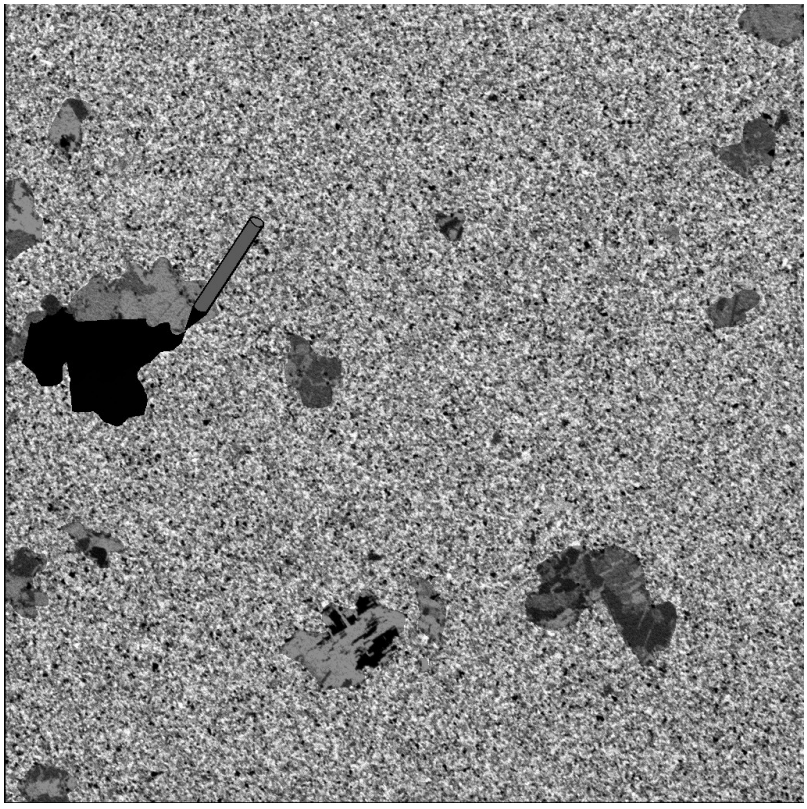

Figure 5.4: Analyzing a picture is done by painting the grown grains.

Immediately after the samples are electroplated, the copper is small grained. At room temperature after some hours or days, the grains grow by secondary recrystallization or abnormal grain growth. Here, it will simply be called recrystallization. To measure the kinetics of the recrystallization, it is necessary to take images of the transforming copper. Since the gallium incorporation into the copper in the imaged area affects the recrystallization kinetics, a new area is imaged each time. The samples with just PVD copper on top do not recrystallize although they are also small grained.

In these experiments, images are recorded every few hours. The images have a dimension of 30µm by 30µm, the small grains of the freshly plated copper are about 0.1µm in size, while the recrystallized grains are about 1-10µm large.

A typical data set consists of approximately 6 pictures between 0% and 100% recrystallization (see figure 5.3). To measure the fraction of recrystallized area in an image, the large grained area of the picture is manually painted in one colour (figure 5.4) using a commercially available image processing program (Adobe Photoshop). Looking at the histogram, it is possible to quantify the amount one colour occupies which equals the percentage of recrystallization.

Over all, 464 pictures have been analyzed out of more than twice that amount of images taken.

The process of recrystallization can be modeled by a general form of the Avrami-

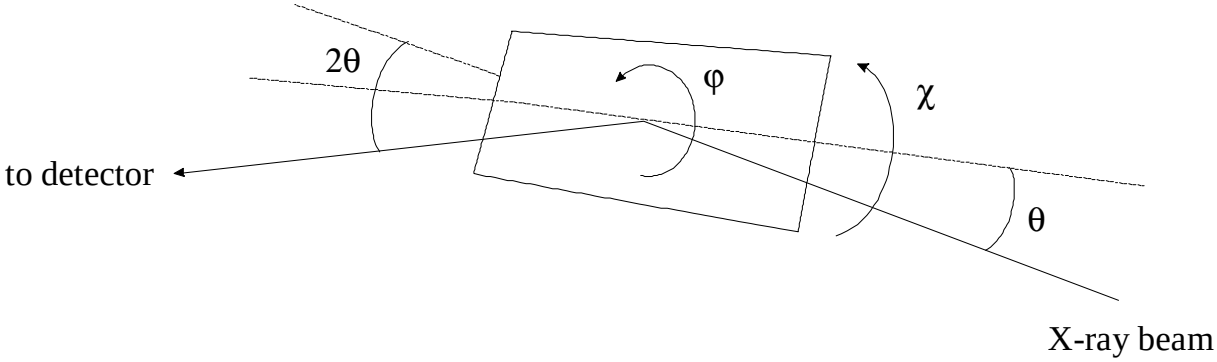

Figure 5.5: Conventional X-ray setup to measure textures.

Johnson-Mehl equation. The factor of recrystallization expressed in percentage is given by:

$$f = 100 \cdot \left(1 - e^{-(\frac{t}{t_r})^{\alpha}}\right). \tag{5.1}$$

The parameter t_r gives the time at which about 63% of the material is recrystallized. The value of α is related to the steepness of the curves. To fit the data in a fast and easy way, a small program has been written, which fits the data with the Avrami-Johnson-Mehl formula using a 'simulated annealing' algorithm.

5.2.2 X-ray texture analysis

X-ray diffractometer with conventional detector

After the overlaying copper film on top of the samples has been removed, it is possible to measure the X-ray texture of the copper inside the trenches and display it as pole figures. To determine the relative distribution of one orientation it is necessary to measure all possible orientations of the planes belonging to it. To achieve this, the Θ and 2Θ angles (see figure 5.5) are set to match the Bragg condition,

$$\lambda = 2nd \sin\Theta,$$

for the selected planes (see e.g. [22]). The diffractometer uses a copper tube with $\lambda_{Cu} = 1.54\text{Å}$. The (111) planes of copper are detected at $2\Theta = 43.4^\circ$, the (200) planes are at $2\Theta = 50.5^\circ$ and the (220) planes can be found at $2\Theta = 74.0^\circ$. When 2Θ is set to match the Bragg condition, only X-rays diffracted by the correct planes will be seen by the detector no matter how the sample is moved. To scan over all planes in the sample, it is rotated (φ) and tilted (χ) as illustrated in figure 5.5.

However, it is not possible to see all the planes. Especially planes perpendicular to the surface cannot be measured directly using this setup, because it would be necessary to tilt the sample up to 90° to see them.

The size of the beam on the sample increases upon decreasing incidence angle. The spot size must be smaller than the sample size and the requirements on mounting the sample increase as well as the flatness of the sample becomes more and more crucial at low angles ($\leq 5^\circ$). Another aspect of measuring at such a grazing incident angle is that the measurement is surface sensitive. Because of these effects, the measurements are restricted up to $\chi = 80^\circ$.

The data have also to be corrected for noise. The easiest way to measure the noise at the three poles is to make a $\Theta/2\Theta$ scan and to observe the background around the peaks.

The pole figures measured here have a coverage of $0^\circ \rightarrow 80^\circ$ in χ and of $0^\circ \rightarrow 360^\circ$ in φ (full circle) with a step size of 5° each. The data are plotted in an azimuthal equidistant projection, which means that χ is plotted linearly from the inside to the outside of the pole figure and φ is represented along the perimeter. The missing data between the 5° grid are interpolated linearly. The y-direction in the pole figure is perpendicular to the trench direction, the x-direction is parallel to the trenches. A sample pole figure is shown in figure 5.6.

The count rate of each data point on the pole figure is represented by a logarithmic colour map. It is possible to plot the absolute counts of each data point, but it makes more sense to plot relative values, multiples of the average, to make the data more comparable between different samples. When the data is displayed this way, the average value on the pole figure is 1 and a data value of 2 means twice the intensity of the average across the pole figure. At this point it is important to remember that the data in the outer 10° of the pole figure are unknown and cannot be taken into account.

Such a pole figure is called an incomplete pole figure due to the missing outer ring. It is possible to generate complete pole figures without missing parts, but only by making calculations with the help of a computer. The program used here to calculate the complete pole figures is called 'POPLA' (Preferred Orientation Program from Los Alamos). It takes (in the case of a cubic material) three incomplete pole figures to calculate the complete pole figures by a harmonic analysis. The complete pole figures can be plotted like the incomplete pole figures. It is important to compare the incomplete and complete pole figures to verify the calculations performed by the program.

One full measurement of the three pole figures and a $\Theta/2\Theta$ scan to determine the noise takes about 15 hours.

X-ray diffractometer with area detector

Modern X-ray diffraction techniques make use of an area detector to speed up the texture measurement significantly.

Such a machine has been set up during my stay at Bell Labs. It was build at Bruker AXS in Madison, Wisconsin. The area detector is an ionization chamber and can detect X-ray photons in an array of 1024 by 1024 wires. Visible on the area detector are the rings caused by the diffraction of the X-ray beam on the matching planes. The detector covers an angular range of about 40° in 2Θ at a distance of 6 cm. It is therefore possible

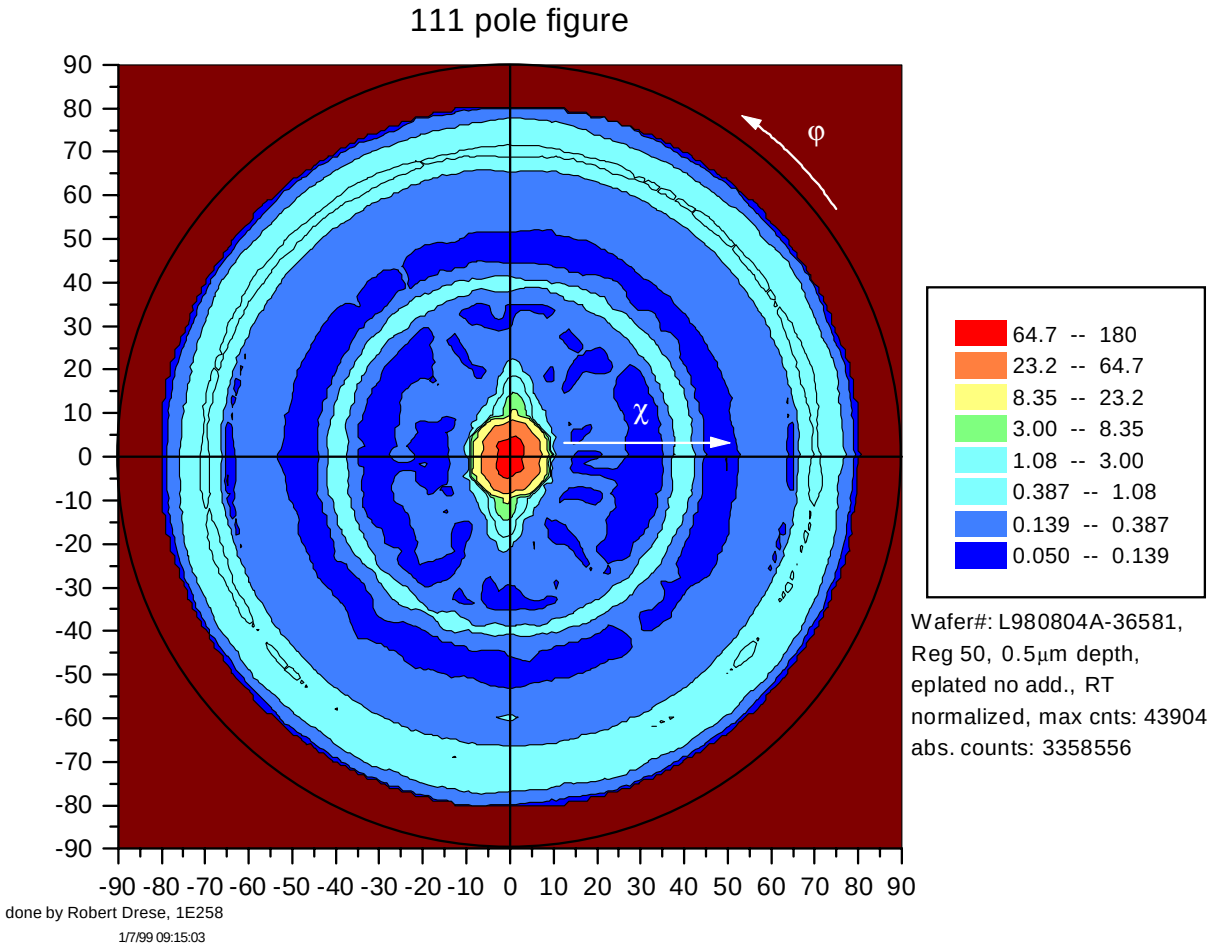

Figure 5.6: An incomplete (111) pole figure with a strong central peak, which causes also the ring at $\chi = 70.5°$. The other ring at $\chi = 38.9°$ results from a (511) texture caused by twinning of the (111) oriented grains.

to look at different peaks simultaneously. In this case it was possible to see all the three copper peaks of interest simultaneously.

The geometry of such a system is mainly the same as in a normal X-ray system (see figure 5.7). However, since χ is restricted to only two positions ($\chi = 90°$ and $\chi = 54.74°$) on this machine, it is not possible to use the method described above to do conventional pole figure measurements.

This is compensated for by the area detector on which the rings of the diffracted X-ray beam are visible. Each ring on the detector is a cut through the pole figure belonging to the pole of the ring. The cut is not a straight line in the pole figure because the angular change along the ring is not only in χ but also in φ.

It is not possible to see the same points on a pole figure for different peaks at the same time, because horizontal movement on the detector is not only in 2Θ, but has also a component in χ. To utilize this, 2Θ is often not twice the angle of Θ, therefore Θ is

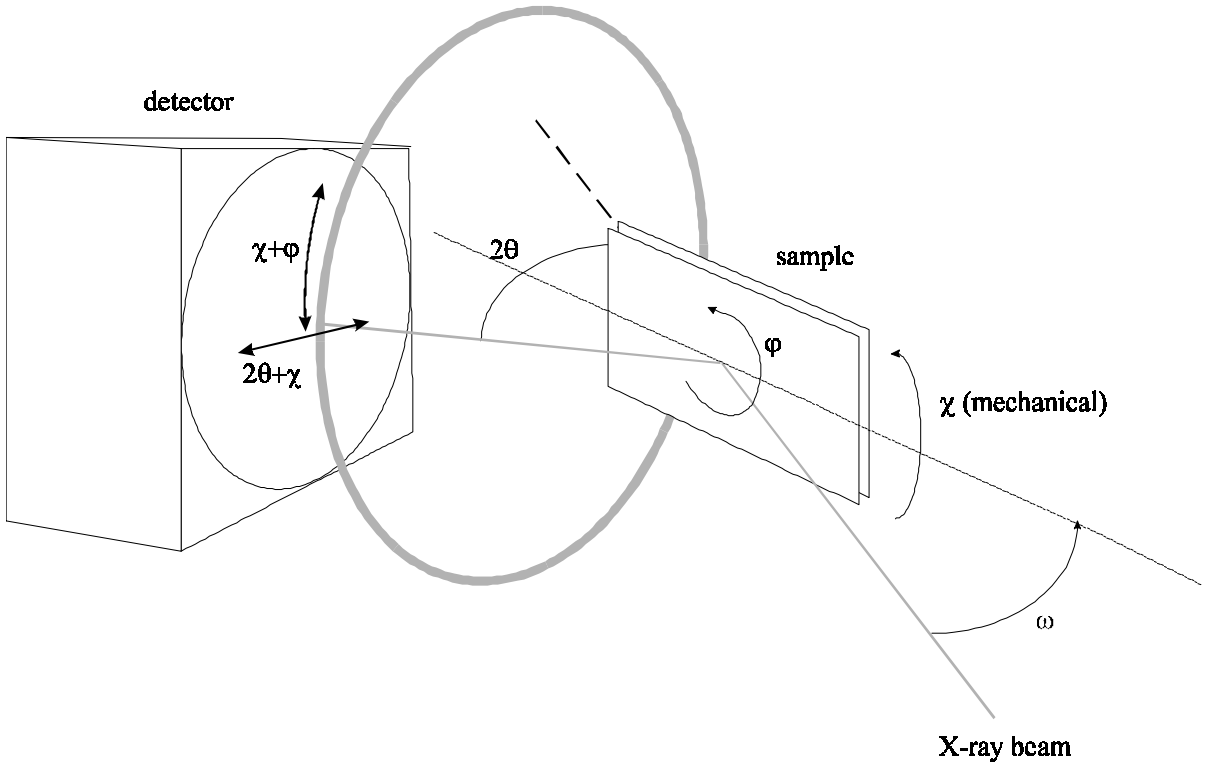

Figure 5.7: Geometry in an area detector system

renamed to ω in the ensuing discussion.

The computer program delivered with the machine takes care of the transformation from the measurements to the pole figure. It is also possible by simulation to determine in advance which parts of a pole figure can be covered by a measurement to optimize the measurement process.

For geometrical reasons, the images taken with the area detector have to be corrected. The detector is for instance flat and not bent along the perimeter of the goniometer circle. The images are also corrected for differences in count rate across the detector.

To collect as much of a pole figure as possible, it is necessary to do at least two measurements. The first one covers the center of the pole figure, the second one the outer area (figure 5.8).

To see the central peak of the pole figure, it is necessary to tilt the stage to $\chi = 90°$ and to move Θ and 2Θ to the Bragg condition of the peak observed. The measurement is done by rotating φ in discrete steps of 5°. Such a measurement covers, for the copper (111) peak, only the inner 30° of the pole figure.

To get the outer part of the pole figure, the stage is tilted to $\chi = 54.74°$, which is the second possible position for the goniometer. ω should be moved to an angle far off the normal position, e.g. to 5°, while 2Θ stays the same. The pole figure is recorded at an extreme position of a rocking scan, which (since a movement in ω is the same as a

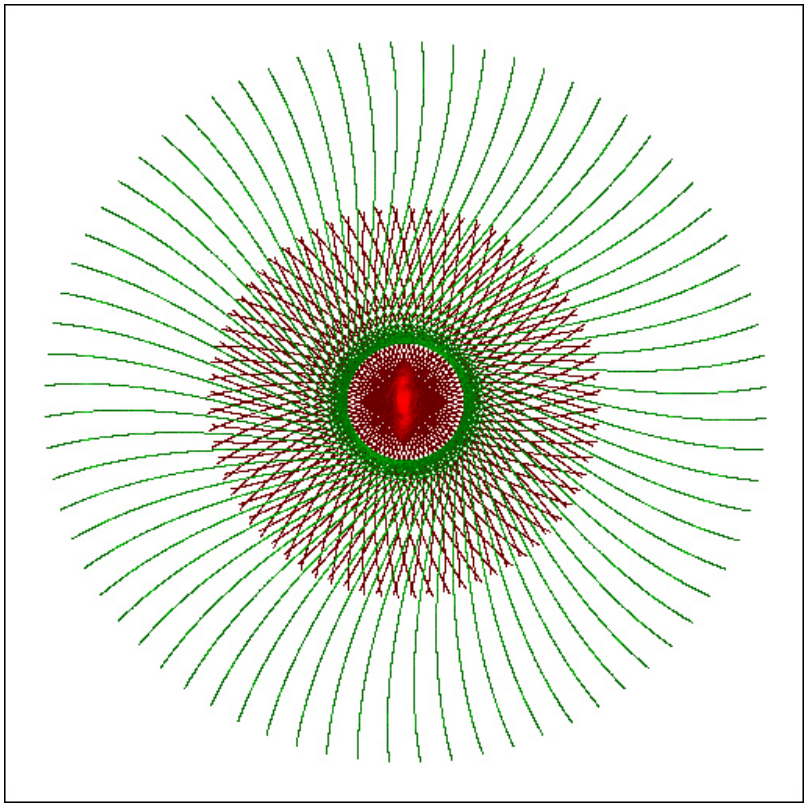

Figure 5.8: Illustration to show how two measurements overlap on a pole figure. Each line represents one picture taken in the detector at a given φ. The inner (red) measurement has been done at $\chi = 90°$, the outer one (green) at $\chi = 54.74°$.

movement in χ and φ) helps to cover a bigger area of the pole figure. A measurement setup like this will give a coverage for the (111) peak in χ of $25° \rightarrow 80°$.

Peaks at higher angles cause a problem, because their diffraction rings are bigger than rings at smaller angles. The percentage of the ring that can be covered by the detector is smaller and χ on the pole figure is restricted by this. The coverage of the pole figure of the (220) copper peak is therefore small, about $35° \rightarrow 65°$. Since the inner pole figure is also smaller than in the (111) case, it is necessary to do a third, intermediate, measurement to get an overlap between the inner and the outer parts of the pole figure for the (220) peak.

The small coverage is a problem for the software calculating the complete pole figures. The algorithms of the software work the better, the more data is provided. If the pole figures are small, the calculation may give wrong results. It is impossible to say exactly how much coverage is needed for accurate calculations, it depends on the complexity of the grain orientation distribution. It is therefore essential to compare the calculations with the measurements.

Some measurements have been performed in both machines with samples containing planes perpendicular to the surface. Both complete pole figures calculated show

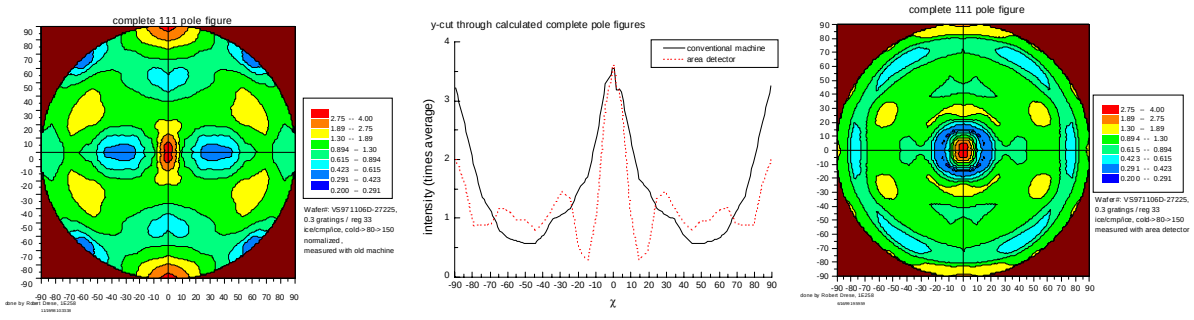

Figure 5.9: Comparison of calculated complete pole figures of the same sample taken on the conventional (left) and the new machine with area detector (right).

the same features (see figure 5.9). This indicates that the calculation of the complete pole figures was correct in this case.

Another problem we faced with the data of the new machine has been the merging of the two sets of data taken for one pole figure. The first few attempts to merge the partial pole figures of the two measurements showed a step between the inner and the outer parts of the pole figure. This is caused by the different values of ω, 2Θ and χ in each measurement, which causes the overall intensity to be different. To merge the pole figures properly, one part has to be scaled relatively to the other to prevent the step. When scaling the data sets, it is important to remember that the intensity of each data point in the pole figures can be very low and that the data is saved as counts in integer values. This means that the dynamic range of the data can be very low and the data must be scaled as floating point values to prevent a loss of information. It is also important to be careful in deciding which one of the two measurements has the correct intensity, because when the data gets imported into POPLA to calculate complete pole figures, the relative intensities of the three pole figures have to match. For the same reason, it is also necessary to scale and process all three pole figures in exactly the same way.

To merge the partial pole figures properly, a program has been written. The data is converted to floating point data and the data of each measurement is compared in the overlap region and scaled accordingly. The inner set of data is used as the reference measurement and not scaled, because this measurement is done at the same $\Theta/2\Theta$ angles as the measurements in the old machine. Another program written mainly by Kenneth Evans-Lutterodt, was used afterwards to convert the data from the original bitmap style file format in Cartesian coordinates to a file format in polar coordinates with a resolution of 5° by 5°. It integrates over each 5° by 5° area on the bitmap to get as much information out of the original file as possible. The different data format is necessary to make the data accessible for POPLA.

When measuring a pole figure at a low incidence angle of e.g. $\Theta = 5°$, the sample must be mounted very well. If the sample is not aligned perfectly, the pole figure has a broken symmetry. When mounting the sample, it normally gets corrected for the

height and the x/y position on the stage. After some measurements we found out that the way we used to attach the sample to the sample holder, a sticky tape, could cause the sample to not longer be mounted flatly, but tilted just a little bit. A very elegant way of aligning the sample, to make sure it is mounted flatly, is to look at the reflected beam of the laser built in the machine. The laser is normally used to align the height of the sample. If the sample is not mounted flat, rotation of the sample will result in a circular movement of the reflected laser beam. It is very easy to follow the movement of the laser spot with a pen on a piece of paper attached to the detector. The next step is to adjust the sample holder in a way that the laser spot moves into the center of the drawn circle, which results in a very well aligned sample.

The result of all the procedures mentioned above is a very fast and easy way of measuring pole figures on the new machine. One measurement for all three poles with noise correction and all calculations takes less than 2.5h, which is a sixth of the time it took on the old machine. The data taken has a resolution of less than or equal to 5° in φ and less than 0.2° in χ, which is much more information compared to the old measurements with a resolution of 5° in both φ and χ.

Although this may sound like the new machine is much better than the old one, I think that for the purpose of generating complete pole figures of copper it is better to use the old machine. The reason for this are the problems described above with the low coverage of the pole figures at higher angles. Many calculated pole figures generated with data collected in the new machine looked all just the same. There was no big difference in the generated complete pole figures, although the incomplete pole figures showed varying features. This problem could be solved by putting a normal 'Euler Cradle' in the machine instead of the manual χ stage. With a stage, which allows a movement in χ, it would be possible to measure pole figures of the same size as in the old machine but at a much higher speed and with a better quality. Another improvement would be a software that is not limited to a resolution of $5^\circ \times 5^\circ$ to calculate complete pole figures.

At the moment, the new machine can still be used to generate very nice incomplete pole figures. They have a very high resolution and lots of features not visible on pole figures measured in the old machine. Besides, there are other kinds of measurements, which are very difficult to do without an area detector. For example to perform a phase analysis of a strangely textured material, it is necessary to scan both $\Theta/2\Theta$ and χ to see all the peaks. To do this on a conventional machine the only fast way would be to pulverize the sample and destroy it by doing this. With an area detector, it is easy to do such a measurement in a short time.

Chapter 6

Results

In this chapter, the different experiments that have been performed are described as well as the results of these experiments are presented.

The first section (6.1) covers the experiments that have been carried out to investigate the crystallographic texture of the copper. Section 6.1.1 focuses on the texture of sputtered copper while section 6.1.2 discusses the texture of electroplated copper.

The experiments characterizing the recrystallization process of the electroplated copper are shown in the second part (section 6.2) of this chapter. The room temperature recrystallization kinetics are studied thoroughly, several parameters thought to influence the room temperature recrystallization are varied and the results of these experiments are shown.

6.1 Crystallographic texture

6.1.1 PVD copper

To investigate the properties of the sputtered copper layer, some samples were not electroplated, but were instead covered with 3000Å of PVD copper. Since this copper does not recrystallize, only X-ray texture measurements have been carried out. The samples have not been treated with CMP, so copper in the regions between the trenches as well as in the trenches contributes to the pole figures.

It is especially interesting to see what influence the geometry of the sample has on the texture of the copper, since during the sputtering copper is deposited both on the bottom and the sidewall of the trenches. The sidewall surface of some samples (e.g. the ones with a trench width of 0.3µm, 0.3µm trench separation) is larger than the area parallel to the surface, because of the trench depth of 1µm. To see the influence of the sidewall, I measured several gratings with different geometries.

Two pole figures of samples with different gratings are plotted in figure 6.1. An additional parameter investigated was the influence of the barrier material, Ta and TaN, on the texture of the PVD copper. To compare the textures of the samples with different geometries and different barrier material, cuts of the pole figures are plotted

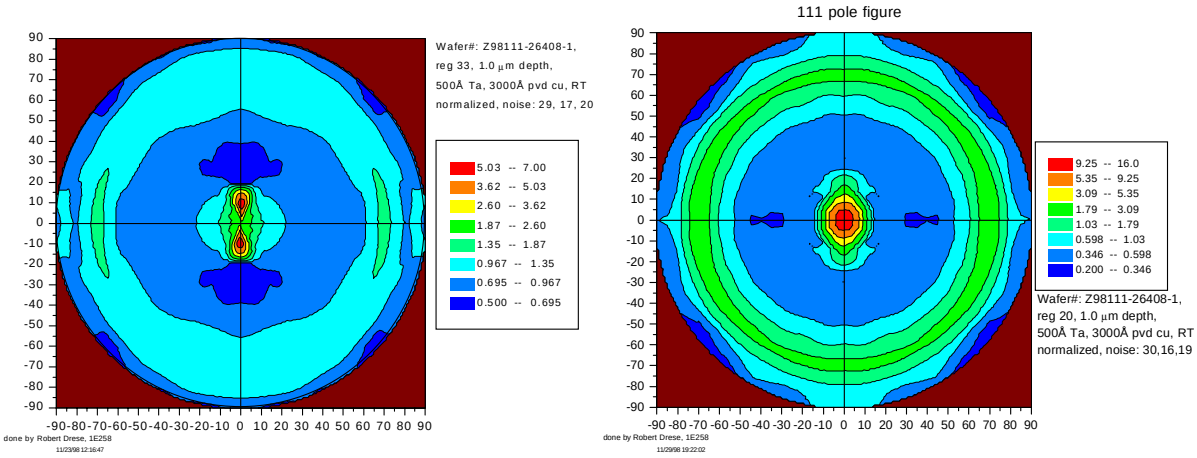

Figure 6.1: Comparison between the (111) texture of a sample with 0.3µm/0.3µm (left) and 2.0µm/2.0µm (right) geometry. The central peak of the left sample is split at about $\chi = \pm 10^\circ$, the wings on the left and right side are the intersections of the two rings at 70.5°. The right sample shows almost perfect circular symmetry.

in figure 6.2. The cuts are done across the trench direction (in y-direction). To look for the possible sidewall induced texture at $\chi = 90^\circ$, I chose to present the data from the generated complete pole figures.

The remarkable fact visible here is a split of the central peak in the samples with the smallest trenches. It looks like the central peak is divided into two single peaks at $\chi = \pm 10^\circ$ each. In the region 0.3µm/0.3µm trench width/spacing the two peaks are visible, while in the regions with wider trenches there is only a peak at $\chi = 0^\circ$.

There is also a small difference between the texture of the copper sputtered on Ta and on TaN. The split of the peak is surely related to the trenches, since it is not visible on any blanket samples. It might be that there are two textures competing against each other, a central peak at $\chi = 0^\circ$ and a peak around $\chi = 10^\circ$ for each sidewall. If the sidewalls are sloped and the growth direction is still predominantly parallel to the direction of the incoming sputtered copper beam, such a texture could develop.

It is not clear whether the split of the peaks is always the same. Since the measurement was done in 5° steps, the bad resolution in χ prohibits more details. A similar texture was found in previous experiments [25].

Another interesting result is the missing sidewall component at 90°. There is no (111) texture component pointing perpendicular to the sidewall. The amount of texture at 90° is even lower than average for most of the samples.

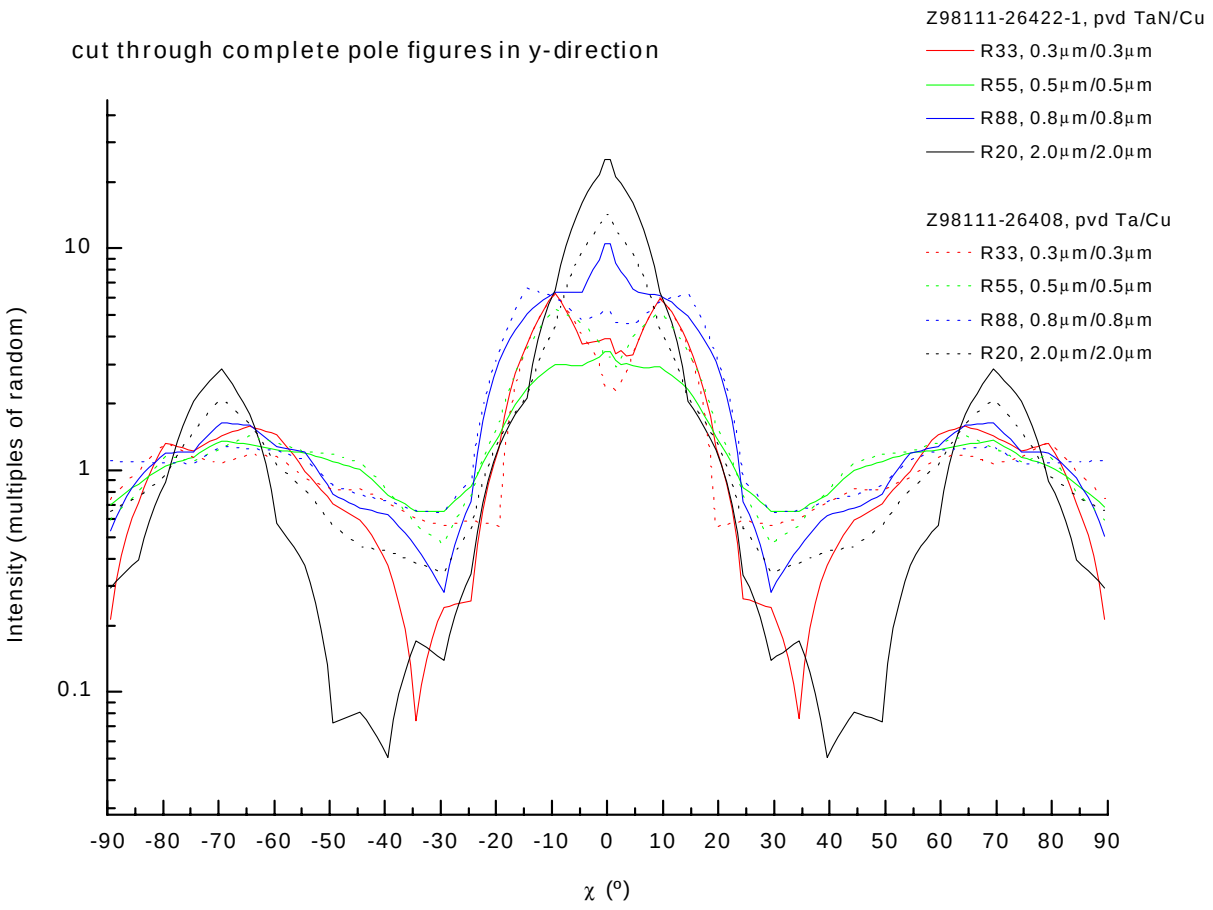

Figure 6.2: Cuts through complete (111) pole figures of PVD samples in y-direction.

6.1.2 Electroplated copper

Samples showing a sidewall texture

In contrast to the results of the PVD copper, where no (111) sidewall texture component was visible at 90°, the following samples show such a texture caused by (111) planes parallel to the sidewall of the trenches (see figure 6.3). During the electroplating process copper grows both on the bottom and the sidewall of the trenches with a strong (111) fiber texture. This type of texture was first observed on a small-grained sample stored on dry ice to prevent recrystallization and measured immediately upon warming to room temperature [28].

To investigate what happens to the texture after annealing to accelerate recrystallization, samples were annealed to various temperatures in forming gas (85% N_2, 15% H_2). The time the samples were annealed in the furnace was about the same for each sample, just the temperature varied. One sample was heated to 80°C, analyzed, heated to 150°C and analyzed again.

The best way to compare the textures is again by plotting cuts through the pole

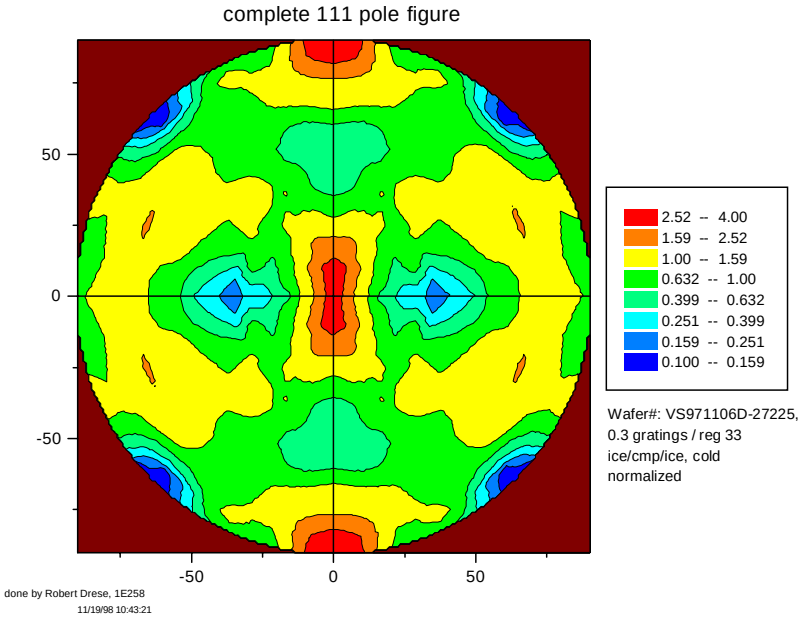

Figure 6.3: A sample, taken off the dry ice and measured immediately, with peaks visible at 90°. The planes causing these peaks are parallel to the sidewall of the trenches.

figures (figure 6.4). The cuts are done in the y-direction of the pole figures, which corresponds to a cut across the trench.

The sidewall texture is strongest in the sample that was taken off the dry ice and measured immediately. The maximum intensity of the sidewall texture is close to that of the central peak and reaches about 3.7mrd (multiples of random). There is also an indication of a split central peak, similar to the one observed in the PVD copper. The annealed samples show a weaker sidewall component. The higher the temperature of the annealing, the lower is the relative amount of (111) planes parallel to the sidewall. The samples annealed at 400°C have a sidewall component of less than 2.5mrd left, while the central peak stays about the same. Surprising is the fact that the sample that was annealed two times, first to 80°C and then to 150°C, shows after the second annealing step a much stronger sidewall texture than after the initial annealing to 80°C. Its sidewall texture is also much stronger than the sample annealed immediately to 150°C.

It is important to remember that the area of interest, the sidewall component of the texture, is not measured directly, but calculated by a software. On the other hand the data sets are all treated the same way and since the data is shown in relative counts, the amount of copper on the samples and the size of the samples should not matter at all and the measurements should be comparable.

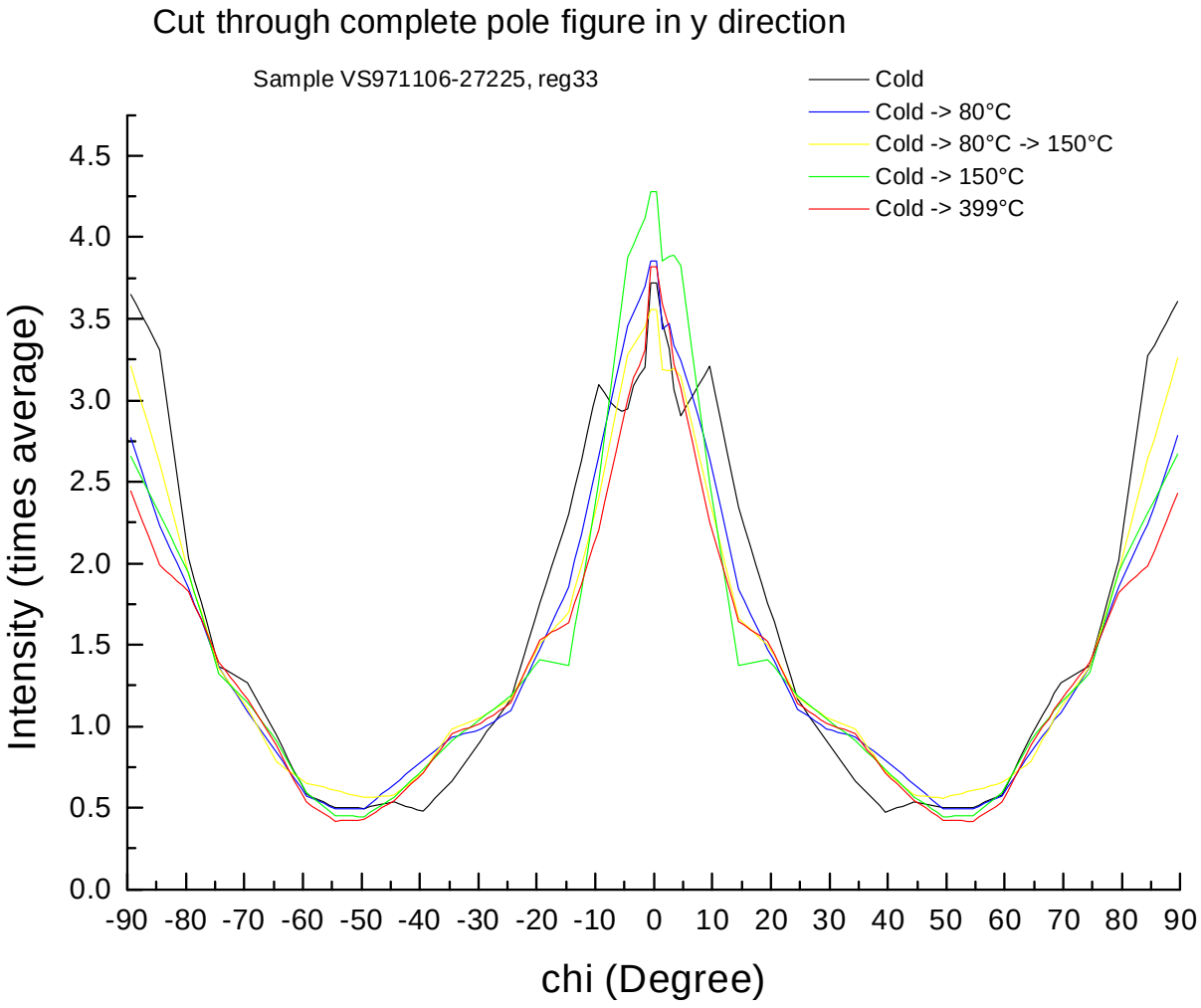

Figure 6.4: Cut through complete (111) pole figures of electroplated samples across the trench direction.

X-ray texture analysis of samples plated in an old and new plating bath

X-ray texture analysis was performed on samples plated in a new and old plating bath to look for differences. The same samples have been used for the recrystallization experiments in section 6.2, where they are described in detail.

Four measurements have been carried out, two samples were taken from the dry ice and measured immediately. Then, the same samples have been annealed at 400°C for 40 minutes and the texture has been remeasured.

The main difference in the texture of the small grained samples plated in the old and the new bath are the central peaks (figure 6.5). It is much higher in the case of the new bath and as a result, the ring at 70.5° is more distinct than the ring of the sample plated in the old bath. This causes also the lower average counts in the area between the central peak and the 70.5° ring for the sample plated in the new bath. The central

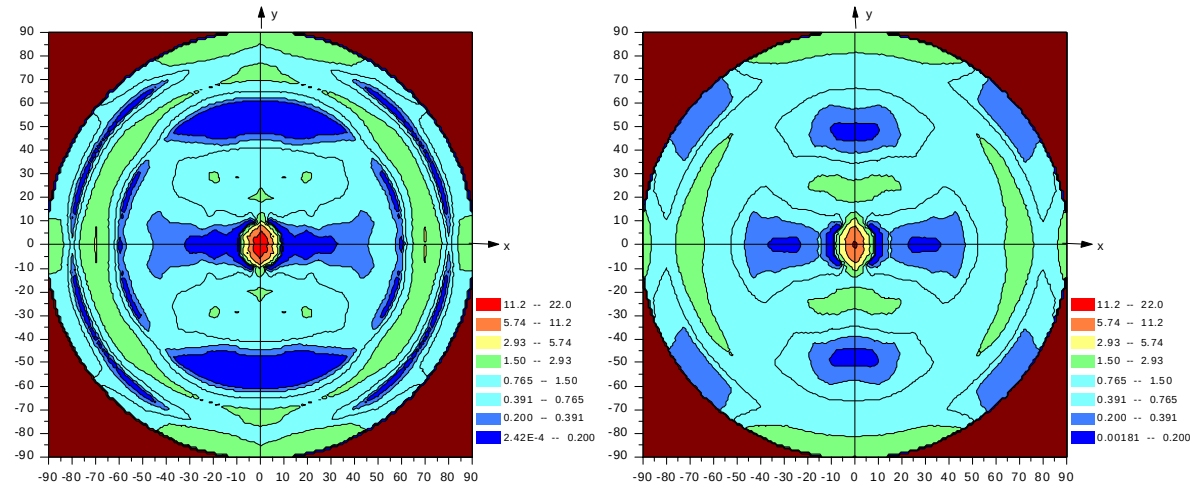

Figure 6.5: Complete (111) pole figures of cold samples plated in the new bath (left) and in the old bath (right). They are scaled to the same colour scheme to make them comparable.

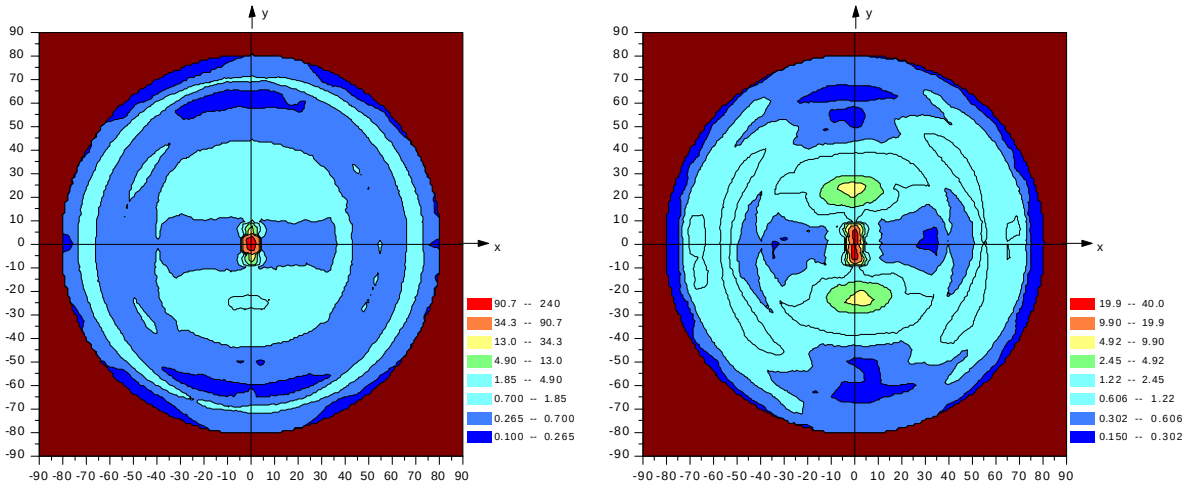

Figure 6.6: Incomplete (111) pole figures of the samples plated in the new bath (left) and in the old bath (right). The samples have been annealed to 400° for 40min.

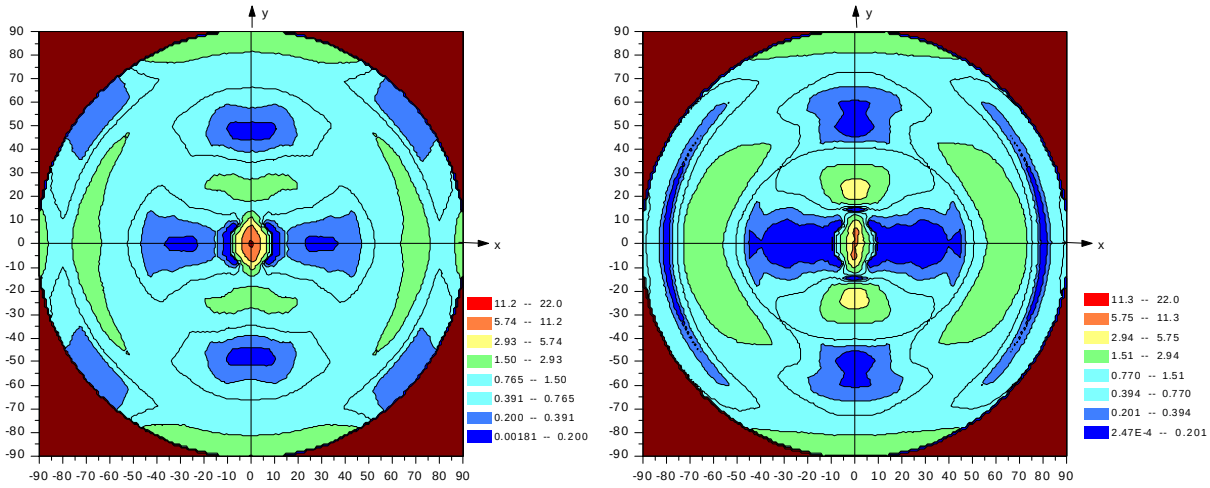

Figure 6.7: Complete (111) pole figures of the sample plated in the old bath. On the left its in the cold state, on the right side after annealing to 400°C for 40 min.

peak is clearly elongated across the trench in both cases, which explains the twofold symmetry at 70.5°.

In case of the sidewall texture, there is no significant difference visible. There is a small sidewall component visible, but it is much weaker than the sidewall component seen in the other samples above.

After annealing, the small differences in the strength of the (111) fiber texture are enhanced (figure 6.6). The central peak of the sample plated in the old bath is more elongated across the trench than the peak of the sample plated in the new bath, which explains the different shapes of the 70.5° ring. It shows again a twofold symmetry for the sample plated in the old bath and it is a continuous ring in the case of the sample plated in the new bath. Apart from these, there are no big differences in the structure of the pole figures visible.

A complete pole figure of the sample plated in the new bath could not be generated because of software limitations. The problem is that the software POPLA can only process samples with a maximum of less than 100 times the average.

To get a comparison of the complete pole figures before and after annealing, the texture of the sample plated in the old bath is shown in figure 6.7 both before and after annealing to 400°C.

The structure of the texture is mostly preserved, there are only a few differences. The two wings at 70.5° are broadened after annealing, which indicates that the texture component parallel to the surface is lowered. This suggests that there is no preferred grain orientation for the grain growth.

The age of the plating bath seems to have no influence on the texture of copper, although it has a large influence on the recrystallization kinetics as shown in section 6.2.

6.2 Recrystallization kinetics of electroplated copper

The main experiment during the stay at Bell Labs has been to observe the room temperature recrystallization of electroplated copper as a function of several parameters.

Four parameters, thought to influence the recrystallization kinetics, have been examined:

- Low temperature cycling. One set of samples was placed immediately on dry ice after plating to prevent recrystallization prior to measurement. The second set of samples was shipped to us at room temperature.
- The age of the plating solution. One set of samples was electroplated in a freshly prepared plating bath, the second set was plated in an old plating solution, in which already about 3000 wafers had already been processed.
- The geometry of the trenches, five different geometries have been examined (width of the trenches/spacing between trenches): 0.3µm/3.0µm, 0.5µm/3.0µm, 0.8µm/3.0µm, 2.0µm/2.0µm and 5.0µm/5.0µm.
- The barrier material, Ta or TaN.

6.2.1 Influence of low temperature cycling

As shown in figure 6.8, the samples stored at dry ice temperature recrystallize much faster than the samples stored at room temperature. In this case, they are about three times faster. This result has been observed with all geometries, both baths and both barrier materials. The samples stored at room temperature recrystallize always slower than the samples stored at dry ice temperature.

The reason for this behaviour is presumably some kind of inelastic deformation of the samples at low temperatures [27]. Since the samples consist of several layers with different thermal expansion coefficients, there is a change in stress when the copper is cooled. The stress could force the copper to be deformed plastically and to form dislocations, which could serve as nuclei for the recrystallization process. Since the wafers are patterned, there may also be non-uniformities in microstrains and the density of dislocations and defects that are further affected by cycling to dry ice temperature [26].

There is one uncertainty involved in this measurement. The problem is that the samples stored at room temperature have not only been exposed to room temperature, but to a variety of temperatures during the transport. Immediately after plating, these samples were shipped by an unheated cargo plane during winter, therefore the thermal history of the samples is unknown. We can only assume that the minimum temperature they were exposed to is much higher than the temperature of dry ice. These samples have been put on dry ice immediately after plating to stop the recrystallization process.

As one can see in figure 6.8, the samples shipped at room temperature have already started recrystallizing about 20 hours before I could start observing them in the FIB.

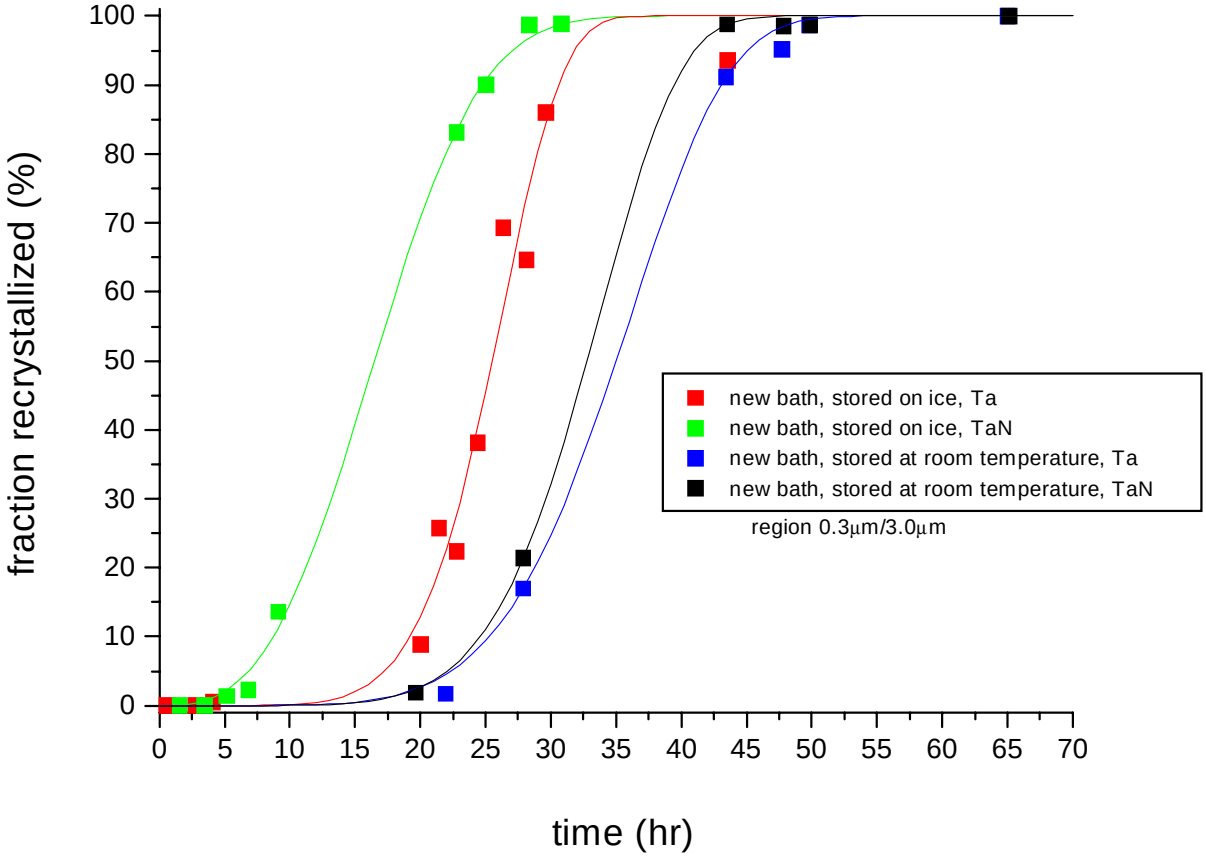

Figure 6.8: Recrystallization of samples stored at room temperature and at dry ice, trench depth is 0.5µm.

During this time, the 0.8µm wide trenches plated with the old bath had already recrystallized to more than 90%. Therefore there are only a few data points for the faster regions. Since it was possible to monitor the recrystallization of the samples stored on dry ice from the beginning, much more images of the recrystallization process have been taken. The data of the dry ice samples is therefore much more significant. Because of this, the following sections refer only to samples stored on dry ice.

Nevertheless all the trends noted for the dry ice samples are also valid for the samples stored at room temperature. The influence of the parameters geometry, barrier material and age of the bath seems to be exactly the same, regardless of the storage temperature of the samples.

6.2.2 Influence of the age of bath

The chemistry of the plating bath is one of the most important parameter in the process of electroplating. It influences the filling of the trenches, the incorporation of impurities from organic additives, the grain size and the recrystallization [19],[37].

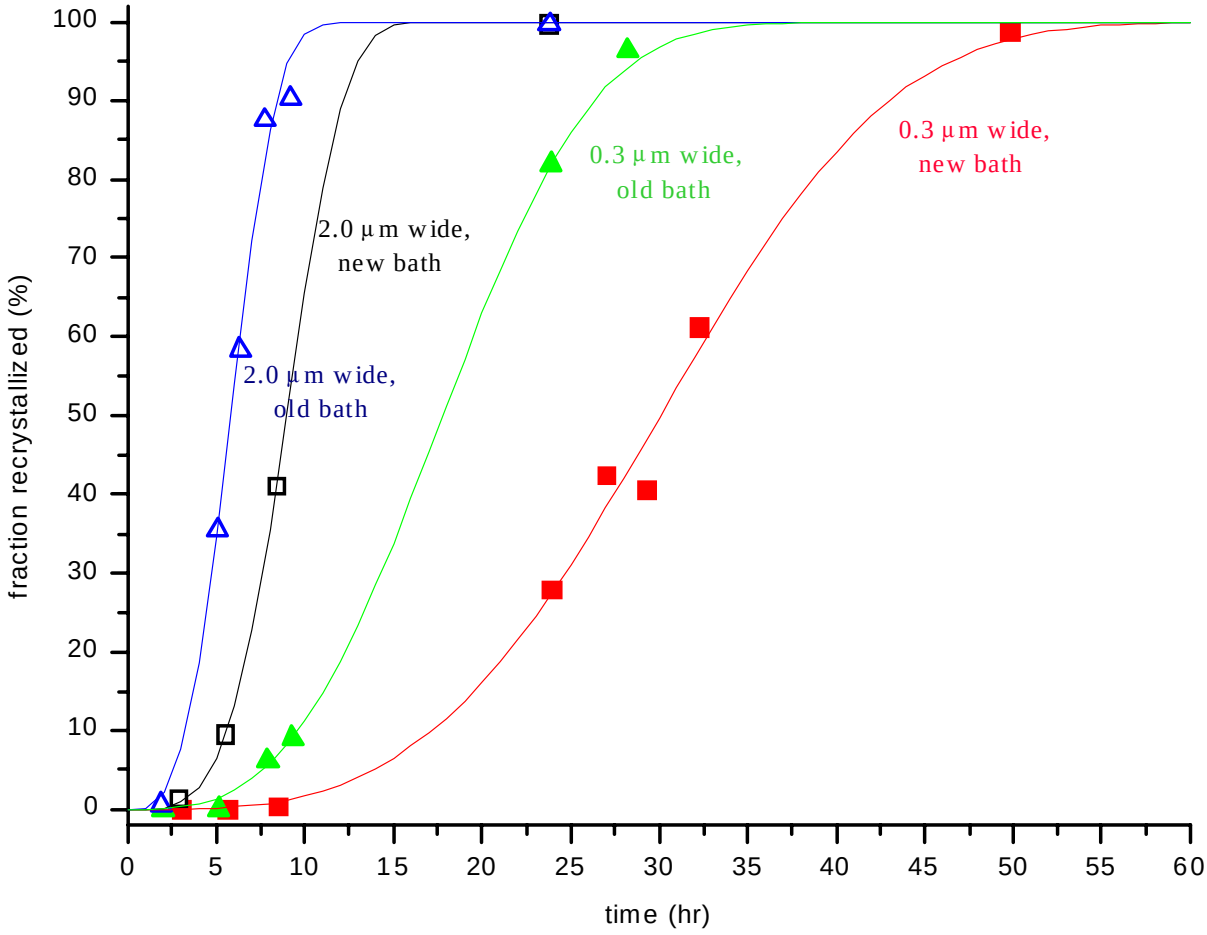

Figure 6.9: Recrystallization of samples plated in the old vs. new bath, barrier is Ta, depth of the trenches are 1µm.

The plating solution consists of copper sulfate, sulfuric acid with HCl and organic additives that help to achieve void free filling of narrow trenches with high aspect ratios. If a wafer is plated in a solution without additives, the copper grains are larger, the surface is rougher and no recrystallization is observed at room temperature. This experiment was intended to investigate the influence of the bath age, and therefore the level of impurities in the bath, on the recrystallization kinetics.

Wafers were electroplated using two different plating solutions. One plating bath was freshly prepared, the second was the same bath after 3000 wafers had been processed with additives replenished at the recommended rate. This replenishment helps maintain equilibrium of additives in the bath.

It is hard to quantify the difference between the two baths, since the company providing the plating solution does not give any detailed analytical information. The term 'new' or 'old' plating bath is therefore only qualitative. To see the difference the age of the bath has on the samples, secondary ion mass spectroscopy (SIMS) was done both

on the samples from the old and the new plating bath. Surprisingly, the results show no big difference of incorporated material in the copper.

However, even though the SIMS analysis are similar, the samples plated in the old bath recrystallize much faster than the samples plated in the new bath (figure 6.9). This result has been observed with all geometries, both temperatures and both barrier materials.

A reason for this behaviour could be that in the old bath somehow fewer or different types of impurities were deposited with the copper despite the old bath having a higher concentration of additive byproducts. Normally, one would expect that if the sample contains more incorporated impurities, these should pin the grain boundaries and slow down the recrystallization process.

Perhaps the difference in the recrystallization rate is not related to the impurities, but to differences in the additive influence of the plating process. The additives have such a strong influence on the way the copper is deposited that the two baths may have different effects on the copper during deposition.

6.2.3 Influence of the sample geometry

The geometry of the trenches has an enormous effect on the recrystallization.

As shown in figure 6.10 there are two regions with almost the same recrystallization speed competing for the fastest recrystallization, depending on the depth of the trenches. In the case of a 0.5µm deep trench, the region 0.8µm/3.0µm takes less time to recrystallize than the region 2.0µm/2.0µm. In the case of the 1.0µm deep trenches, it is the other way around. The 5.0µm wide trenches need some more time to recrystallize and the region 0.3µm/3.0µm is always the slowest followed by the region 0.5µm/3.0µm.

The reason for the observed geometric effect is proposed to be related to the location where recrystallization is initiated. For the 2µm and 5µm trenches, recrystallization appears to start at the upper corner of the trenches, then spreads in the trenches where the copper is thicker more rapidly than between the trenches. Due to the limited number of trench widths available in this experiment, it is possible that there is a trench geometry with a trench width somewhere between 0.8µm and 2.0µm, which recrystallizes faster than the samples analyzed here.

As the trench width decreases, it is no longer possible to correlate the initial large grains with underlying topography. At the smaller trench widths, the non-uniformities in the defects, dislocations and microstrains that serve as the nucleation sites for recrystallization may average out over several trenches. At wider widths it may appear more uniform. Therefore if a non-uniform distribution accelerates recrystallization, the seemingly more uniform distribution gives a slower rate [27],[26].

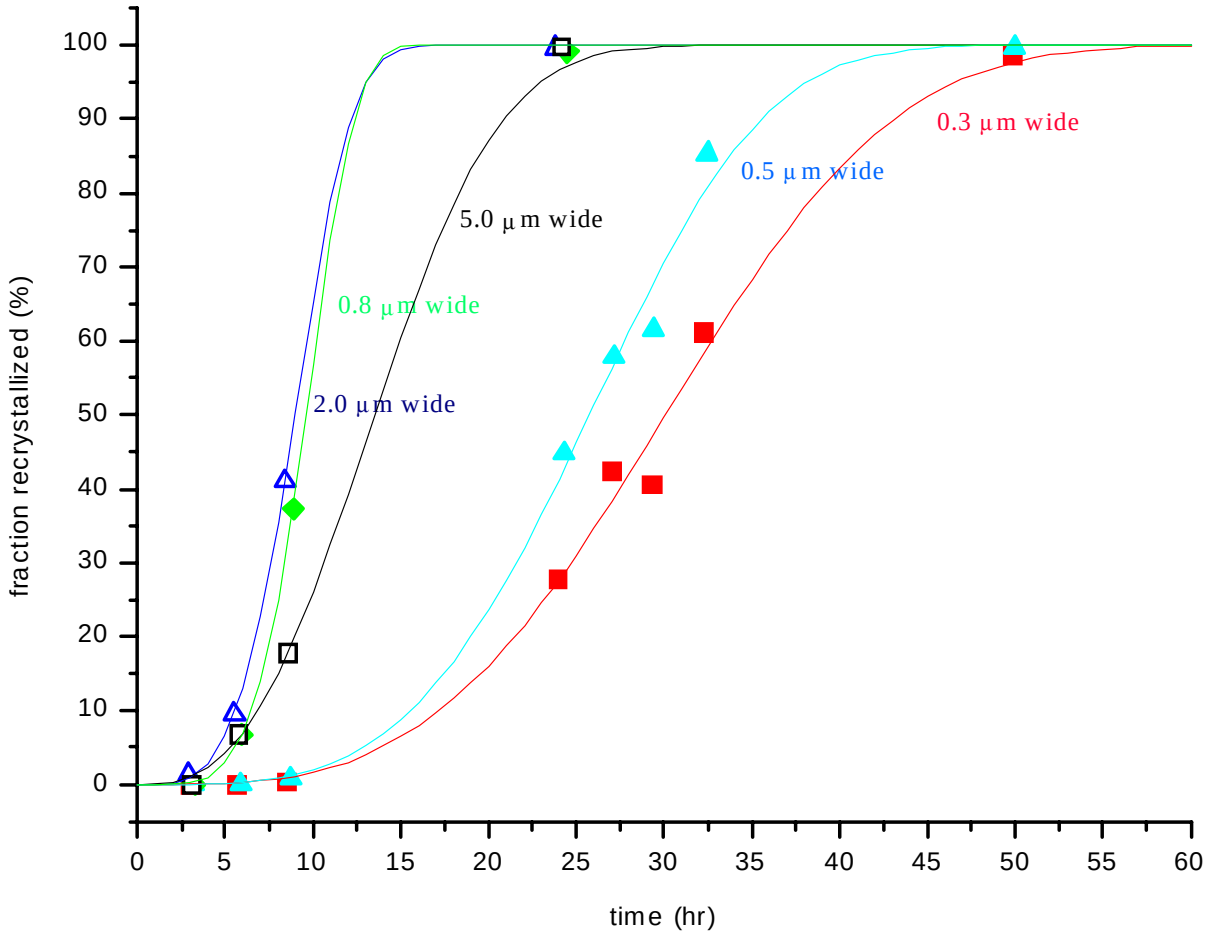

Figure 6.10: Recrystallization of samples with different geometries, the samples were plated in the new bath and are 1µm deep.

6.2.4 Influence of the barrier material

The barrier material also has an influence on the recrystallization kinetics. As shown in figure 6.11, the samples with TaN as barrier material always recrystallize faster than those with Ta. This result is valid for all geometries, both temperatures and both baths.

A closer lattice match between the β-Ta and the copper than between the multi-phase TaN and the copper could be the reason for these results. The copper may not be hindered by the TaN to reorient itself, whilst the interaction between the Ta and the copper might be stronger. The lattice misfit between Ta (111) and Cu (111) is 21.4%. It is not possible to determine the misfit between the TaN and the Cu, since the TaN used in these samples is present in several phases and its X-ray signature is very weak.

The bond strength at the interface between the barrier and the copper could have a strong influence on the recrystallization speed as well as the different energy states of the bond.

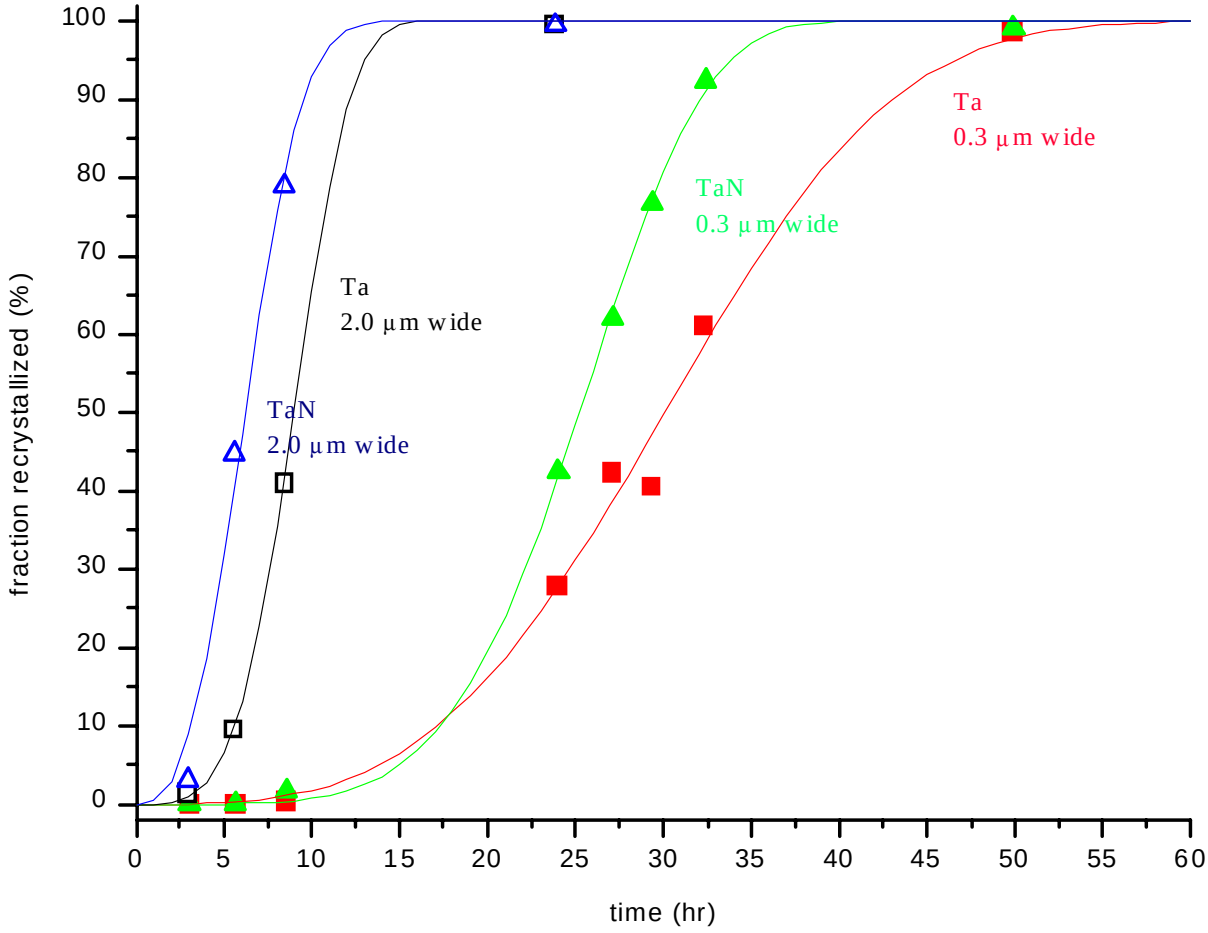

Figure 6.11: Recrystallization of samples with different barrier materials, plated in the new bath. The depth of the trenches is 1µm.

6.2.5 Summary of the recrystallization experiment

The fitting parameter t_r of the Avrami-Johnson-Mehl equation (see formula 5.1) can be taken as a numerical value for the speed of the recrystallization since it represents the time at which about 63% of the material is recrystallized. To summarize the effect of the three parameters bath age, barrier material and geometry, t_r is plotted in figure 6.12 for samples with a trench depth of 0.5µm and 1.0µm which have been kept on dry ice prior to measurement.

In this format it is easy to see the differences between the old and new bath, between Ta and TaN as barrier material and the influence of the trench geometry. The results are very consistent, the shape of the graphs is about the same for all parameters. This is surprising considering the possible errors in the measurements.

The overall error of the measurement is hard to quantify. There are two major error possibilities here, experimental errors and human errors caused by the judgment of the person analyzing the pictures. To quantify the human errors pictures were analyzed

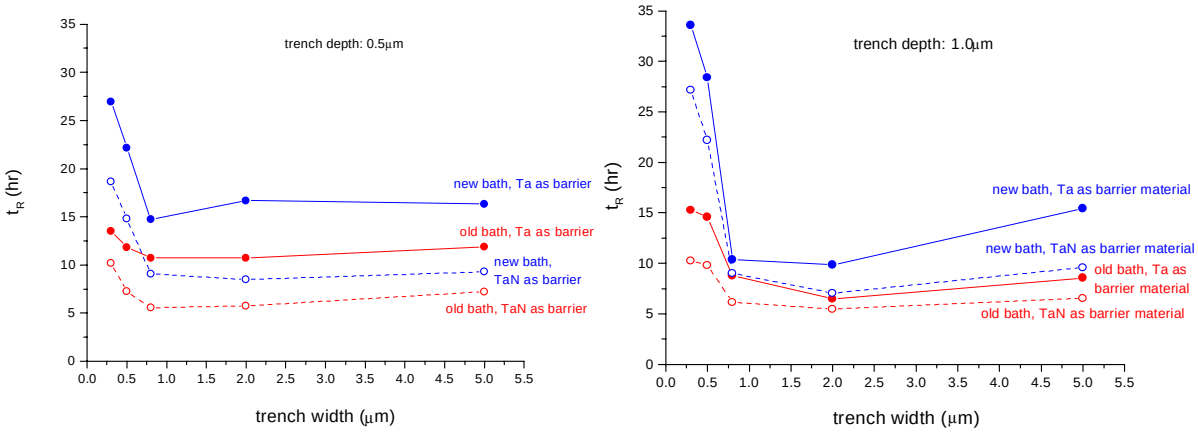

Figure 6.12: Comparison of fitting parameter t_r for the parameters bath age, barrier and geometry. The figure on the left shows samples with a trench depth of 0.5µm, on the right, the trenches are 1µm deep. All samples have been stored on dry ice.

by different people. The results of the picture analysis varied by an absolute value of up to 10% per image depending on the picture analyzed.

The experimental errors are hard to quantify. The area analyzed is 30µm by 30µm large and therefore very small compared to the size of the 5mm by 5mm overall area and should not have any statistical relevance. But compared to the small grains of size 0.1µm, the area is again quite big, there is space for about 90000 small grains. When we assume that the recrystallization is homogeneous over the sample area, the statistical error should be small. The size of the trenches is also very important for the error. In the areas with small trenches, e.g. region 0.3µm/3.0µm, one picture contains 9 trenches, in the region 5.0µm/5.0µm there are only 3 trenches. Since the important part of this experiment is the influence of the trenches, the data taken on the areas with smaller trenches should be statistically more significant than the data taken on the areas with wider trenches.

In my opinion, the biggest uncertainty here is the fact that the copper shows abnormal grain growth and therefore the grains are gathering in clusters. Sometimes large parts of one picture showed strong recrystallization, whilst another part of the same picture was still small grained with no visible grain growth at all (compare figure 5.3). Therefore I would say that the absolute experimental error is at least 20% with variation over time. It would be possible to reduce the error easily by taking more FIB pictures and analyzing them.

Conclusions

The properties of copper in damascene trenches have been analyzed using a focused ion beam microscope and two different X-ray systems. The samples used for these experiments resemble interconnects used in computer chips. They contain trenches, which are etched in an insulating silicon oxide layer. These trenches are covered with a barrier material to hinder the copper from diffusing into the insulating oxide. After deposition of the barrier layer, a thin copper film is sputtered onto the samples to allow the electroplating of a thick copper film. Some samples have been prepared to investigate the sputtered copper film. No additional copper is electroplated onto these samples and the sputtered film is thicker.

The crystallographic texture of both sputtered and electroplated copper has been studied by X-ray texture analysis. The texture is measured for the (111), (200) and (220) planes up to 80° in χ and complete pole figures are calculated by a computer program.

Electroplated copper shows a unique behaviour, i.e. abnormal grain growth or recrystallization at room temperature. The recrystallization process is monitored in a focused ion beam by imaging the samples periodically.

The X-ray texture analysis of the sputtered samples shows that the central peak of the texture is split at an angle of $\pm 10°$ for small feature sizes. Samples with large trench widths do not show this behaviour. With increasing feature sizes, the split of the peak decreases. The difference between samples with Ta and TaN as barrier material is small, but visible.

Some electroplated samples show a distinct sidewall texture. This texture is a fiber texture perpendicular to the walls of the trenches. It can be explained by the growth process during electroplating. The copper grows as well on the sidewalls as it does on the bottom of the trenches during deposition. The behaviour of this texture component upon annealing has been studied in detail. The result is that the grain growth has no preferred texture, all grains grow the same way, regardless of their orientation.

The kinetics of the room temperature recrystallization has been studied for electroplated samples with respect to several parameters.

The storage temperature has a significant effect on the recrystallization process. Samples that have been stored at room temperature, recrystallize much slower than samples stored at the temperature of dry ice. This is presumably caused by plastic deformation in the samples due to thermal stresses caused by the temperature difference between deposition and storage. The plastic deformation causes nucleation sites, where grain growth can start.

The influence of the age of the plating solution on the recrystallization speed has been investigated, too. The experiment shows that the samples plated in the old bath recrystallize faster than the other samples. This result is a surprise, since one would expect that during the plating with the older bath, more dirt is incorporated into the copper and this dirt should pin the grain boundaries and slow down recrystallization. However, secondary mass ion spectroscopy shows no significant difference in the impurity concentration in the samples plated in the different solutions. This leads to the conclusion that the plating solution influences the properties of the copper by changing the way it is deposited.

Despite the differences in recrystallization kinetics, the texture of the samples plated in the different solutions show no structural difference. The central peak of the sample plated in the new bath is much higher than the central peak of the sample deposited in the old solution, but the structure of the texture seems to be similar.

The sample geometry plays a crucial role in the recrystallization process. Depending on the width of the trenches, the speed of the grain growth varies. The fastest recrystallization occurs presumably at a trench width somewhere between 0.8µm and 2.0µm.

The barrier material determines the recrystallization speed, too. Samples with Ta as the barrier material recrystallize significantly slower than samples using TaN as barrier material. The interaction between the copper and Ta is presumably stronger than between the TaN and the copper. This might be related to the fact that TaN is present in several phases while Ta is crystalline.

The research on copper yet offers still a lot of open questions, which are worth investigation. It is for example not clear, why electroplated copper recrystallizes at room temperature, while sputtered copper of the same grain size needs to be annealed to show grain growth. Another interesting topic is how the plating solution influences the properties of the copper and which properties are related to the recrystallization.

Appendix A

Proof of equation 2.1

This chapter contains a proof of the basic equation 2.1:

$$\frac{x}{s} = \frac{2f}{R}.$$

The proof is based on the geometrical properties of the beam path in the setup as illustrated in figure A.1. The laser beam is shown for two different scanner positions. It is important to notice that each one of the two beams drawn in the figure represents the laser beam at a different instant in time, in reality they are never both present at once.

The two beams are focused by the curved sample into the focal point G. At a distance d from the sample, the lens is positioned. The distance between the two laser spots on the lens is s'. The two beams are refracted and focused into B at a distance b. The distance between the lens and the detector is the focal length of the lens f, the distance between the virtual object positioned at the point G and the lens is g.
The two relations needed for the proof are given by basic geometrical optics (e.g. [40]):

$$\frac{1}{f} = \frac{1}{g} + \frac{1}{b} \tag{A.1}$$

and

$$f_R = \frac{R}{2}. \tag{A.2}$$

Starting with

$$\begin{aligned} \frac{x}{s'} &= \frac{f-b}{b} = \frac{f}{b} - 1 \\ &\overset{\text{A.1}}{=} f \cdot \left(\frac{1}{f} - \frac{1}{g}\right) - 1 \\ &= \frac{f}{g} = \frac{f}{f_R - d} \end{aligned}$$

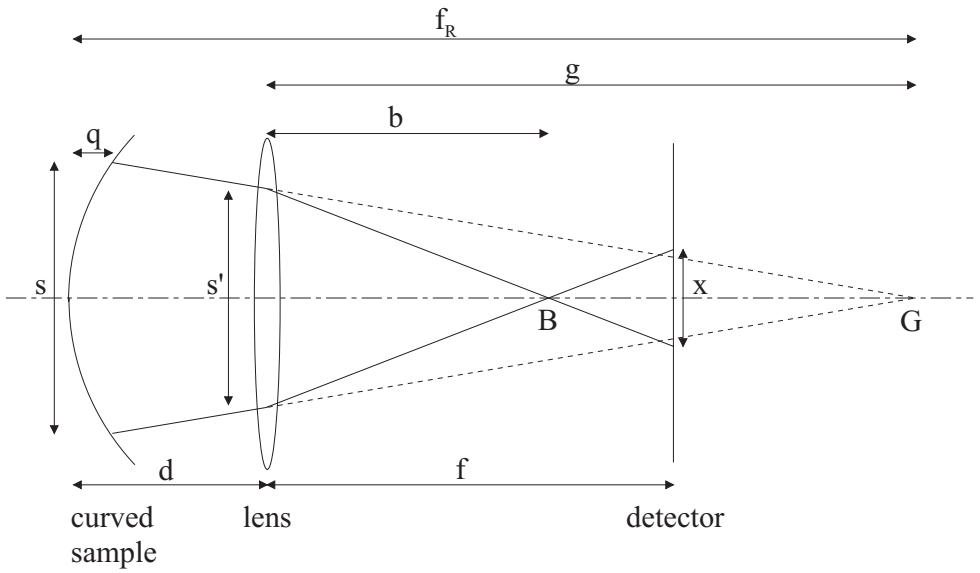

Figure A.1: The beam scans over the sample (s), the reflected beam is directed towards the focal point of the sample G at a distance f_R, but redirected by the lens towards B. It scans over the detector (x). The distance between the lens and the detector is the focal length f of the lens, the distance between the lens and the sample is d.

Substitute s' with s:

$$\frac{s'}{s} = \frac{g}{f_R - q} = \frac{f_R - d}{f_R - q}.$$

Combining the two equations gives

$$\begin{aligned} \frac{x}{s} &= \frac{x}{s'} \cdot \frac{f_R - d}{f_R - q} = \frac{f}{f_R - d} \cdot \frac{f_R - d}{f_R - q} \\ &= \frac{f}{f_R} \cdot \frac{1}{1 - \frac{q}{F_R}} \qquad (A.3) \\ &= \frac{f}{f_R}, \qquad q \ll F_R \\ &\overset{A.2}{=} \frac{2f}{R}, \qquad 2q \ll R \qquad (A.4) \end{aligned}$$

This proves that equation 2.1 is in fact valid with the restriction $2q \ll R$.

q has to be substituted with a parameter, which can be measured. The geometrical properties of the curved sample are shown in figure A.2:

$$\begin{aligned} R^2 &= \frac{s^2}{4} + R'^2 \\ q &= R - R' = R - \sqrt{R^2 - \frac{s^2}{4}} \end{aligned}$$

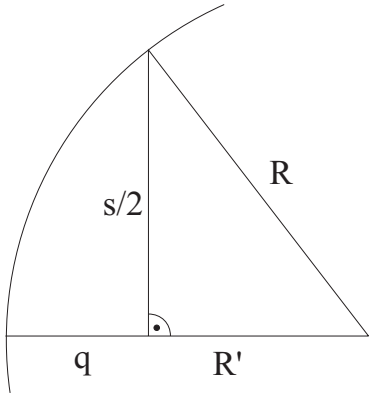

Figure A.2: Illustration of the geometrical properties of the sample

$$\Leftrightarrow 2 \cdot \frac{q}{R} = 2 - \sqrt{4 - \frac{s^2}{R^2}}$$

This gives

$$2q \ll R \Leftrightarrow s \ll R$$

To find out how low the ratio $\frac{s}{R}$ has to be for a measurement, the deviation factor given in equation A.3 is used:

$$\frac{1}{1 - \frac{2q}{R}} = \frac{1}{\sqrt{4 - \frac{s^2}{R^2}} - 1}$$

This is the ratio between the real curvature of a sample and its calculated curvature using equation 2.1. This deviation factor should be limited by a given value x, which can be e.g. $x = 1.01$ for a deviation of 1%.

$$\begin{aligned} \frac{1}{\sqrt{4 - \frac{s^2}{R^2}} - 1} &\leq x \\ \Leftrightarrow \sqrt{4 - \frac{s^2}{R^2}} - 1 &\geq \frac{1}{x} \\ \Leftrightarrow \frac{s^2}{R^2} &\leq 4 - \left(\frac{1}{x} + 1\right)^2 \\ \Leftrightarrow \frac{s}{R} &\leq \sqrt{4 - \left(\frac{1}{x} + 1\right)^2} \end{aligned}$$

Choosing a deviation of 1%, $x = 1.01$:

$$\frac{s}{R} \leq 0.199$$

The maximum s used is $s = 3$cm, this gives a minimum radius of

$$R \geq 15.09\text{cm}$$

for $\leq 1\%$ deviation between the real curvature of a sample and its calculated value.

Bibliography

[1] ARETZ, P. Aufbau eines Spannungsmeßplatzes und dessen Charakterisierung. Diploma thesis, RWTH Aachen, August 1999.

[2] BLAKELY, J. M. *Journal of applied Physics 35* (1964), 1756.

[3] BRÜCKNER, W., AND GRIESSMANN, H. Apparatus for the laser-optical measurement of stress in thin films: Results on CuNi. *Review of scientific instruments 69*, 10 (October 1998), 3662–3665.

[4] *CRC Handbook of Chemistry and Physics*, 78th ed., vol. 4 A. CRC Press, 1997.

[5] CULLITY, B. D. *Elements of X-ray diffraction*, 2nd ed. Addison-Wesley, 1978.

[6] DURELLI, A. J., PHILLIPS, E. A., AND TSAO, C. H. *Introduction to the Theoretical and Experimental Analysis of Stress and Strain*. McGraw-Hill Book Company, Inc., 1958.

[7] EDELSTEIN, D. Copper ULSI interconnect technology. *Advanced Interconnects and Contact Materials and Processes for Future Integrated Circuits Symposium Material Research Society* (April 1998), 39–.

[8] EMERY, R., SIMONS, C., MAZIN, B., AND POVIRK, G. L. High temperature tensile behaviour of free-standing gold films. *Thin-Films-Stresses and Mechanical Properties VII. Symposium Material Resarch Society* (December 1997), 57–62.

[9] EMERY, R. D., LENSHEK, D. X., BEHIN, B., GHERASIMOVA, M., AND POVIRK, G. L. Tensile behaviour of free-standing gold films. *Polycrystalline Thin Films – Structure, Texture, Properties and Applications III. Symposium Material Research Society* (April 1997), 361–6.

[10] FLETCHER, A. J. *Thermal Stress and Strain Generation in Heat Treatment*. Elsevier Applied Science, 1989.

[11] FLIESSBACH, T. *Statistische Physik*. BI Wissenschaftsverlag, 1993.

[12] FLINN, P. A. Measurement and Interpretation of stress in Alu-based metallization as a function of thermal history. *IEEE Transactions on electron devices 34* (1987), 689–698.

[13] FRANZ, P. Untersuchungen zu den struktuellen Eigenschaften des Phasenwechselmediums $Ge_2Sb_2Te_2$. Diploma thesis, RWTH Aachen, November 1999.

[14] GARDNER, D. S., AND FLINN, P. A. Mechanical Stress as a Function of Temperature in Aluminum Films. *IEEE Transactions on electron devices 35*, 12 (December 1988), 2160–2169.

[15] GELLER, W. *Großes Handbuch der Mathematik*. Buch und Zeit Verlagsgesellschaft m.b.h. Köln, 1970.

[16] GEORG, A. *Zum optischen Schalten von Wolframoxidschichten mittels reduzierender und oxidierender Gase*. PhD thesis, Universität Freiburg, März 1999.

[17] GRANQVIST, C. G. *Handbook of inorganic electrochromic materials*. Elsevier, 1995.

[18] GROSS, M. E., LINGK, C., AND SIEGRIST, T. Microstructure and Texture of Electroplated Copper in damascene Structures. *Materials Research Society Proceedings Advanced Interconnects and Contact Materials and Processes for Future Integrated Circuits* (April 1998), 293–8.

[19] GROSS, M. E., TAKAHASHI, K., RITZDORF, T., AND GIBBONS, K. The Role of Additives in Electroplating of Void-Free Cu in Sub-micron Damascene Features. *Advanced Metallization Conference* (October 1998).

[20] HENKE, M. Präparation und Charakterisierung von Phasenwechselschichten zur optischen Datenspeicherung. Diploma thesis, RWTH Aachen, October 1998.

[21] HODGE, T. C., BIDSTRUP-ALLEN, S. A., AND KOHL, P. A. Stresses in Thin Film Metallization. *IEEE Transactions on components, packaging and manufactoring technology 20*, 2 (June 1997), 241–250.

[22] KITTEL, C. *Introduction to Solid State Physics*, 5th ed. John Wiley & Sons, Inc., 1976.

[23] LANDOLT-BÖRNSTEIN. *Zahlenwerte und Funktionen aus Physik, Chemie, Astronomie, Geophysik und Technik; Wärmetechnische Messverfahren, thermodynamische Eigenschaften homogener Stoffe*, 6th ed., vol. 4 A. Springer Verlag, 1967.

[24] LIBERA, M., AND CHEN, M. Multilayered Thin-Film Materials for Phase-Change Erasable Storage. *MRS Bulletin* (April 1990), 40–45.

[25] LINGK, C., AND GROSS, M. E. Pole Figure Analysis of Electroplated Cu in Damascene Trenches. *Advanced Metallization Conference* (October 1998).

[26] LINGK, C., AND GROSS, M. E. Recrystallization kinetics of electroplated Cu in damascene trenches at room temperature. *Journal of Applied Physics 84*, 10 (November 1998), 5547–53.

[27] LINGK, C., AND GROSS, M. E. Room Temperature Recrstallization of Electroplated Cu in Damascene Structures: Kinetics and Mechanics. *Advanced Metallization Conference* (October 1998).

[28] LINGK, C., GROSS, M. E., AND BROWN, W. L. X-ray diffraction pole figure evidence for (111) sidewall texture of electroplated Cu in submicron damascene trenches. *Applied Physics Letters 74*, 5 (February 1999), 682–4.

[29] Werkstoffkunde dünner Schichten, Skript zur DGM-Fortbildungsveranstaltung. Max-Plank-Institut für Metallforschung, Seestraße 92, 70174 Stuttgart, Germany, March 1998.

[30] MAYER, J. W., AND LAU, S. S. *Electronic Materials Science: For Integrated Circuits in Si and GaAs*. Macmillan Publishing Company, 1990.

[31] OHRING, M. *The materials sience of thin films*. Academic Press, Inc., 1992.

[32] *One, two-dimensional PSDs (position sensitive detectors)*. Hamamatsu Photonics K. K., Solid State Division, 1997.

[33] PEDERSEN, T. L. Personal conversation, January 2000.

[34] PROOST, J., WITVROUW, A., COSEMANS, P., ROUSSEL, P., AND MAEX, K. Stress relaxation in Al(Cu) thin films. *Micorelectronic engineering 33* (1997), 137–147.

[35] SCHULZE, G. E. R. *Metallphysik*, 2nd ed. Springer Verlag, 1974.

[36] STONEY, G. G. *Proc. Roy. Soc. London A82* (1909), 172.

[37] TAKAHASHI, K. M., AND GROSS, M. E. Analysis of Transport Phenomena in Electroplated Copper Filling of Submicron Vias and Trenches. *Advanced Metallization Conference* (October 1998).

[38] TAYLOR, C., BARLETT, D., CHASON, E., AND FLORO, J. A Laser-Based Thin-Film Growth Monitor. *The Industrial Physicist* (March 1998), 25–27.

[39] THISSEN, G. Herstellung und Charakterisierung gasochromer Schichten auf der Basis von Wolframoxid. Diploma thesis, RWTH Aachen, Juli 1999.

[40] VOGEL, H. *Gerthsen Physik*. Springer-Verlag, 1995.

Acknowledgements

- First, I would like to thank Prof. Dr. Matthias Wuttig for giving me the opportunity to experience the experimental environment in a different country and for the discussions and suggestions during the work in his institute.
- Priv. Doz. Dr. Thomas Michely is gratefully acknowledged for correcting this thesis and for many practical hints concerning the vacuum setup.
- I want to thank Dr. Walter L. Brown for giving me the opportunity to experience the research environment at the Bell Laboratories and for his strong encouragement, constructive discussions and his help during that time.
- I sincerely thank Tom Leervad Pedersen for guiding my work at the RWTH-Aachen and for the fruitful and pleasant discussions.
- Mihal E. Gross is gratefully acknowledged for patiently teaching me much about scientific work and for guiding my experimental work at the Bell Labs.
- I want to thank Ken Evans-Lutterodt for the fruitful and pleasant discussions at the Labs and during the nice trips to Madison and Christoph Lingk for introducing me to the world of FIB and the X-ray diffraction as well as the american way of life.
- The people of the mechanical workshop are gratefully acknowledged. Without their knowledge and skills this work would not have been possible. Especially Mr. Siedling and Heinz Vonhoegen have helped us a lot when designing and improving the system.
- I want to thank Mr. Selvaraj Venkataraj and Ralph Spolenak who helped me a lot by reading this report.
- I sincerely thank Hans-Jörg and Christian for the support with the switchable windows and Ines and Oliver for providing many sputtered samples.
- Last but not least, my parents are gratefully acknowledged for their great support during my graduation.